NASA-CR-194627

Meso-Beta Scale Numerical Simulation Studies of Terrain-Induced Jet Streak Mass/Momentum Perturbations

NAG 5-1790
IN-47-CR
191243
121 P

FY93 November Semi-Annual Report

submitted to the
Mesoscale Processes Research Program
Atmospheric Dynamics and Radiation Branch
Earth Science and Application Division
Office of Space Science and Applications
NASA Headquarters
Washington, D. C. 20546
Attention: Dr. Ramish Kakar, Program Manager

by

Yuh-Lang Lin and Michael L. Kaplan
Department of Marine, Earth, and Atmospheric Sciences
North Carolina State University
Raleigh, North Carolina 27695-8208
(919) 515-7977

November 1993

(NASA-CR-194627) MESO-BETA SCALE NUMERICAL SIMULATION STUDIES OF TERRAIN-INDUCED JET STREAK MASS/MOMENTUM PERTURBATIONS Semiannual Report (North Carolina State Univ.) 121 p

N94-20138

Unclas

G3/47 0191243

Table of Contents

Part I. 3-D Numerical Modeling of Meso-Beta Scale Terrain-Induced Jet Streak Mass/Momentum Adjustments

a) Design of the Control-B Nested-Grid Simulation 1

b) Simulation of the Background Jet Streak Geostrophic Adjustment Process and Its Role in Organizing the Orogenic Forcing 2

1) Primary Geostrophic Adjustment Period 3
2) Secondary Frontogenetical Period 5
3) Secondary Geostrophic Adjustment Period 7

c) Simulation of Orogenically-Forced Adjustment Processes and the Development of CCOPE Gravity Wave Episodes I and II 9

1) Genesis of Gravity Wave Episode I 10
2) Genesis of Gravity Wave Episode II 12
3) Environment for the Generation of the MCS 14

d) Summary and Conclusions 16

e) Current and FY94 Planned Research Simulation Experiments 20

Part II. Linear Theory and Theoretical Modeling

a) Summary of FY93 Theoretical Work 21

b) Proposed FY94 Research 27

1) Future Work on Homogeneous Atmospheres 27
2) Future Work on Continuously Stratified Atmospheres 28

References 32

List of Figures 36

Part I. 3-D Numerical Modeling of Meso-Beta Scale Terrain-Induced Jet Streak Mass/Momentum Adjustments

a) Design of the Control-B Nested-Grid Simulation

The Control-B simulation experiment was designed to improve on the Control-A experiment performed with the GMASS model during FY92. This experiment addressed several inadequacies with the first smooth terrain numerical simulation by including: 1) increased nested-grid resolution to better define the simulated gravity waves, 2) increased horizontal diffusion to remove outflow boundary condition noise, and 3) the use of reanalyzed rawinsonde data and surface observations in the initial state to increase the definition of the observed jet streak as well as other low-level features. The Control-B simulation involved the use of smooth terrain and two matrices of 223 x 146 x 30 grid points with 16 km and 8 km horizontal resolution, respectively, for the coarse and nested-grid simulations as are depicted in Figure 1. The actual horizontal resolution was even finer at the latitude of interest over the grids depicted in Figure 1 due to standard map scale distortion accompanying the polar stereographic projection. This region of nested-grid simulation includes the CCOPE mesonetwork in Montana. The GMASS model, which is a modified version of the MASS model (Kaplan *et al.* 1982) has been described in Whitaker *et al.* (1988). This model was integrated over the coarse mesh matrix for a period of 30 hours of real time commencing at 0000 UTC 11 July 1981 and terminating at 0600 UTC 12 July 1981. The nested-grid simulation began at 0900 UTC 11 July 1981 and terminated at 0600 UTC 12 July 1981, thus covering a real-time period of 21 hours. These simulations were performed on the Cray Y-MP at the MCNC computing facility in Research Triangle Park, North Carolina who provided all of the computer time for these and subsequent experiments. The simulation experiments required more than 40 million words of in-core memory on the MCNC Cray Y-MP, thus utilizing all of the available memory.

The initial data were based on the analyzed 2.5 x 2.5 degree global analyses from NCAR with North American rawinsonde and hourly surface data reanalyzed into the initial state. Highly

smoothed NWS LFM terrain data were employed for the Control-B simulation as is depicted in Figure 1b. The smoothed terrain should be compared to the high resolution terrain to be employed in subsequent numerical simulations depicted in Figure 2. The Control-B simulation also included a complete surface energy budget within the Blackadar planetary boundary layer code with surface sensible heating and latent heat flux, but condensation processes within the atmosphere above the surface were not allowed, i. e., no convective or stratiform clouds or precipitation was simulated. The effect of soil moisture on the energy budget was neutralized by maintaining uniform sparse values in the initial conditions. The purpose of this simulation was to act as a significantly improved control run prior to the inclusion of meso-β scale terrain and condensation processes in the numerical model. The simulation experiments were designed to determine the extent to which background geostrophic adjustment processes, shearing instability, and/or smooth orogenic forcing organized the gravity wave phenomena and other mesoscale dynamical processes observed by Koch and Golus (1988), Koch *et al.* (1988), Koch and Dorian (1988), and Koch *et al.* (1993) over and in proximity to the CCOPE mesonetwork.

b) Simulation of the Background Jet Streak Geostrophic Adjustment Process and Its Role Organizing the Orogenic Forcing

In this section of the report we will emphasize the first 12 hours of the coarse mesh and first 3 hours of the nested-grid simulations which collectively span the period through 1200 UTC 11 July 1981. This period roughly corresponds to the period immediately preceeding the development of the gravity waves R1, R2, RU, and R3 during the first wave episode wherein the waves were eventually observed over CCOPE during the 1700 UTC through 2100 UTC period as described by Koch *et al.* (1988). Also, as noted in Koch *et al.* (1988), the actual organization of these waves occured near the intersection of the Idaho, Montana, and Wyoming borders during the 1100 UTC through 1600 UTC period. Wave episode II, including waves R4, R5, and R6 were also organized in this region during the 1800 UTC through 2300 UTC period and subsequently affected CCOPE between 0000 UTC and 0700 UTC. In order to better describe the complex

dynamical processes at work during the organizational period, which created a background mesoscale environment over Idaho, Montana, and Wyoming conducive for orogenically-forced gravity waves episodes I and II in this case study, we will partition this organizational period between 0000 UTC and 1200 UTC 11 July into three stages. These stages will be termed: 1) primary geostrophic adjustment period (~0300 UTC - 0600 UTC), 2) secondary frontogenetical period (~0600 UTC - 0900 UTC), and 3) the secondary geostrophic adjustment period (~0900 UTC - 1200 UTC). In order to focus on the organizational adjustments, the numerical model output, both coarse and nested-grid, will be displayed over the three-state region and southern Canada as depicted in Figure 3. Also depicted in Figure 3 are the locations of the two vertical cross sections which are employed in the analyses of numerical model simulation fields. These include a cross section orthogonal to the jet from Spokane, Washington (GEG) to Rapid City, South Dakota (RAP) and a cross section parallel to the jet from Boise, Idaho (BOI) to Dickinson, North Dakota (DIK). Both of these cross sections pass over parts of the observed gravity wave generation region and the CCOPE observational network.

1) Primary Geostrophic Adjustment Period

Depicted in Figure 4 are the simulated coarse mesh 300 mb and 500 mb height fields valid at 0100 UTC - 0300 UTC 11 July 1981. Evident are the strongest east-west and south-north gradients of height over northern Idaho, northwestern Montana, southern British Columbia, southern Alberta, and southwestern Saskatchewan. This region represents the core of the mid-upper tropospheric geostrophic wind velocity and total wind velocity maximum and will be referred to as the "*stream*" during the first geostrophic adjustment period. The largest magnitude height gradients at this time are directed toward the northwest which is nearly orthogonal to the stream over the "chimney" region of northern Idaho. These gradients diminish rapidly downstream and to the southeast of this region. Hence, air parcels entering this region, *which represents the approximate location of the inflection point in the height field* between the cutoff low pressure area over western Washington and the ridge of high pressure over eastern Montana, will

be accelerated across the stream towards the northwest. Thus, as the weak short wave trough propagates through the inflection point by 0300 UTC, air parcels will be accelerated to the left of the stream indicated by an increase in the local meridional (v) wind component during the 0200 UTC - 0400 UTC period most notably near the southern British Columbia, southern Alberta, extreme northwestern Montana, and northern Idaho border regions. In response to this northwestward acceleration, the inertial-advective terms in the equations of motion will produce an increase in the zonal (u) wind component directed towards the southeast in an effort to restore the flow into geostrophic balance, i. e., the u-component will increase markedly just southeast of the increasing v-component as can be seen in Figure 5 predominantly over southwestern Montana. This process is consistent with that described by Kaplan and Paine (1977), Zack and Kaplan (1987), Uccellini and Koch (1987), and Koch and Dorian (1988) wherein the variation in the Laplacian of height forces air parcels to increase their divergence significantly over short time periods resulting in the eventual modification of the rotational wind. While this first geostrophic adjustment process occurs several hours prior to the observed genesis of gravity waves over southwestern Montana, it sets into motion a sequence of mesoscale processes responsible for a second adjustment process which occurs in the correct region and time of the observed wave generation mechanism during episode I. *It should be noted, however, that while this first simulated geostrophic adjustment period preceeds the first gravity wave episode analyzed by Koch and Golus (1988) by several hours, microbarographs indicate ample evidence of gravity waves in nature at this time over Montana.* We will, however, only closely compare simulated gravity waves to observed waves during the active wave generation period between 1100 UTC and 2300 UTC.

2) Secondary Frontogenetical Period

The effect of the aforementioned adjustment process is to radically modify the fine scale structure of the jet stream between northeastern Oregon and southwestern Saskatchewan. What were two separate wind maxima at 0200 UTC are unifying into a northeast-southwest oriented

stream by 0700 UTC. To the southeast of this stream are strong east-west gradients of meridional (v) and south-north gradients of zonal (u) wind components, thus revealing significant shearing deformation as well as upper-level velocity convergence, particularly on the anticyclonic side of the jet from southwestern Montana to southeastern Montana as can be seen in Figure 6. These mid-upper tropospheric kinematic fields resulting from the first geostrophic adjustment process will play a key role in producing mid-upper tropospheric frontogenesis accompanying a mesoscale thermally-indirect circulation during the 0600 UTC through 0900 UTC time period.

Figures 7-8 depict the 0600 UTC - 0800 UTC coarse mesh heights and temperatures, 0500 UTC - 0700 UTC omega fields, and vertical cross sections of potential temperature, omega, and total wind velocity orthogonal to the stream during the 0600 UTC - 0800 UTC period. Horizontal cross sections are depicted at the 500 mb and 300 mb levels in Figure 7. The primary geostrophic adjustment process has, in effect, extended the right exit region of the jet across Montana. As a result of this process are the evolving mesoscale patterns of vertical velocity on either side of the stream wherein a narrow band of sinking motions near the western part of the Montana-Wyoming border is producing adiabatic warming at 300 mb on the order of ~2C/3hrs, while weaker warming is occurring at 500 mb. In proximity to this mid-upper tropospheric warming accompanying the transverse thermally-indirect circulation is an axis of weaker mesoscale cooling over northcentral Montana. This region of cooling, which is stronger at 500 mb during this time period, is the result of combined upward vertical motion and relatively larger magnitudes of westerly winds, thus resulting in ageostrophic shearing deformation and an increasing magnitude of cold advection as the stream is bisected from south to north across Montana. Hence, the indirect circulation producing net warming at 300 mb and 500 mb near the western part of the Montana-Wyoming border region, net cooling over northcentral Montana due to adiabatic expansion, and increased cold advection over central Montana, particularly at 500 mb, acts to produce, by 0800 UTC, a mid-upper tropospheric front to the southeast of the location of the primary baroclinic zone accompanying the stream at 0300 UTC. This represents a significant shift of over 250 km to the southeast in the location and increase in magnitude of the largest southeast-northwest oriented

temperature gradient throughout much of the mid-upper troposphere over Montana during the 0600 UTC through 0900 UTC time period. The strongest baroclinic zone has shifted from northwestern Montana and northern Idaho to southcentral Montana. Furthermore, there is every indication from Figures 7-8 that the geostrophic adjustment process has produced a component of indirect circulation *along* as well as across the stream, thus indicating the highly ageostrophic nature of this circulation.

This development of a secondary jet/baroclinic zone can be inferred from the infrared satellite imagery during this time period depicted in Figure 9. Quite apparent is the developing narrow plume of cloudiness from southcentral Idaho into southcentral Montana during the 0600 UTC - 0900 UTC time period. This plume lies to the southeast of the prexisting long narrow plume accompanying the original jet stream extending from southeastern Oregon to Saskatchewan. The plume is, in effect, a tracer for mid-upper tropospheric cooling processes which accompany the thermally-indirect circulations producing ascending motions on the cyclonic side of jet streaks.

These mid-upper tropospheric processes, which produce a positive thickness anomaly over southcentral Montana and a negative thickness anomaly over northcentral Montana, are further augmented and supplemented by simulated baroclinic processes within the planetary boundary layer occuring to the lee of the Front Range of the smoothed Rocky Mountains during the 0600 UTC - 0900 UTC time period. The complex synergy between upper-tropospheric adjustments and planetary boundary layer processes accompanying the high terrain is highlighted by the thermal and kinematic fields depicted in Figures 10-12 over northcentral Montana for the 0300 UTC - 0900 UTC period. During the 0300 UTC - 0600 UTC period the radiational cooling within the planetary boundary layer after simulated sunset along the lee slope of the Front Range acts to produce a narrow northwest-southeast oriented negative temperature anomaly at 850 mb and 700 mb. This anomaly is further amplified during the following 0600 UTC - 0900 UTC period as the northerly wind component at 850 mb increases in response to the amplifying southeastward-directed pressure gradient force within the planetary boundary layer as can be seen depicted in Figure 11. This increasing southeastward-directed low-level acceleration acts to produce low-level cold

frontogenesis over northcentral Montana by 0900 UTC. The pooling of colder air over northwestern Montana relative to southeastern Montana acts to amplify the negative height anomaly through the troposphere to the northwest of the aforementioned mid-upper tropospheric front relative to the positive height anomaly over the southeastern part of Montana. Hence, the lower tropospheric adjustments merely act to intensify the baroclinic zone and mass perturbation which has shifted well southeast, by 0900 UTC, of the baroclinic zone accompanying the original stream at 0300 UTC. This new detached baroclinic zone/mass perturbation represents a secondary geostrophic jet, thus inducing a secondary and more focused region of possible geostrophic adjustment after 0900 UTC which is located to the southeast of the primary adjustment region described in *1)* above.

3) Secondary Geostrophic Adjustment Period

Figures 12-15 depict the nested-grid simulated height, temperature, total wind, geostrophic wind, and ageostrophic wind fields throughout most of the troposphere and lower stratosphere valid at 0900 UTC - 1200 UTC 11 July. Most extraordinary in these fields is the very marked secondary baroclinic zone located over central Montana which has developed by 0900 UTC to the southeast of the primary baroclinic zone with the synoptic-scale jet streak over northwestern Montana and northern Idaho. This becomes most evident as one ascends to the 200 mb level. There are two definable geostrophic jet maxima at the upper levels with the entrance region of the secondary geostrophic jet lying very close to the observed gravity wave generation region just southeast of Salmon, Idaho (SMN) at 300 mb and 200 mb. This juxtapositioning of the secondary geostrophic jet's entrance region accompanying the secondary baroclinic zone relative to the primary jet stream's exit region produces a cross-stream ageostrophic wind component in excess of 50% of the total wind velocity value at 300 mb and 200 mb. These values are consistent with the criteria defined by Koch and Dorian (1988):

$$R_o = V_{ag}/V > 0.5 \qquad \text{(I.1)}$$

for an unbalanced flow regime wherein V_{ag} represents the cross-stream component of the ageostrophic wind and V represents the total wind velocity. The magnitude of imbalance increases between the 500 mb and 200 mb levels, thus producing a southeastward displacement of the jet directly over the observed gravity wave generation region between SMN and West Yellowstone, Wyoming (WEY). Consistent with this region of imbalance located between the exit region of the total wind velocity jet and entrance region of the geostrophic jet are values of the advective Rossby number (Uccellini *et al.* 1984):

$$R_o = | \mathbf{V} \cdot \nabla \mathbf{V} | / (f | \mathbf{V} |) \qquad \text{(I.2)}$$

which exceed 0.75 in magnitude over extreme southwestern Montana just downstream from the cross-stream ageostrophic wind maximum.

By 1200 UTC, the continued increase in magnitude of both the u-component and v-component velocities at 300 mb over the region encompassed by SMN, WEY, and Dillon, Montana (DLN) has resulted in a distinct secondary jet maximum more than 200 km to the south-southeast of the remnants of the primary maximum located over northcentral Idaho and northwestern Montana north of Missoula (MSO) and Great Falls (GTF). The secondary maximum is supported in large part by the increase in the u-component over extreme southwestern Montana which is well-detached from the primary lobe of the 300 mb jet located over northwestern Montana as can be seen depicted in Figure 14.

Thus, the adjustment of the wind field to the mass field accompanying the secondary baroclinic zone has produced a split in the jet with a secondary jet maximum lying directly above the observed gravity wave generation zone over extreme southwestern Montana by 1200 UTC. Underneath this secondary jet, nonuniform low-level pressure falls produce a northwest-southeast oriented subsynoptic low pressure trough resulting in an increased northward-directed pressure gradient force and the development of a strong low-level jet evident at 700 mb (note Fig. 16). Observed rawinsonde data at 1200 UTC (not shown) confirm the increase in the northward-directed pressure gradient over Wyoming, Idaho, and Montana relative to 0000 UTC 11 July 1981

thus supporting the simulated acceleration of the 700 mb winds toward the north during this period. This low-level jet represents a secondary lower branch counterpart to the upper-level jet exit region lying above it over the extreme southwestern part of Montana and southeastern part of Idaho, hence, it represents the low-level branch of the secondary transverse indirect circulation as the primary low-level jet to its northwest represents the low-level branch of the original jet's thermally-indirect circulation.

Figures 17a and b depict, schematically, the juxtapositioning of forcing functions during this first 12 hour period of the Control-B simulation and the circulations which result. This region over southwestern Montana, which is under the secondary jet stream, is also where observed gravity waves are generated, hence, the next issue to be determined is if there are indications that the simulation is generating these waves in the absence of high resolution terrain and condensation and, if so, are the waves the result of geostrophic adjustment, shearing instability, or both processes.

c) Simulation of Orogenically-Forced Adjustment Processes and the Development of CCOPE Gravity Wave Episodes I and II

The remaining 18 hours of the coarse mesh simulation and fine mesh simulation spanning the period from 1200 UTC on 11 July 1981 through 0600 UTC on 12 July 1981 can be logically partitioned into three phases: 1) the genesis period for gravity wave episode I from 1200 UTC through 1800 UTC, 2) the genesis period for gravity wave episode II from 1800 UTC through 0000 UTC, and 3) the genesis period for subsequent severe convection downstream from CCOPE from 0000 UTC through 0600 UTC.

1) Genesis of Gravity Wave Episode I

Figure 18 depicts the nested-grid 700 mb winds, omegas, temperatures, and relative humidities at 1400 UTC, i. e., shortly after the emergence of the low-level jet depicted in Figure 16a. As the low-level jet rises up from the Snake River Plain to the smoothed top of the Absaroka

Range over northwestern Wyoming, adiabatic expansion results in upslope cooling over the southwestern slopes and adiabatic compression results in downslope warming over the northeastern slopes (note Figure 17b for a schematic depiction of this process). This results in an along-stream solenoidal field caused by the bouyancy perturbations, i. e., isentropic undulations depicted in the vertical cross section B in Figure 19 over the wave genesis region. The development of this feature preceeds the development of the 700 mb saturation region near the border region of Idaho, Wyoming, and Montana which is consistent with the observed genesis of precipitation in consort with the development of wave R1 as depicted in Figure 20 and also as noted in Koch and Golus (1988). Hence, the low-level jet produces a mountain wave which results in an along-stream meso-β scale baroclinic zone directly over the observed wave genesis region by 1400 UTC. The upslope segment of the mountain wave produces a region of high mid-lower tropospheric relative humidity which propagates downstream in consort with but slightly upstream from the bouyancy perturbations accompanying the mountain wave.

The response to this forcing during the 1500 UTC through 1800 UTC period is to produce a series of along-stream wind velocity perturbations and isentropic undulations which propagate downstream towards the region covered by the CCOPE mesonetwork as can be seen depicted in Figure 21. The dominant isentropic, omega, and wind perturbation has a wavelength of ~160 km and is phase-shifted in the vertical indicative of a rearward/upstream tilted mode. This mode is approaching CCOPE between 1800 UTC and 1900 UTC which is one hour after the wave R1 is diagnosed within the network. This phase reversal and amplitude maximum within the 700 mb - 500 mb layer is consistent with the linear stability analyses performed by Koch *et al.* (1993). Above 500 mb, the signal of the wave drops off in amplitude precipitously.

The mean sea level hourly pressure fields valid at 1600 UTC and 1900 UTC depicted in Figure 22 indicate a pressure fall/rise maximum with an amplitude of ~.5 mb corresponding to the 700 mb - 500 mb isentropic/wind undulation which is propagating east- northeastward at ~17 ms^{-1} with a half-wavelength of ~ 80 km. This speed, wavelength, and its vertical structure indicate the liklihood of a gravity wave with characteristics similar to the primary waves during episode I as

observed by Koch and Golus (1988) over CCOPE. This mean sea level pressure perturbation is coupled to the dominant mid-lower tropospheric isentropic and wind perturbations between the wave generation region and CCOPE during the 1600 UTC - 1900 UTC time period.

It should be noted that the wave genesis process described above, in this subsection, is *not* totally different from the background geostrophic adjustment processes described earlier in this report. The mountain wave produces a warm and cold thickness perturbation which is weak but definable to the 200 mb level. Ahead of the warm perturbation is a weak meridional wind component acceleration which is, in turn, followed by a zonal wind component acceleration. These surges are quite evident at 500 mb during episode I as can be seen in Figures 23-24. They propagate towards CCOPE at an average velocity of ~ 100 km/hr and have a wavelength of ~ 150 km. At least two "surges" are definable during this first wave episode. The leading surge propagates out away from the orographically-induced bouyancy perturbation. This could indicate a weaker secondary gravity mode. These features damp in amplitude very markedly between the 500 mb and 300 mb levels. Since the wind field perturbations are moving faster than the pressure perturbation, the vertical velocity structure is not constant with respect to the isentropic undulation in time, thus causing variations in the quadrature relationship. Hence, the adjustment of the wind field to the adiabatically-forced orogenic bouyancy perturbation is larger in magnitude and has a shorter period than the background geostrophic adjustment, but follows a fundamentally similar sequence wherein cross-stream leftward-directed ageostrophy is followed by rightward-directed ageostrophic flow. This juxtapositioning of ageostrophy during the genesis of the gravity wave/mountain wave system on or about the 1400 UTC - 1600 UTC period can be seen depicted in Figures 23-25 wherein the terrain-induced thickness perturbation acts to supplement the prexisting height perturbation accompanying the secondary upper-level jet maximum. This maintains and reinforces the imbalanced region near the borders of Idaho, Montana, and Wyoming where gravity wave generation is observed to occur.

2) Genesis of Gravity Wave Episode II

During the 1800 UTC - 0000 UTC period, the intense surface heating simulated by the GMASS model over the smoothed elevated terrain from the Absaroka Range through the Bitteroot Mountains has produced a second diabatically-generated orogenic thermal perturbation which will act in a similar manner to the adiabatic thermal perturbation. This feature is analogous to orogenic circulations simulated by Tripoli and Cotton (1989a,b) and reflects the northwest-southeast orientation of the aforementioned mountains over southwestern Montana and northwestern Wyoming as can be seen in the 700 mb and 500 mb temperatures depicted in Figure 26. The thermal ridge accompanying this second feature has a wavelength of ~150 km which is somewhat longer than the first adiabatically-generated bouyancy perturbation. This feature is indicative of the development of a mountain-plains solenoidal (MPS) circulation wherein the thermally-direct circulation caused by the elevated heat source near the border region of Wyoming, Montana, and Idaho has induced an upslope low-level jet (MPS lower branch) over eastern Montana, western North, and western South Dakota as well as a return circulation aloft (upper branch MPS) directly above the wave generation region during this time period.

Figure 27 depicts vertical cross sections of simulated fields indicating the growth of the simulated dry adiabatic layer accompanying the developing MPS over the leeside sloping terrain just southwest of Billings, Montana (BIL) during the period from 0900 MDT to 2100 MDT. This deepening adiabatic layer approaches the ~550 mb level over the elevated terrain while it is limited to ~650 mb east of the mountains thus producing the solenoidal field which generates the thermally-direct circulation accompanying the new bouyancy perturbation. One can see in the cross sections the evolution of this second bouyancy perturbation into a ducted gravity wave after 2000 UTC. This perturbation is following downstream behind the adiabatically-generated feature which is approaching CCOPE at approximately the same time that the perturbation upstream is becomming organized. *Thus, two dominant waves are generated in the smooth terrain simulation independent of latent heating.*

The 500 mb wind and height fields depicted in Figures 26 - 28 indicate the slowness with which the second bouyancy perturbation and its accompanying wind surge are progressing

eastward. The average phase velocity of this feature being ~50 km/hr at the 500 mb level over the 10 hour period from 2000 UTC through 0600 UTC 12 July. This slow speed of movement is not totally consistent with the simulated duct structure evident from the vertical cross sections depicted in Figure 27. By 0000 UTC, there is an extraordinary increase in static stability in the vertical at ~ 6 km elevation over eastern Montana. This simulated stable layer extends to ~9 km which is slightly higher in elevation and deeper than the observed 0009 UTC Knowlton, Montana (KNO) sounding depicted in Koch and Dorian (1988). The base of the simulated stable layer is juxtapositioned with a critical layer assuming the observed primary wave phase velocity during episode II ~ $17ms^{-1}$. Calculations employing the following equation from Koch and Dorian (1988) for the wave phase velocity as a function of N and the depth of the duct:

$$c \leq 2ND/\pi + U \qquad (I.3)$$

employing simulated fields indicate a value of ~22 ms^{-1} for the gravest mode. Hence, the simulated waves are slightly slower than both the observed modes and the theoretical prediction based on the duct structure.

Ascent accompanying the simulated thermal ridge at 700 mb produces a second region of saturated fluid just upstream from the second bouyancy perturbation between 1800 UTC and 2100 UTC as can be seen in Figure 29. Thus, as was the case with the first bouyancy perturbation, the absence of latent heating in the numerical model is likely restricting the development of companion bouyancy perturbations to the adiabatic feature during episode I and the sensible heat flux-generated bouyancy perturbation during episode II.

3) Environment for the Generation of the MCS

The environment for the generation of the massive mesoscale convective system which develops just after 0000 UTC 12 July 1981 as described by Koch and Golus (1988) and Koch *et al.* (1988) is simulated to be closely associated with the evolution of the first orogenic bouyancy perturbation and the MPS. Figure 30 depicts the 850 mb omegas, streamlines, isotachs, and

relative humidity fields over eastern Montana after the adiabatic bouyancy perturbation propagates from the lee slope area to CCOPE between 1400 UTC and 2100 UTC and then interacts with the lower branch of the MPS during the 1800 UTC through 0000 UTC period. Quite evident is the development of the mesocyclone which takes shape just southwest of CCOPE by 0000 UTC. It is at this time that the low-level flow and relative humidity fields change abruptly with the development of a south-southeasterly low-level jet directed towards CCOPE which results in an explosion of upward motion and increasing relative humidity. This circulation is apparent at 700 mb by 2100 UTC as the low-level jet which formed the adiabatic bouyancy perturbation earlier, i. e., before 1200 UTC over southwestern Montana, has propagated to the border region of Montana and North Dakota producing strong low-level convergence, ascent, and a saturated environment over western North Dakota after 0000 UTC as is depicted in Figure 31.

The mass fluxes producing the mesolow and low-level jet are the result of the modification of the first adiabatic bouyancy perturbation by surface sensible heat flux as it propagated towards CCOPE. This produces low-level pressure falls and explosive inflow and upward motions over western North Dakota and eastern Montana shortly after 0000 UTC as can be seen from the 850 mb winds and 700 mb ascent and vertical velocity fields which are depicted in Figures 31-32. The development of this mesolow and the explosive development of the mesoscale convective system over and just east of CCOPE are observed as can be seen from the surface and satellite observations from Koch *et al.* (1988) which are depicted in Figure 33. These observations indicate the development of a low pressure area over southcentral Montana southwest of BIL before 1800 UTC which propagates to CCOPE by 2300 UTC and interacts with a prexisting inverted trough. There is every indication from the model simulation that the downslope heated air between 700 mb and 850 mb is forced up and over the upslope flow from the south-southeast at and below 850 mb. This may account for the extraordinary amount and size of hail observed during the mesoscale convective system over western Montana. What is occurring here represents the interaction between the low-level inflow accompanying the lower branch of the MPS which develops after 1800 UTC, is directed westward, and is also directed upslope and the remnants of the lower

branch of the secondary jet which developed over the wave generation region more than 12 hours earlier and is directed downslope (note Figure 35). The resultant low-level jet (MCS LLJ) forced by the merger of the secondary LLJ and the lower branch of the MPS transports moisture and organizes convergence between CCOPE and the western Dakotas thus producing the explosive growth of the tongue of high 700 mb relative humidity over this region by 0000 UTC as can be seen depicted in Figures 31 and 35.

The signal of the amplifying mesolow is not limited to the lower troposphere in the numerical simulation as the propagating bouyancy perturbation passes over CCOPE just before 0000 UTC. Even at 300 mb the wind perturbation is divergent, thus aiding in the low-level pressure falls. After 0000 UTC, the surface sensible heat fluxes accompanying the second orogenic bouyancy perturbation act to maintain the positive height anomaly over the gravity wave generation region over southwestern Montana, northwestern Wyoming, and eastern Idaho. The jet maintains a highly unbalanced structure over this region as is indicated by the evolution of the ageostrophic wind field at 300 mb after 0000 UTC as can be seen depicted in Figure 34. This will insure the generation of additional gravity waves over this region during the final hours of the simulation. The imbalances in this wave generation region are, by far, the largest produced in this simulation with huge ageostrophic wind components resulting in Rossby number values well in excess of 1.0. The magnitude of unbalanced flow reflects the interaction aloft between the upper branch of the MPS with the prexisting unbalanced secondary jet streak. Thus, two regions of geostrophic adjustment are occurring within the observed gravity wave generation region at the same time (note Figure 35).

d) Summary and Conclusions

The smoothed terrain Control-B simulation indicates a complex multiscale sequence of adjustments which produce many of the mesoscale phenomena observed over, upstream, and downstream from the CCOPE mesonetwork on 11 and 12 July 1981. The observed mesoscale phenomena include: 1) the development of a secondary upper-level cloud plume indicative of a

secondary jet streak to the southeast of the primary jet streak by 0900 UTC 11 July, 2) a sequence of gravity waves which are generated over extreme southwestern Montana on or about 1200 UTC - 1500 UTC 11 July, 3) a second sequence of gravity waves generated in the same region approximately 6 hours later, 4) a mesocyclone over eastern Montana on or before 0000 UTC 12 July 1981, and 5) a mesoscale convective complex over much of North Dakota and South Dakota which forms shortly after 0000 UTC 12 July and produces copius hail. The simulated processes resulting in analogous phenomena can be subdivided into a sequence of stages each of which is 3-6 hours in length commencing just after 0000 UTC 11 July 1981 and ending just before 0600 UTC 12 July 1981.

Stage I involves the geostrophic adjustment of the wind to the pressure field within the mid-upper troposphere 3-6 hours after the model is initialized at 0000 UTC 11 July 1981. As a subsynoptic scale wind maximum encounters the rapidly increasing cross-stream pressure gradient force over northern Idaho and northwestern Montana, air parcels are accelerated to the left of the stream. This increase in the meridional wind component is followed by an adjustment of the zonal wind component which acts to accelerate the flow nearly 180 degrees relative to the initial acceleration. The increase in mid-upper tropospheric flow to the southeast of the upper-level stream produces a shear zone over southcentral Montana oriented orthogonal to the original jet axis and displaced at least 200 km to its southeast.

Stage II involves frontogenesis aloft 3 or more hours later in response to the new ageostrophic flow accompanying the initial geostrophic adjustment process. The increase in mass on the right flank of the original stream induces nonuniform sinking motions over southern Montana, southeastern Idaho, and northern Wyoming. The nonuniform adiabatic compression along a southeast-northwest axis induces differential warming within the mid-upper troposphere. Ageostrophic shearing deformation fortifies the frontogenesis by producing midlevel cold advection over central Montana which is stronger than over southern Montana. Finally, the positive and negative height anomalies within the atmospheric column are further enhanced by radiative cooling within the planetary boundary layer over northwestern Montana. These processes

conspire during this stage to produce a new deep front and secondary mass perturbation along the gradient of the new thickness anomaly fields ~250 km to the southeast of the original deep jet/baroclinic zone.

Stage III occurs as the mid-upper tropospheric secondary front/mass perturbation induces a secondary adjustment in the wind field over the observed gravity wave generation region near the borders of Idaho, Montana, and Wyoming. This new sequence of adjustments acts to produce a cross-stream ageostrophic flow directed to the left of the stream followed by a rightward cross-stream directed flow. These adjustments are highly focussed over the wave generation region, i. e. the Wyoming, Idaho, and Montana border region by 0900 UTC.

Stage IV unfolds as the integrated mass fluxes accompanying Stage III produce nonuniform surface pressure falls resulting in a surface pressure trough, an increased north-northeastward directed low-level pressure gradient force, and a subsequent secondary low-level jet which is coupled to the secondary exit region indirect circulation. This low-level jet is directed towards the upslope terrain near the gravity wave generation region. Air parcels within this jet will be forced to ascend from the Snake River Plain over southeastern Idaho up the elevated terrain including the Absaroka Mountain Range bordering Idaho, Montana, and Wyoming.

The first gravity wave episode is ushered in during Stage V wherein the upslope cooling accompanying the low-level jet over the Wyoming, Idaho, Montana border region and downslope warming further northeast over southwestern Montana produce an along-stream mountain wave which is analogous to a bouyancy perturbation or along-stream front. This feature is well-developed in the simulation after 1200 UTC and begins to propagate downstream towards the CCOPE mesonetwork region over the next several hours. Most interesting is the fact that the ascending part of the propagating wave produces saturation at low-levels directly behind the wave. This indicates that future simulations which include latent heating may generate dual primary waves as opposed to the single wave simulated during this episode. As it propagates, it produces some characteristics analogous to the primary gravity wave during the first wave episode observed by Koch and Golus (1988). However, despite the fact that multiple surface pressure oscillations and

multiple mid-upper tropospheric wind surges accompany this feature it still differs in many respects from the first episode primary waves which were observed. These differences include wave length, phase speed, and vertical structure.

The second simulated gravity wave episode is triggered during Stage VI approximately 6 hours after the first wave and in approximately the same location. This second wave is the result of simulated differential surface sensible heating between the elevated terrain and the nearby valley regions. This produces another bouyancy perturbation/front oriented along the stream which has a somewhat longer wavelength than the first terrain-induced bouyancy perturbation. This feature then propagates downstream towards CCOPE less rapidly than the first bouyancy perturbation. It too is accompanied by a region of strong upward motion and adiabatic cooling which reaches low-level saturation quite rapidly. While it is accompanied by a wind surge aloft, unlike the first episode wave it is not accompanied by a secondary wind surge. One very interesting aspect of this feature is the fact that the unbalanced flow aloft over the wave generation region accompanying the secondary jet is synergistically reinforced by the elevated sensible heating which modifies the mid-upper tropospheric pressure gradient force due to the thickness increases within the secondary jet's exit region. Thus, the formation of the upper branch of the MPS acts on a region which is already experiencing geostrophic adjustment, thus agravating the imbalances even further.

Finally, Stage VII results after 2100 UTC as the first orogenic bouyancy perturbation approaches the region near CCOPE. The low-level sensible heating induces pressure falls accompanying the propagating wave resulting in the development of a north-northwestward directed low-level jet near the border region of Montana, South Dakota, and North Dakota. The 850 mb mesocyclone formed by these processes over CCOPE is the focal point for strong ascending motions and column saturation. Furthermore, the strong low-level south-southwesterly 700 mb jet is transporting very warm dry air above the 850 mb jet which is transporting warm moist air northwestward. This results in the strong lifting over western North Dakota of air masses of rapidly varying thermodynamical characteristics which is appropriate for widespread convection likely producing large hail as was observed in nature after 0000 UTC in this region.

The resultant of these two low-level jets forms a narrow moist conveyor belt over CCOPE and the western Dakotas which transports moisture into the region of the observed MCS.

In summary, a smoothed-terrain dry simulation with the nested-grid GMASS model has revealed many important aspects of the processes which resulted in the generation of gravity waves in the region and time when and where they were observed. However, the vertical structure, number, and characteristics of the waves are still quite different from observed waves as diagnosed from Koch *et al.* (1988) and Koch and Golus (1988) thus necessitating future improved simulations. However, as noted in the schematics depicted in Figures 17 and 35, this control simulation has produced substantial insight into processes which occur on many spatial scales over a 30 hour time period thus allowing one to draw promising inferences as to the mechanisms for the complex processes which occurred in nature during the CCOPE case study.

e) Current and FY94 Planned Research Simulation Experiments

The Control-B simulation experiment strongly indicates the importance of geostrophic adjusment, adiabatic orographic forcing, and surface sensible heat fluxes in producing the mass/momentum perturbations which were observed during CCOPE. Before adding the complicating factor of latent heat release we will be performing a series of simulations during FY94 which are designed to focus on the sensitivity of the model to these three fundamental forcing mechanisms. Therefore, the following three simulations will be performed during the remainder of FY94 to better diagnose the role of the geostrophic adjustment processes, terrain, and surface sensible heat fluxes in the generation of the CCOPE mesocirculations:

1) A nested-grid GMASS simulation employing the highest resolution terrain possible, i. e., terrain which does not produce numerical instabilities but contains height gradients several times larger than those included in the smooth terrain Control-B simulation, in an effort to diagnose the structure of orogenic features as a function of terrain resolution,

2) A nested-grid GMASS simulation employing no terrain variation at all to determine to what extent background geostrophic adjustment accompanying the jet streak alone can organize the environment for wave genesis independent of terrain forcing, and

3) A nested-grid GMASS simulation with no surface sensible heat fluxes or related radiational forcing in an effort to determine how critical they are in modifying the orogenic wave development processes.

Should time and resources permit, we will begin addressing the role of latent heating on wave genesis and evolution. However, it is felt that a meso-γ scale nonhydrostatic cloud model nested within GMASS may be the best vehicle to sort out the latent heating effects.

During FY94 we will also be preparing a two-part journal article based on these simulations diagnosing the role of all three primary forcing functions in the development of the observed CCOPE mesoscale circulation systems. We will also be preparing two conference presentations and preprints based on these simulation studies; one to be presented at the forthcoming 10th AMS Conference on Numerical Weather Prediction and one to be presented at the forthcoming 6th AMS Conference on Mesoscale Processes to be held in Portland, Oregon during July 1994. These diagnoses and analyses will then be utilized to prepare a final project report.

Part II. Linear Theory and Theoretical Modeling

(a) Summary of FY93 Theoretical Work

During FY93, the theoretical aspects of the project have focused on understanding the nature of the *ageostrophic* circulations which are produced in idealized models of the atmosphere in which the troposphere is modeled in one of two ways. The first model assumes that the lower atmosphere can be represented as a single layer of homogeneous fluid whose upper surface is free to exhibit vertical displacement. Two-dimensional internal convergence (divergence) occuring during the adjustment to an asymptotic equilibrium state from an ageostrophic initial state whose

momentum structure is representative of a midlatitude localized zonal wind anomaly will cause the free upper surface of the homogeneous atmosphere to rise (fall), and therefore the response can be viewed as being physically three-dimensional. The second model assumes that the troposphere can be represented by an unbounded continuously stratified Boussinesq fluid of constant Brunt-Vaisala frequency N, where the vertical gradient of the basic state potential temperature profile allows for the existence of vertically propagating internal inertia-gravity waves. The homogeneous model is similar to the one employed in the linear theory of Barwell and Bromley (1988), and is the simplest model which retains the basic physics esstential for an investigation of geostrophic adjustment processes in planetary atmospheres (Blumen, 1972; Gill, 1982). The continuously stratified model is similar to the one employed in the recent analytical study by Luo and Fritts (1993). Our models however, are different in one very important aspect in that the basic state is *not motionless*, but rather consists of a *geostrophically balanced barotropic flow*. Although a very crude approximation to real midlatitude synoptic scale flows, this type of basic state is, in our opinion, more representative of the environment in which localized zonal wind anomalies are commonly found in the midlatitudes. Therefore, our theory generalizes the methodology commonly employed in the classical or traditional treatment of geostrophic adjustment problems by (i) including an initial state more representative of the three-dimensional structure of midlatitude jet streaks, and (ii) the *physical mechanisms* of linearized perturbation vorticity advection - $\mathbf{U}\cdot\nabla\zeta'$ and temperature advection - $\mathbf{U}\cdot\nabla\theta'$ associated with *the subsequent motions of the equilibrium state after the ageostrophy of the initial state is removed from the source region by the transient inertia-gravity waves*. These upper-level forcing mechanisms are known to play a crucial role in the life cycle of midlatitude baroclinic waves, for example (Holton, 1992; Bluestein, 1993a, b).

The methods of small-amplitude perturbation theory applied to the linearized wave equations governing the response in a homogeneous atmosphere has revealed that in the absence of orographic and external momentum forcing, the perturbation potential vorticity distribution characterizing the initial *disturbance* state of the barotropic current (which, in general, is ageostrophic) is the inhomogeneous source term which governs the spatial and temporal evolution

of the zonal and meridional *geostrophic* wind perturbations. In the absence of forcing, no contribution is made to the perturbation zonal and meridional ageostrophic winds from the initial disturbance to the barotropic basic state. Therefore, the ageostrophic winds are comprised solely of transient inertia-gravity waves whose phase speeds and group velocities are modified by the basic state flow, and no long-lived steady-state ageostrophic motions develop near the jet core, since the asymptotic equilibrium state is one of pure nondivergent, geostrophic balance between the mass and momentum fields. The geostrophic jet is then advected downstream from the initial location occupied by the ageostrophic jet by the basic state flow, and becomes the mechanism for linearized geostrophic vorticity advection, $-\mathbf{U}\cdot\nabla\zeta_g$ associated with the moving jet. This downstream advection constitutes the *steady-state response* within the context of linear theory.

Since a homogeneous barotropic atmosphere lacks the physical mechanism of potential vorticity (PV) advection by the basic state thermal wind which is responsible for the forcing of quasi-geostrophic vertical motions in a rotating baroclinic flow (Zehnder and Keyser, 1991; Holton, 1992), we investigate the ageostrophic circulations and vertical motions forced by a prescribed traveling external momentum forcing, which is taken to represent a localized zonal wind anomaly or jet streak propagating at the constant speed c along the +x-axis through a uniform barotropic current of magnitude U, which itself is taken to be representative of the basic state synoptic scale flow within which the jet streak is embedded. Two types of external momentum forcing are investigated:

$$F_x(x,y,t) = \frac{u_{jet}}{\tau}\left[\frac{(x-ct)^2}{a_x^2} + \frac{y^2}{a_y^2} + 1\right]^{-3/2}, \qquad \text{(II.1)}$$

$$F_x(x,y,t) = U^* \frac{\partial}{\partial x}\left[u_{jet}\left\{\frac{(x-ct)^2}{a_x^2} + \frac{y^2}{a_y^2} + 1\right\}^{-3/2}\right]. \qquad \text{(II.2)}$$

Eq. (II.1) is chosen in order to investigate the forced geostrophic adjustment dynamics associated with an independently propagating jet in a uniform barotropic flow, while Eq. (II.2) is chosen to

be more representative of the forcing *the alongstream gradients associated with a propagating jet streak impose on the slower moving basic state flow*, $|U| \leq |c|$ (Bluestein, 1986).

Linear theory shows that the forced response in a reference frame translating at the uniform speed c consists of primarily three mechanisms: (1) the generation of a transient inertia-gravity wave radiation field which removes a portion of the ageostrophy imposed by the divergence of the external forcing, (2) the generation of a potential vorticity (PV) anomaly which is advected downstream of the forcing region at the relative speed (U-c), and (3) a steady-state circulation confined to the forcing region which consists of both geostrophic and ageostrophic components. It is found that the *PV anomaly* generated by the external momentum forcing given by Eq. (II.1) constitutes a geostrophically balanced zonal jet ($u' > 0$) with compensating zonal counter currents ($u' < 0$) north and south of the jet core, while the steady-state response confined to the forcing region consists of a zonal jet (counter jet) in the exit (entrance) region of the stationary external momentum forcing. The steady ageostrophic winds within the forcing region give rise to a two-cell pattern of vertical motion, with rising (sinking) on the anticyclonic (cyclonic) side of the forcing center, similar to a jet-induced thermally direct circulation in a baroclinic atmosphere. An observer in a non-translating reference frame would see the steady-state portion of the response associated with the external momentum forcing propagate through the uniform barotropic current at the speed c, and therefore these mesocirculations would be identified by this observer as those associated with a propagating jet streak. Although the momentum forcing given by Eq. (II.1) can generate a PV anomaly whose structure is similar to the asymptotic equilibrium state of the initial value problem, the ageostrophic circulations and accompanying vertical motions are not representative of those inferred from quasi-geostrophic dynamics applied to jet streaks in rotating baroclinic atmospheres.

Linear theory applied to the external momentum forcing given by Eq. (II.2), which is taken as a first approximation to represent the acceleration (deceleration) the alongstream gradients associated with a propagating jet streak produce on the basic state flow in which it is embedded, shows that a geostrophically balanced zonal counter jet ($u' < 0$) with compensating zonal jets north

and south of the core of the counter jet is the type of PV anomaly generated by this type of prescribed forcing. The steady-state response within the forcing region consists of an isolated region of positive zonal winds, with confluence (diffluence) in the jet entrance (exit) region. Most dramatic, however, are the ageostrophic winds and associated vertical motions, which consists of a four-cell pattern with rising (sinking) in the right rear and left front quadrants (left rear and right front quadrants) surrounding the jet core. This result shows that the alongstream gradient associated with a propagating jet streak, which is represented by the external momentum forcing given by Eq. (II.2), provides the physical mechanism of *forced quasi-geostrophic jetogenesis* in a homogeneous barotropic atmosphere. Our linear theory has therefore shown that jet streaks *are not necessarily restricted* to exist only in baroclinic flows. We feel that these theoretical results help to bridge the gap which currently exists between the classical geostrophic adjustment theory of very idealized initial states whose mass and momentum structures are not representative of localized zonal wind anomalies, and the geostrophic adjustment processes associated with midlatitude jet streaks inferred from detailed analysis of observational datasets (Koch and Golus, 1988, Koch *et al.* 1988, Koch and Dorian, 1988, Koch *et al.* 1993) and from nonlinear numerical models simulating complex baroclinic severe storm producing environments (Kaplan *et al.* 1993).

Derivation of the forced geostrophic and ageostrophic wave equations further shows that (i) If the external momentum forcing is nondivergent, then it makes no contribution to the evolution of the geostrophic winds, whose steady-state is characterized solely by the total linearized perturbation potential vorticity (PV) distribution (q') which defines the initial disturbed state of the barotropic current. (ii) If the divergence of the external momentum forcing is equal to -fq', then the external momentum forcing *destroys* the PV distribution characterizing the disturbance state of the barotropic flow. In a sense, an external momentum forcing of this form tends to remove any PV anomalies, and therefore the initial PV distribution of the atmosphere becomes more homogeneous. (iii) In an externally forced uniform barotropic atmosphere, if the meridional (zonal) gradient of the quantity $(q' + F_\delta/f)$ (which physically represents the linear superposition between the PV distribution characterizing the initial disturbance of the basic state flow and the PV

anomaly generated by the divergence of the external momentum forcing) vanishes, then *no non-trivial* equilibrium state can be obtained by the zonal (meridional) component of the geostrophic wind.

The effects of nonlinearity on the adjustment to an asymptotically balanced equilibrium state is investigated by solving the initial value problem numerically with a simple numerical model which integrates the nonlinear shallow water equations governing the geostrophic adjustment dynamics of a homogeneous barotropic atmosphere. Although the early stages of the response are similar to that predicted by the analytical solution of the linear initial value problem, the primary effect of nonlinearity is to transform the geostrophic jet into a quasi-geostrophic jet by inducing northerly (southerly) directed ageostrophic meridional winds in the jet entrance (exit) region due to existence of the nonlinear inertial-advective or alongstream gradient $u_g'\partial u_g'/\partial x$. These meridional wind perturbations create a mass adjustment which transfers mass from the anticyclonic (cyclonic) side of the jet to the cyclonic (anticyclonic) side of the jet in the entrance (exit) region. The resulting four-cell divergence pattern is similar to that inferred to be associated with baroclinic jet streaks from quasi-geostrophic theory (Bluestein, 1986, 1993a, b). However, due to mass continuity through the constraints imposed by the Taylor-Proudman theorem for rotating homogeneous flows, *the four-cell pattern of vertical motion* characterizing the steady-state response to the nonlinear initial value problem *is reversed* from that obtained from the linear forced problem, and that commonly inferred to be associated with jet streaks in a baroclinic flow. This is to say that an indirect (direct) ageostrophic circulation exists in the jet's entrance (exit) region rather than the customary direct (indirect) circulation. Nevertheless, these patterns of ageostrophic motion are consistent with the physics of homogenoeus barotropic flows, and therefore we classify the steady-state equilibrium solution to the nonlinear initial value problem as *barotropic jetogenesis.*

Similar work has been done for a barotropic flow in a continuously stratified Boussinesq atmosphere, and the results from this phase of our research which generalizes the continuously stratified results presented in the May semi-annual report along with a full elaboration of the response in barotropic homogeneous flows will be presented in Weglarz (1993), which currently is

in preparation. In addition, two papers are being planned for submission to refereed journals and the upcoming 6th AMS Conference on Mesoscale Processes which will contain the core of the theoretical results to be presented in Weglarz (1993) and in the final project report.

(b) Proposed FY94 Research

Although the work to date presented in the previous section has been offered as a preliminary attempt to fill the gap which currently exists between our knowlege of basic jet streak dynamics inferred from the theoretical geostrophic adjustment physics of very idealized models of the atmosphere and the evolution of these mesoscale momentum sources and their influence on the regional severe weather environment predicted by nonlinear primitive equation numerical models initialized with real observational data using fairly sophisticated numerical techniques, closely related topics which generalize the theoretical results outlined here have also been addressed. While the work associated with some of these topics has already been completed, some has just begun, and it is not the purpose here to expound upon these results. Rather, this section provides the reader with some indication of the direction in which future work is currently being undertaken in order to approach the problems associated with jet streak dynamics inferred from observational data.

1. Future Work on Homogeneous Atmospheres

The linear geostrophic adjustment of a rotating homogeneous atmosphere to a three-dimensional ageostrophic (unbalanced) zonal wind anomaly whose basic state is one of uniform barotropic flow when there exists shallow surface orography has been completed. The orography considered has been an infinite two-dimensional mountain ridge oriented perpendicular to the basic state current, and a three-dimensional isolated, bell-shaped topographic barrier. Using the method of small-amplitude perturbation theory, the results obtained consist of the superposition between the solution to the linear initial value problem outlined in Section II(a), and the solution to the linear initial value problem due to orographic forcing of the basic state barotropic flow alone in the absence of an initial PV anomaly. Although these results have increased our understanding of *the perturbation of mid-upper tropospheric jet streaks due to significant mesoscale orographic forcing*, a more realistic scenario of the orographically forced perturbations to a quasi-geostrophic jet streak can be obtained only when the ageostrophic circulations not present with linear, non-divergent,

geostrophically balanced zonal wind anomalies exist. This problem can easily be addressed through idealized theoretical modeling studies using a simple primitive equation shallow water model (Weglarz, 1993). The methodology will be as follows: (1) Introduce an ageostrophic (unbalanced) zonal wind anomaly whose horizontal zonal and meridional scales are much smaller than the Rossby deformation radius of the homogeneous model atmosphere. (2) Allow the model physics (nonlinearity) to produce a *quasi-geostrophically balanced* jet streak, with its associated ageostrophic entrance and exit region circulations. (3) Introduce the QG-balanced jet streak upstream of the orography as the initial state in an otherwise uniform, barotropic basic state current. (4) Investigate both the linear and nonlinear dynamics as the jet streak is advected towards and over the topography. (5) Investigate *the effects of horizontal shear on* the evolution to geostrophic and quasi-geostrophically balanced barotropic *jet streak genesis* in addition to the orographic perturbation of the jet by allowing the basic state flow to possess a non-uniform meridional (north-south) structure. *This type of basic state will allow for a more correct representation of the midlatitude planetary jet stream.* The results of this study will be directly applicable to the role jet streaks play as *forcing mechansims of lee cyclogenesis* in idealized barotropic atmospheres, in addition to allowing an investigation of the perturbation of the jet stream due to mesoscale orographic barriers.

2. *Future Work on Continuously Stratified Atmospheres*

The adjustment to both geostrophic and quasi-geostrophic balanced jet streak genesis in a rotating continuously stratified baroclinic atmosphere whose basic state consists of *vertically sheared* zonal and meridional winds will be investigated both theoretically and numerically. The results from this study will generalize the results concerning the fundamental adjustment physics of barotropic atmospheres in addition to generalizing the two-layer rigid lid model results of Duffy (1990). Because the physical mechanism responsible for the maintainence of the ageostrophic entrance and exit region circulations, namely the baroclinicity of the basic state, is present, the

linear and nonlinear initial value problems will be studied first. The response to propagating external momentum forcings will then be considered to make the study complete.

Work on the role played by mid-upper tropospheric jet streaks in proposed quasi-geostrophic theories of lee (Smith, 1984, 1986) and quasi- and semigeostrophic theories of coastal (Lin, 1989, 1990, 1992) cyclogenesis has been started. Although the extension of these theories will not be able to address the role played by inertia-gravity waves due to the imposed constraints of quasi- or semi-geostrophy, the *baroclinic waves* produced by the propagating upper level jet streak can be studied by investigating the linear initial value problem. Because the indirect circulations associated with the jet streak play a crucial role in connecting the upper and lower tropospheric dynamics, both the QG omega and Sawyer-Eliassen circulation equations, which were neglected by Smith (1984, 1986) and Lin (1989, 1990, 1992), must be solved. The quasi-geostrophic results can be generalized by investigating the effects of ageostrophic advection using a simple semigeostrophic model (Lin ,1990). The initial potential vorticity distribution associated with an upper-level jet streak has already been incorporated into this model. The results from these theoretical studies will aid in our understanding of the basic physics provided by an upper level forcing mechanism in both quasi- and semigeostrophic models of idealized lee and coastal cyclogenesis. The role played by inertia-gravity wave dynamics will be addressed through the use of a simple three-dimensional continuously stratified terrain-following primitive equation model (Weglarz, 1993).

Results from a recent case study of the meso-β scale environment associated with the isolated Raleigh tornado outbreak of 28 November 1988 from the Goddard Mesoscale Atmospheric Simulation System (GMASS) numerical weather prediction model by Kaplan *et al.* (1993) seem to indicate that convectively driven or diabatic forcing mechanisms associated with the latent heat release of hypothesised wave-CISK supported midlatitude squall lines in the entrance region of the meso-α to synoptic scale upper tropospheric jet streak were responsible for perturbing the mass field, which subsequently led to the development of a meso-β scale wind/momentum surge in the upper levels of the thermally direct entrance region circulation

through geostrophic adjustment dynamics. Similar findings by Maddox *et al.* (1981) and Johnson and Keyser (1984) have shown that mid-level tropospheric latent heat release associated with a mesoscale convective complex (MCC) in both dry and moist atmospheres can significantly influence the pre-existing upper-level synoptic scale winds, as well as the classical ageostrophic jet streak entrance and exit region circulations, respectively. However, due to the complexity of the baroclinic environments simulated by their numerical models, it is difficult to identify the primary physical mechanisms associated with diabatic forcing of pre-existing, quasi-balanced midlatitude jet streaks. Our understanding of the basic physics of this process can be enhanced through idealized theoretical modeling studies and will generalize the linear theoretical results of mechanically forced jet streak genesis presented here by investigating the fundamental physics of diabatically forced jet streak genesis.

Perhaps the ultimate application of the theoretical work presented here which differs from that outlined in the preceeding paragraphs is to address *the problem of inertia-gravity wave generation by geostrophic adjustment processes as a mature, quasi-balanced jet streak propagates toward the ridge axis of a pre-existing midlatitude baroclinic wave*, a common signature of upper-level dynamics accompanying many types of severe weather producing environments (Uccellini and Koch, 1987). The solution to this problem must involve methods which view the jet streak not as simply a perturbation in the basic state baroclinic flow, but rather as part of a fully three-dimensional baroclinic basic state possessing both *horizontal and vertical shear* which is subsequently forced by inherently nonlinear inertial-advective processes. Again, it appears that until analytical methods powerful enough to solve the associated wave equations are developed, the problem will most likely be handled by numerical integration of the primitive equations. Work on generalizing the simple primitive equation model used in this project to handle a fully three-dimensional balanced baroclinic basic state has already begun. The first approach will be to incorporate analytical relations which capture the essential quasi- or semi-geostrophic features of the basic state dynamical fields (Fritsch *et al.*, 1980), which can then be generalized to more sophisticated numerical techniques such as solution of the nonlinear balance equation or

incorporating nonlinear normal mode initialization (Haltiner and Williams, 1980; Holton, 1992) to provide an optimum balance between the initial mass and momentum fields.

References

Barwell, B. R., and R. A. Bromley, 1988: The adjustment of numerical weather prediction model to local perturbations. *Quart. J. Roy. Meteor. Soc.*, **114**, 665-689.

Bluestein, H. B., 1986: Fronts and jet streaks: A theoretical perspective. *Mesoscale Meteorology and Forecasting*. P. S. Ray, Ed. Amer. Meteor. Soc., 1986.

--------, 1993a: *Synoptic-Dynamic Meteorology in Midlatitudes. Volume I. Principles of Kinematics any Dynamics*. Oxford Univ. Press, New York.

--------, 1993b: *Synoptic-Dynamic Meteorology in Midlatitudes. Volume II. Observations and Theory of Weather Systems*. Oxford Univ. Press, New York.

Blumen, W., 1972: Geostrophic adjustment. *Rev. Geophys. Space Phys.*, **10**, 485-528.

Duffy, D. G., 1990: Geostrophic adjustment in a baroclinic atmosphere. *J. Atmos. Sci.*, **47**, 457-473.

Fritsch, J. M., E. L. Magaziner, and C. F. Chappell, 1980: Analytic initialization for three-dimensional models. *J. Appl. Meteor.*, **19**, 809-818.

Gill, A. E., 1982: *Atmosphere-Ocean Dynamics*. Academic Press, 662 pp.

Haltiner, G. J., and R. T. Williams, 1980: *Numerical Prediction and Dynamic Meteorology*, 2nd ed., John Wiley and Sons, New York, 477 pp.

Holton, J. R., 1992: *An Introduction to Dynamic Meteorology*. Academic Press, Inc.

Johnson, D. R., and D. A. Keyser, 1984: Effects of diabatic heating on the ageostrophic circulation of an upper tropospheric jet streak. *Mon. Wea. Rev.*, **112**, 1709-1724.

Kaplan, M. L., and D. A. Paine, 1977: The observed divergence of the horizontal velocity field and pressure gradient force at the mesoscale: Its implications for the parameterization of three-dimensional momentum transport in synoptic-scale numerical models. *Beitr. Phys. Atmos.*, **50**, 321-330.

--------, J. W. Zack, V. C. Wong, and J. J. Tuccillo, 1982: Initial results from a mesoscale atmospheric simulation system and comparisons with the AVE-SESAME I data set. *Mon. Wea. Rev.*, **110**, 1564-1590.

--------, R. A. Rozumalski, R. P. Weglarz, and Y.-L. Lin, 1993: Numerical simulation studies of the role of prolonged wave-CISK in contributing to the rotation and buoyancy accompanying the isolated Raleigh tornado outbreak. *17th AMS Conf. on Severe Local Storms*, 4-8 October, 1993, St. Louis, Missouri.

Koch, S. E., and R. E. Golus, 1988: A mesoscale gravity wave event observed during CCOPE. Part I: Multiscale statistical analysis of wave characteristics. *Mon. Wea. Rev.*, **116**, 2527-2544.

--------, R. E. Golus, and P. B. Dorian, 1988: A mesoscale gravity wave event observed during CCOPE. Part II: Interactions between mesoscale convective systems and the antecedent waves. *Mon. Wea. Rev.*, **116**, 2545-2569.

--------, and P. B. Dorian, 1988: A mesoscale gravity waveevent observed during CCOPE. Part III: Wave environment and probable source mechanisms. *Mon. Wea. Rev.*, **116**, 2570-2592.

--------, F. Einaudi, P. B. Dorian, S. Lang, and G. M.Heymsfield, 1993: A mesoscale gravity wave event observed during CCOPE. Part IV: Stability analysis and Doppler-derived wave vertical structure. *Mon. Wea. Rev.*, **121**, 2483-2510.

Lin, Y.-L., 1989: A theory of cyclogenesis forced by diabatic heating. Part I: A Quasi-geostrophic approach. *J. Atmos. Sci.*, **46**, 3015-3036.

--------, 1990: A theory of cyclogenesis forced by diabatic heating. Part II: A Semigeostrophic approach. *J. Atmos. Sci..*, **47**, 1755-1777.

--------, 1992: Dynamics of thermally forced mesoscale circulations. *Trends in Atmospheric Sci.*, **1**, 73-152.

Luo, Z., and D. C. Fritts, 1993: Gravity-wave excitation by geostrophic adjustment of the jet stream. Part II: Three-dimensional forcing. *J. Atmos. Sci.*, **50**, 104-115.

Maddox, R. A., D. J. Perkey, and J. M. Fritsch, 1981: Evolution of the upper tropospheric features during the development of a mesoscale convective complex. *J. Atmos. Sci.*, **38**, 1664-1674.

Smith, R. B., 1984: A theory of lee cyclogenesis. *J. Atmos. Sci.*, **41**, 1159-1168.

--------, 1986: Further development of a theory of lee cyclogenesis. *J. Atmos. Sci.*, **43**, 1582-1602.

Tripoli, G. J., and W. R. Cotton, 1989a: Numerical study of an observed orogenic convective system. Part 1: Simulated genesis and comparisons with observations. *Mon. Wea. Rev.*, **117**, 273-304.

--------, and --------, 1989b: Numerical study of an observed orogenic convective system. Part 2: Analysis of governing dynamics. *Mon. Wea. Rev.*, **117**, 305-328.

Uccellini, L. W., P. J. Kocin, R. A. Petersen, C. H. Wash, and K.F. Brill, 1984: The Presidents' Day cyclone of 18-19 February1979: Synoptic overview and analysis of the subtropical jet streak influencing the pre-cyclogenetic period. *Mon. Wea. Rev.*, **112**, 398-412.

--------, and S. E. Koch, 1987: The synoptic setting and possible energy sources for mesoscale wave disturbances. *Mon.Wea. Rev.*, **115**, 721-729.

Weglarz, R. P., 1993: Three-dimensional geostrophic adjustment of rotating homogeneous and continuously stratified atmospheres with application to the dynamics of midlatitude jet streaks. Ph.D. thesis, North Carolina State University, in preparation.

Whitaker, J. S., L. W. Uccellini, and K. F. Brill, 1988: A model-based diagnostic study of the explosive development phase of thePresidents' Day cyclone. *Mon. Wea. Rev.*, **116**, 2337-2365.

Zack, J. W., and M. L. Kaplan, 1987: Numerical simulations of the subsynoptic features associated with the AVE-SESAME I case. Part I: The preconvective environment. *Mon. Wea. Rev.*, **115**, 2367-2394.

Zehnder, J. A., and D. Keyser, 1991: The influence of interior gradients of potential vorticity on rapid cyclogenesis. *Tellus*, **43A**, 198-211.

List of Figures

Fig. 1: Location of (a) coarse mesh (16 km) and nested-grid (8 km) regions of integration ofthe GMASS numerical model employing a 223 x 146 x 30 matrix of grid points for the Control-B simulation. (b) NWS LFM smooth terrain representation over the region of the Control-B simulation.

Fig. 2: High resolution terrain representation over the same region as the Control-B simulation.

Fig. 3: Display region for horizontal cross sections for the coarse and nested-grid Control-B simulations. Line A and line B represent locations of vertical cross sections orthogonal to the jet stream from Spokane, Washington (GEG) to Rapid City, South Dakota (RAP) and parallel to the jet stream from Boise, Idaho (BOI) to Dickinson, North Dakota (DIK), respectively, which are employed for the coarse mesh simulation. These are shortened for the fine mesh simulation extenting from Missoula, Montana (MSO) to RAP for cross section A and Salmon, Idaho (SMN) to DIK for cross section B.

Fig. 4: Coarse mesh GMASS Control-B simulation of 500 mb and 300 mb height (m) and temperature (C) valid at (a-b) 0100 UTC and (c-d) 0300 UTC 11 July 1981.

Fig. 5: Coarse mesh GMASS Control-B simulation of 500 mb and 300 mb u-component (ms^{-1}) and v-component (ms^{-1}) isotachs valid at (a-d) 0200 UTC and (e-h) 0400 UTC 11 July 1981.

Fig. 6: Coarse mesh GMASS Control-B simulation of 500 mb and 300 mb u-component (ms^{-1}) and v-component (ms^{-1}) isotachs valid at (a-d) 0500 UTC and (e-h) 0700 UTC 11 July 1981.

Fig. 7: Coarse mesh GMASS Control-B simulation of 500 mb and 300 mb height (m) and temperature (C) valid at (a-b) 0600 UTC and (c-d) 0800 UTC and omega ($micrbs^{-1}$) valid at (e-f) 0500 UTC and (g-h) 0700 UTC 11 July 1981.

Fig. 8: Vertical cross sections A and B of coarse mesh GMASS Control-B simulation of potential temperature (K) and omega ($micrbs^{-1}$), and total wind velocity (ms^{-1}) isotachs valid at (a-d) 0600 UTC and (e-h) 0800 UTC 11 July 1981.

Fig. 9: Infrared satellite imagery valid at (a) 0600 UTC, (b) 0700UTC, (c) 0800 UTC, and (d) 0900 UTC 11 July 1981.

Fig. 10: Coarse mesh GMASS Control-B simulation of 850 mb and 700 mb height (m) and temperature (C) valid at (a-b) 0300 UTC and (c-d) 0900 UTC 11 July 1981.

Fig. 11: Coarse mesh GMASS Control-B simulation of 850 mb u-component (ms^{-1}) and v-component (ms-1) isotachs valid at (a-b) 0300 UTC and (c-d) 0900 UTC 11 July 1981.

Fig. 12: Nested-grid GMASS Control-B simulation of 500 mb, 300 mb, and 200 mb height (m) and temperature (C) valid at (a-c) 0900 UTC 11 July 1981.

Fig. 13: Nested-grid GMASS Control-B simulation of 500 mb total wind velocity vectors and isotachs (ms^{-1}) valid at (a) 0900 UTC and (b) 1200 UTC and 500 mb geostrophic wind velocity vectors and isotachs (ms^{-1}), ageostrophic wind velocity vectors and isotachs (ms^{-1}), u-component isotachs (ms^{-1}), and v-component isotachs (ms^{-1}) valid at (c-f) 1200 UTC 11 July 1981.

Fig. 14: Nested-grid GMASS Control-B simulation of 300 mb total wind velocity vectors and isotachs (ms^{-1}) valid at (a) 0900 UTC and (b) 1200 UTC and 300 mb geostrophic wind velocity vectors and isotachs (ms^{-1}), ageostrophic wind velocity vectors and isotachs (ms^{-1}), u-component isotachs (ms^{-1}), and v-component isotachs (ms^{-1}) valid at (c-f) 1200 UTC 11 July 1981.

Fig. 15: Nested-grid GMASS Control-B simulation of 200 mb total wind velocity vectors and isotachs (ms^{-1}) valid at (a) 0900 UTC and (b) 1200 UTC and 200 mb geostrophic wind velocity vectors and isotachs (ms^{-1}), ageostrophic wind velocity vectors and isotachs (ms^{-1}), u-component isotachs (ms^{-1}), and v-component isotachs (ms^{-1}) valid at (c-f) 1200 UTC 11 July 1981.

Fig. 16: Nested-grid GMASS control-B simulation of 700 mb total wind velocity vectors and isotachs (ms^{-1}) valid at (a) 0900 UTC and (b) 1200 UTC 11 July 1981

Fig. 17: a) Schematic describing early period (1200 UTC and before) circulations and forcing functions resulting in the development of the secondary upper and lower-level jet circulation over southwestern Montana, southeastern Idaho, and northwestern Wyoming in the first 12 hours of the Control-B simulation. Dashed lines surrounding - sign represent deep cold pool and negative height anomaly and solid lines surrounding + sign represent deep warm pool and positive height anomaly. LLJ refers to low-level jet location and AGEO refers to location of mean position of maximum cross-stream

ageostrophic wind vector between 500 mb and 200 mb. b) Schematic describing the early period (1200 UTC and before) mechanism producing the first orogenic bouyancy perturbation over southwestern Montana, southeastern Idaho, and northwestern Wyoming in response to the secondary low-level jet formation during the 0900 UTC - 1200 UTC time period. Dashed lines surrounding - sign represent shallow cold pool caused by orographic lifting and solid lines surrounding + sign represent shallow warm pool caused by orographic sinking. LLJ refers to low-level jet maximum position at various UTC times.

Fig. 18: Nested-grid GMASS Control-B simulation of 700 mb wind vectors and isotachs (ms^{-1}), omega ($micrbs^{-1}$), height (m) and temperature (C), and relative humidity (%) valid at (a-d) 1400 UTC 11 July 1981.

Fig. 19: Vertical cross section B of nested-grid GMASS Control-B simulation of potential temperature (K), omega ($micrbs^{-1}$), and total wind velocity (ms^{-1}) valid at (a-b) 1400 UTC UTC 11 July 1981.

Fig. 20: Infrared satellite imagery valid at (a) 1200 UTC and (b) 1300 UTC 11 July 1981.

Fig. 21: Vertical cross section B of nested-grid GMASS Control-B simulation of potential temperature (K), omega ($micrbs^{-1}$), and total wind velocity (ms^{-1}) valid at (a-b) 1600 UTC and (c-d) 1900 UTC 11 July 1981.

Fig. 22: Nested-grid GMASS Control-B simulation of hourly mean sea pressure (mb) and surface temperature (F) valid at (a) 1600 UTC and (b) 1900 UTC UTC 11 July 1981.

Fig. 23: Nested-grid GMASS Control-B simulation of 500 mb wind vectors and isotachs (ms^{-1}), height (m), and temperature (C) valid at (a-b) 1600 UTC and (c-d) 1900 UTC 11 July 1981.

Fig. 24: Nested-grid GMASS Contol-B simulation of 300 mb wind vectors and isotachs (ms^{-1}), height (m), and temperature (C) valid at (a-b) 1600 UTC and (c-d) 1900 UTC 11 July 1981.

Fig. 25: Nested-grid GMASS Control-B simulation of 300 mb and 200 mb ageostrophic wind vectors and isotachs (ms^{-1}) valid at (a-b) 1600 UTC 11 July 1981.

Fig. 26: Nested-grid GMASS Control-B simulation of 700 mb and 500 mb height (m) and temperature (C) valid at (a-b) 1800 UTC and (c-d) 2100 UTC 11 July 1981.

Fig. 27: Vertical cross section B of nested-grid GMASS Control-B simulation of potential temperature (K), omega (micrbs^{-1}), and total wind velocity (ms^{-1}) valid at (a-b) 1500 UTC, (c-d) 1800 UTC, (e-f) 2100 UTC, (g-h) 0000 UTC 11 July 1981. Vertical cross section B of coarse-grid GMASS Control-B simulation of potential temperature (K), omega (micrbs^{-1}), and total wind velocity (ms^{-1}) valid at 0300 UTC 12 July 1981 (i-j).

Fig. 28: Nested-grid GMASS Control-B simulation of 500 mb isotachs (ms^{-1}) and wind vectors valid at (a) 1800 UTC, (b) 2100 UTC, (c) 0000 UTC , 11 July 1981. Coarse-grid GMASS Control-B simulation of 500 mb isotachs (ms^{-1}) and wind vectors valid at 0300 UTC -12 July 1981 (d).

Fig. 29: Nested-grid GMASS Control-B simulation of 700 mb streamlines and omega (micrbs^{-1}), wind vectors and isotachs (ms^{-1}), and relative humidity (%) valid at (a-c) 1800 UTC and (d-f) 2100 UTC 11 July 1981.

Fig. 30: Nested-grid GMASS Control-B simulation of 850 mb streamlines and omega (micrbs^{-1}), wind vectors and isotachs (ms^{-1}), and relative humidity (%) valid at (a-c) 2100 UTC and (d-f) 0000 UTC 11-12 July 1981.

Fig. 31: Nested-grid GMASS Control-B simulation of 700 mb streamlines and omega (micrbs^{-1}), wind vectors and isotachs (ms^{-1}), and relative humidity (%) valid at (a-c) 0000 UTC 11 July 1981. Coarse-grid GMASS Control-B simulation of 700 mb streamlines and omega (micrbs^{-1}), wind vectors and isotachs (ms^{-1}), and relative humidity (%) valid at 0300 UTC 12 July 1981 (d-f).

Fig. 32: Coarse-grid GMASS Control-B simulation of 850 mb streamlines and omegas (micrbs^{-1}), wind vectors and isotachs (ms^{-1}), and relative humidity (%) valid at (a-c) 0300 UTC, and (d-f) 0600 UTC 12 July 1981.

Fig. 33: Observed surface analyses over and in proximity to the CCOPE mesonetwork valid at (a) 1900 UTC, (b) 2100 UTC, (c) 2300 UTC, and (d) 0100 UTC 11-12 July 1981. Infrared satellite imagery valid at (e) 0000 UTC, (f) 0200 UTC, (g) 0400 UTC, and (h) 0600 UTC 12 July 1981.

Fig. 34: Nested-grid GMASS Control-B simulation of 300 mb total wind vectors and isotachs (ms^{-1}) and 300 mb ageostrophic wind vectors and isotachs (ms^{-1}) valid at (a-b) 2100 UTC, (c-d) 0000 UTC 11 July 1981. Coarse-grid GMASS Control-B simulation of 300

mb total wind vectors and isotachs (ms^{-1}) and 300 mb ageostrophic wind vectors and isotachs (ms^{-1}) valid at 0300 UTC 12 July 1981 (e-f).

Fig. 35: Schematic describing the later period (after 1800 UTC) orogenically-forced adjustments. Multiple solid arrows represent the hourly position of the secondary 700 mb low-level jet maximum during the 0900 UTC 11 July 1981 through 0300 UTC 12 July 1981 time period. .Heating refers to the surface sensible heating maximum above the elevated terrain. Upper branch and lower branch arrows refer to the acceleration vector exerted on the upper tropospheric and lower tropospheric flows, respectively, by the differential heating-induced mountain-plains solenoid (MPS). The MCS LLJ arrow indicates the resultant flow vector forced by the joint forcing of the MPS lower branch and the secondary LLJ.

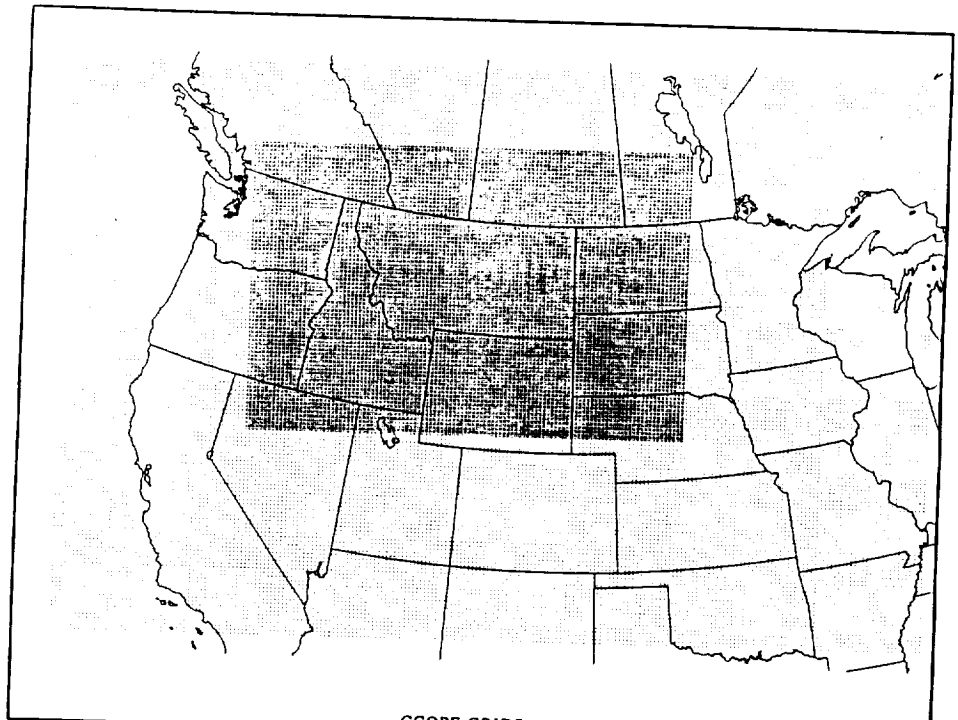

CCOPE GRIDS

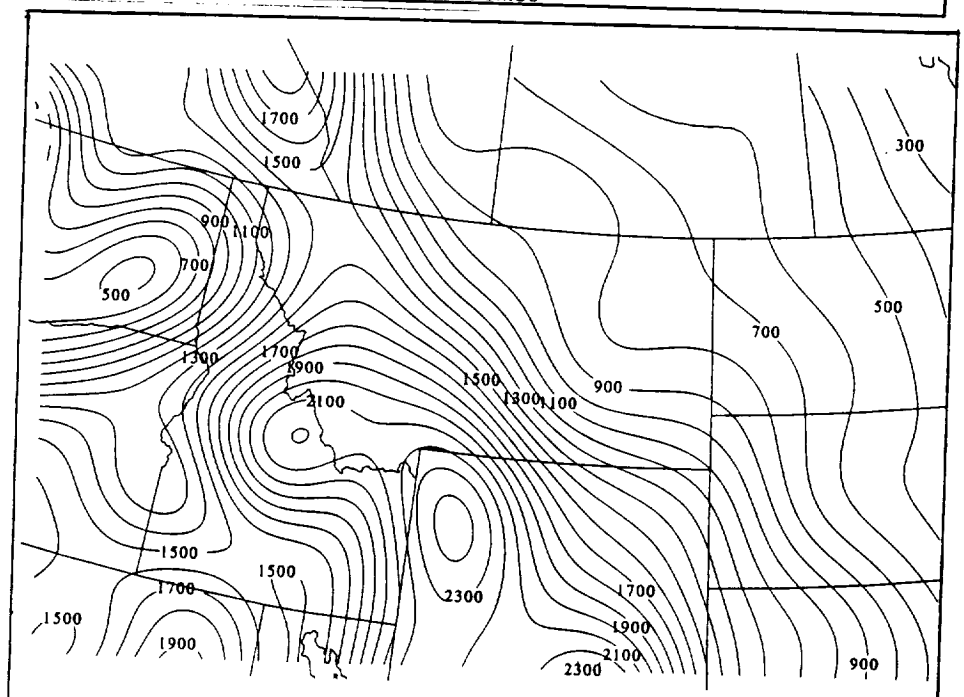

SMOOTH TERRAIN

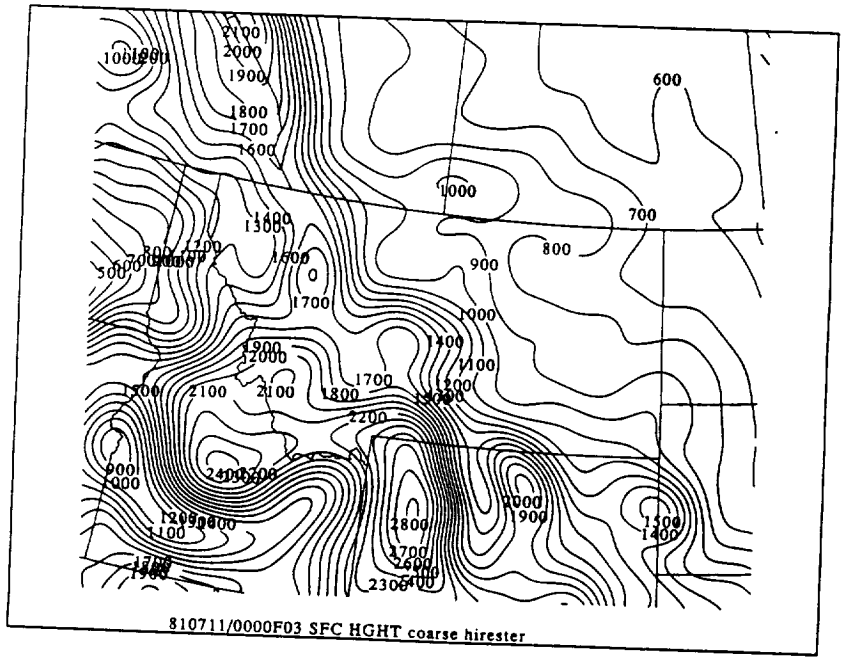
810711/0000F03 SFC HGHT coarse hirester

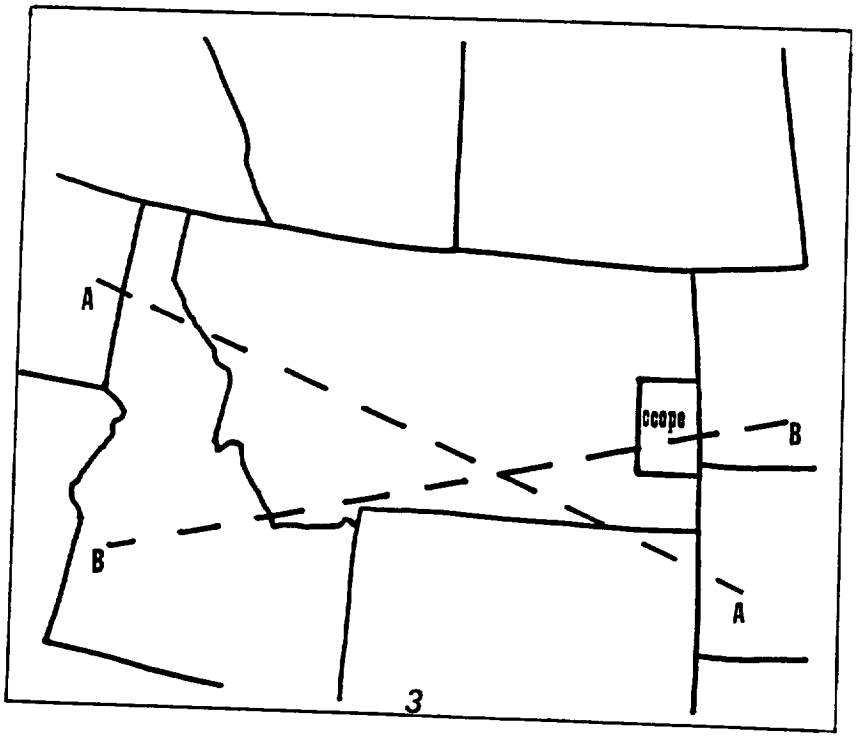

3

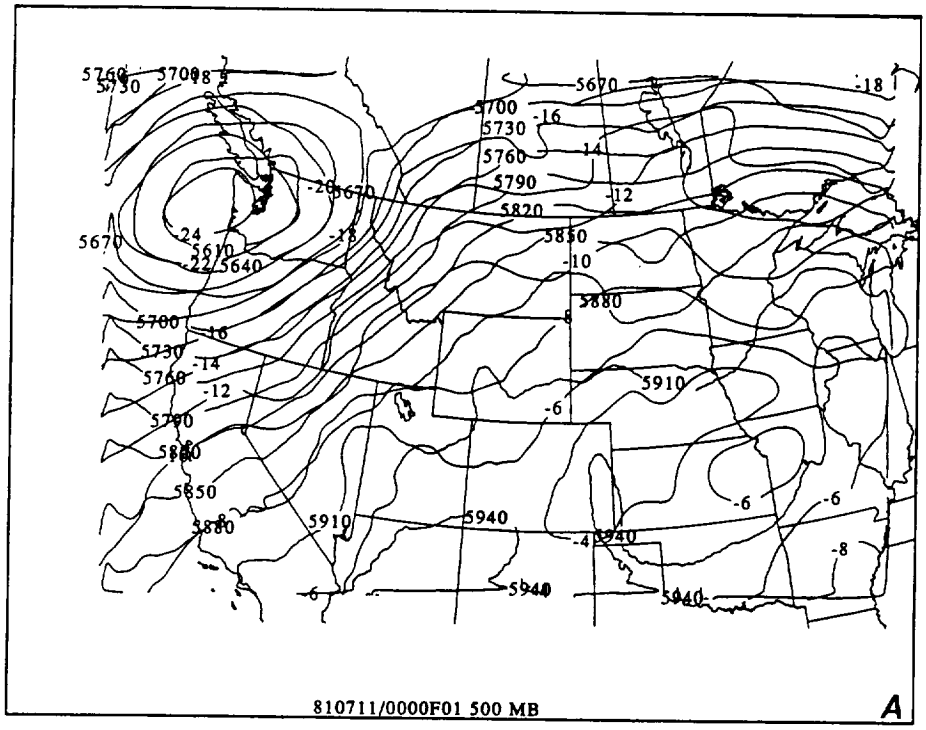
810711/0000F01 500 MB
A

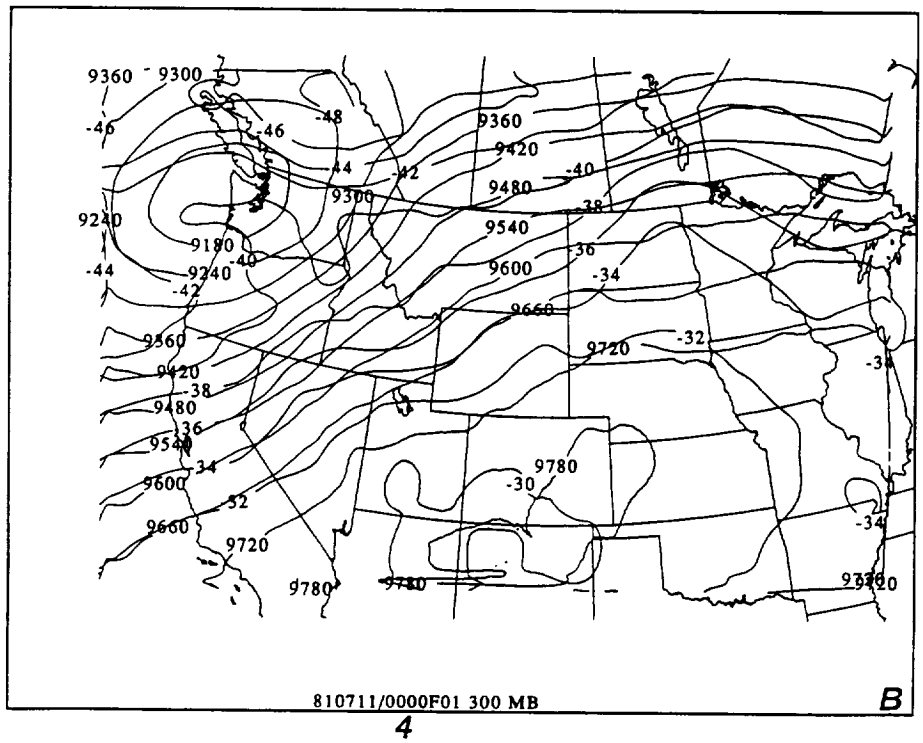
810711/0000F01 300 MB
B

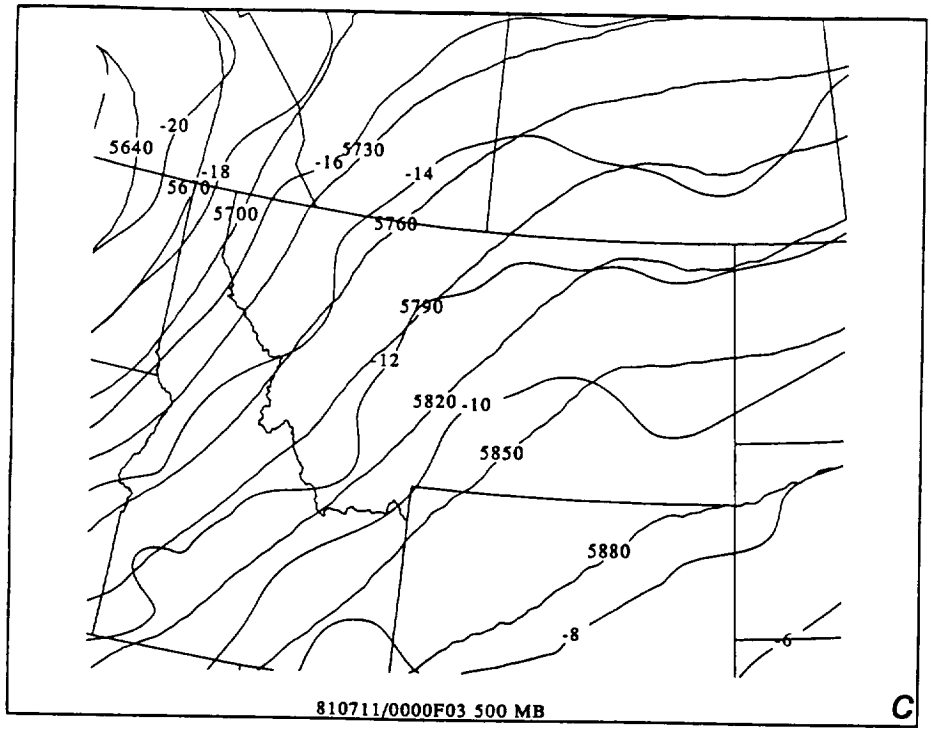
-20
5640
-18
5670
5700
-16
5730
-14
5760
5790
-12
5820
-10
5850
5880
-8
-6
810711/0000F03 500 MB
C

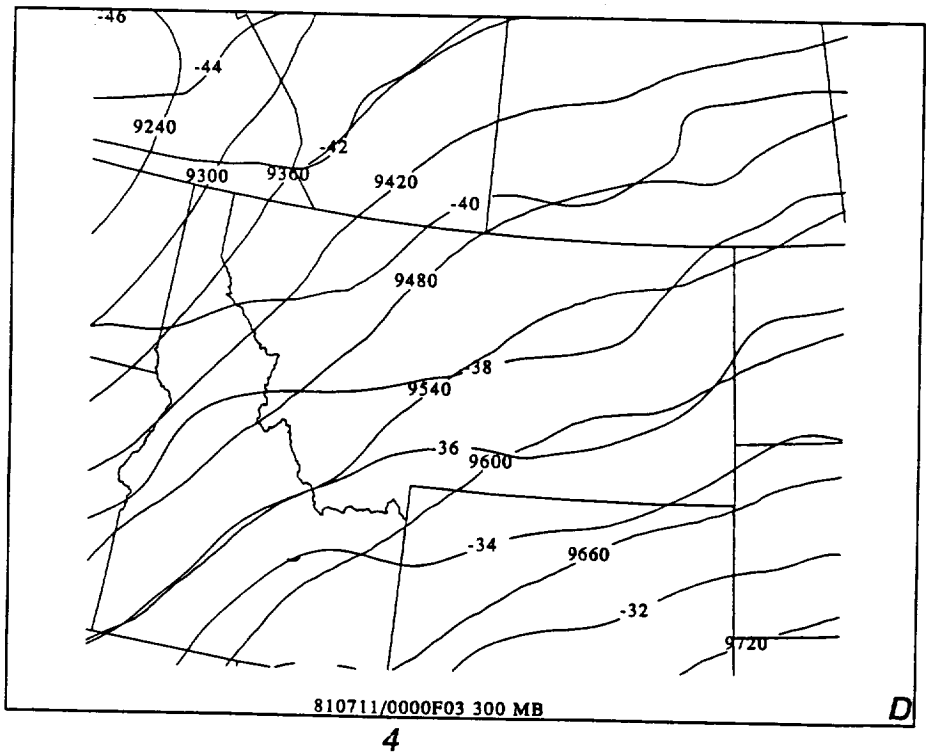
-46
-44
9240
-42
9300
9360
9420
-40
9480
-38
9540
-36
9600
-34
9660
-32
9720
810711/0000F03 300 MB
D

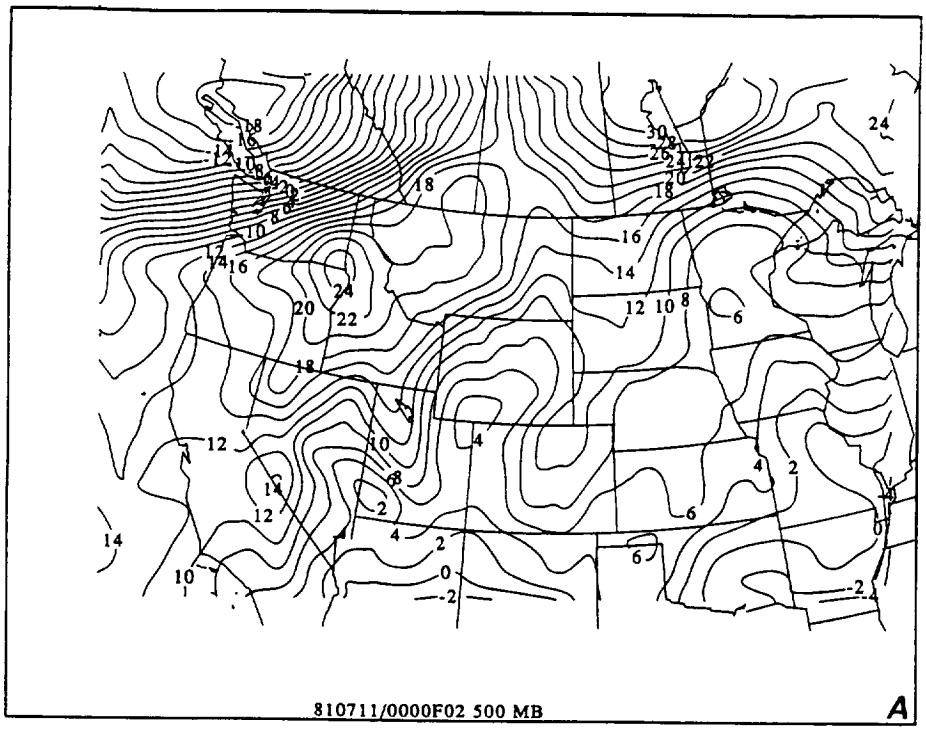
810711/0000F02 500 MB
A

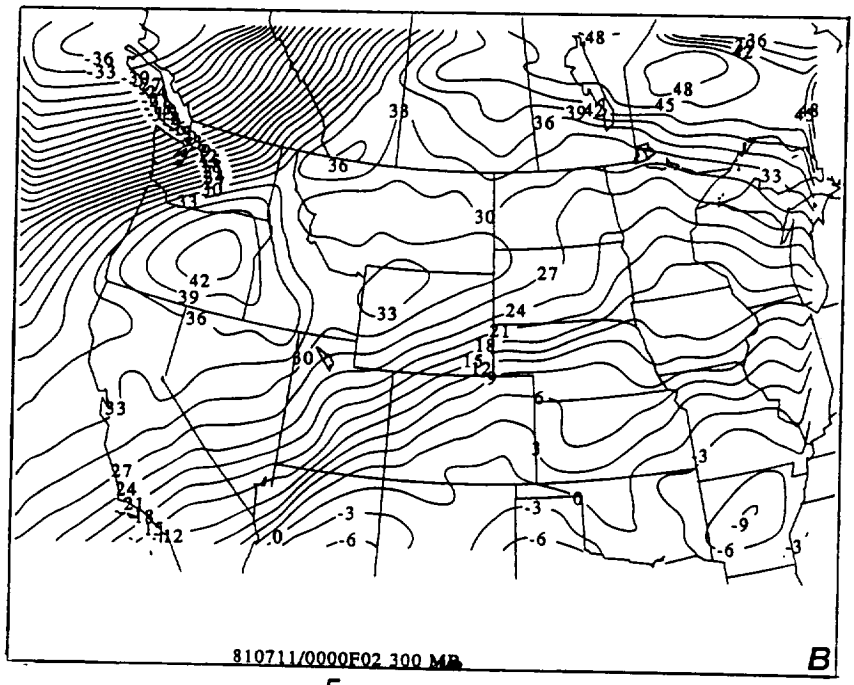
810711/0000F02 300 MB
B

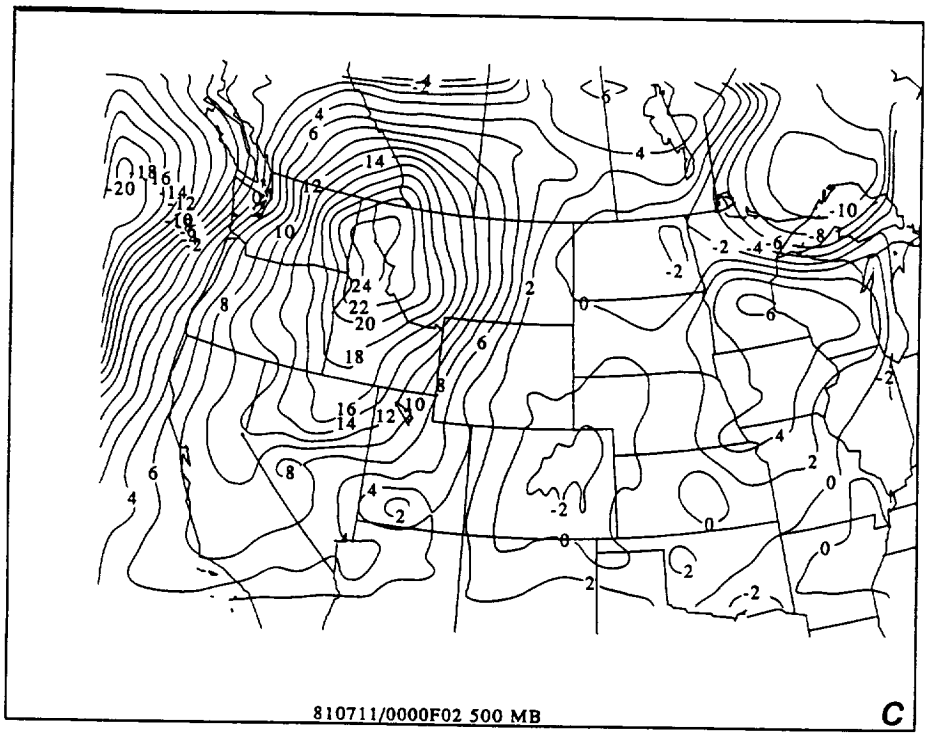
810711/0000F02 500 MB
C

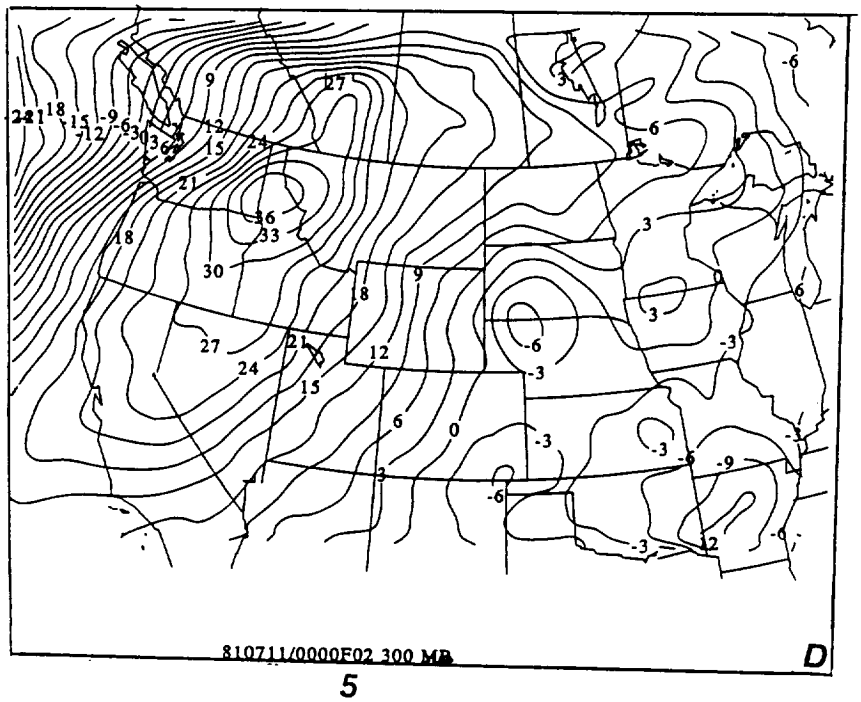
810711/0000F02 300 MB
D

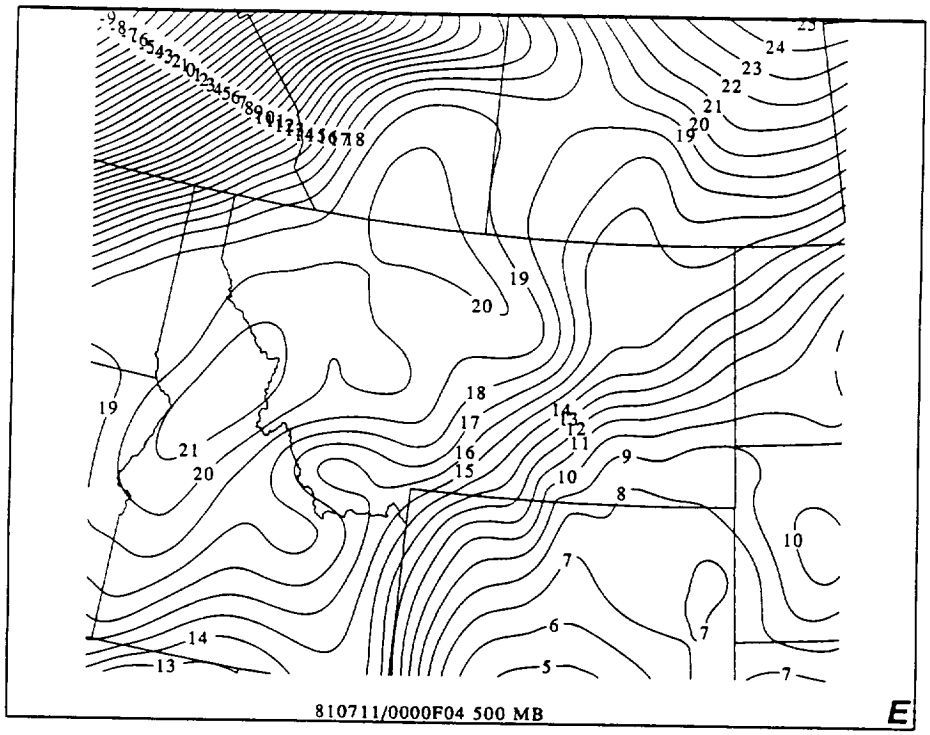
810711/0000F04 500 MB
E

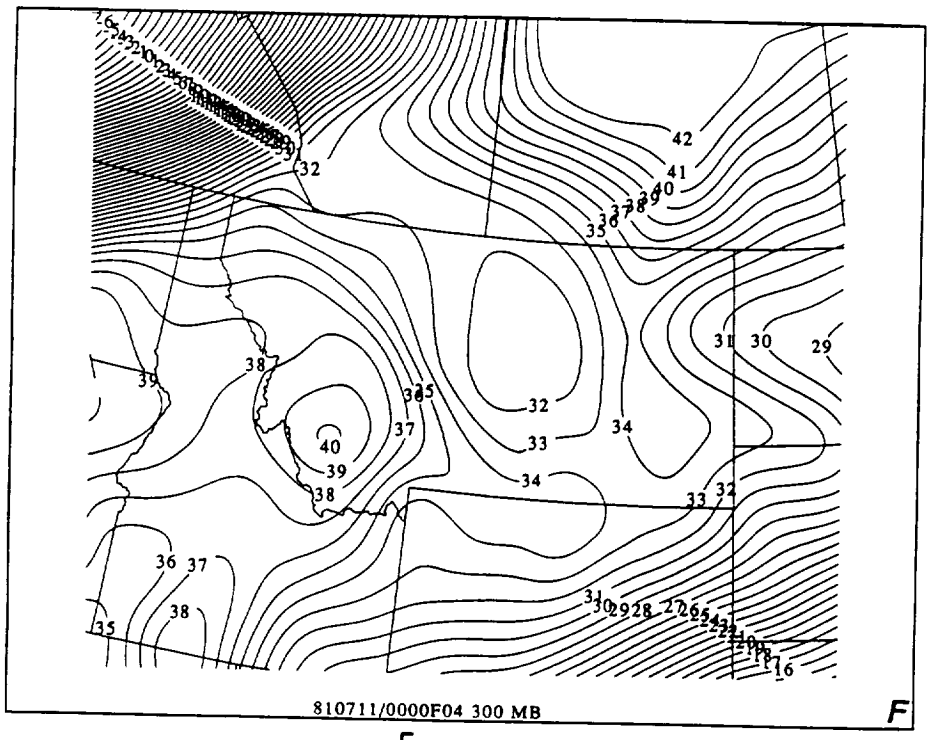
810711/0000F04 300 MB
F

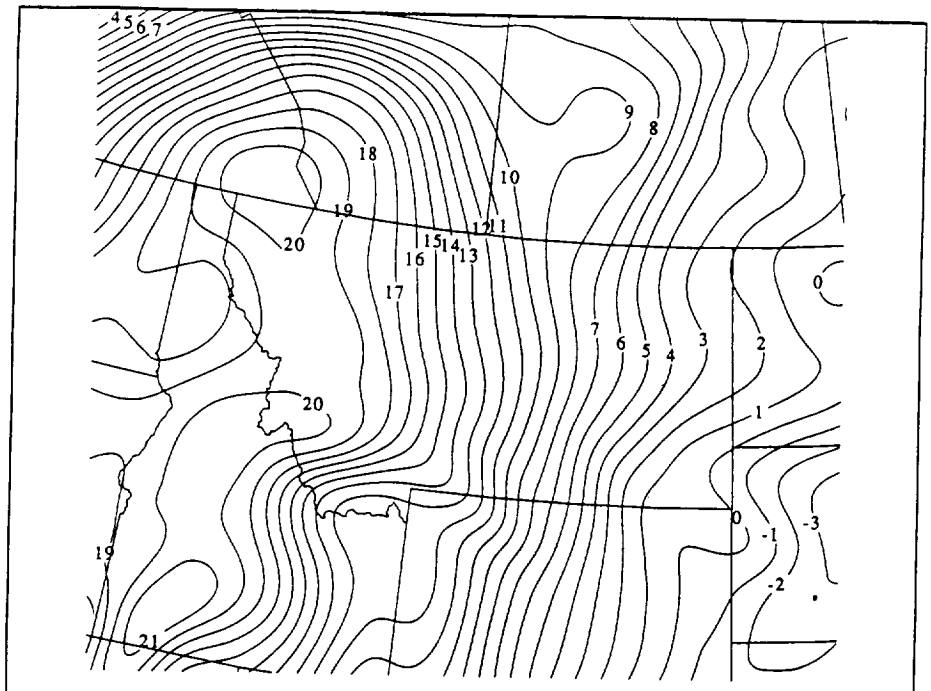

810711/0000F04 500 MB

G

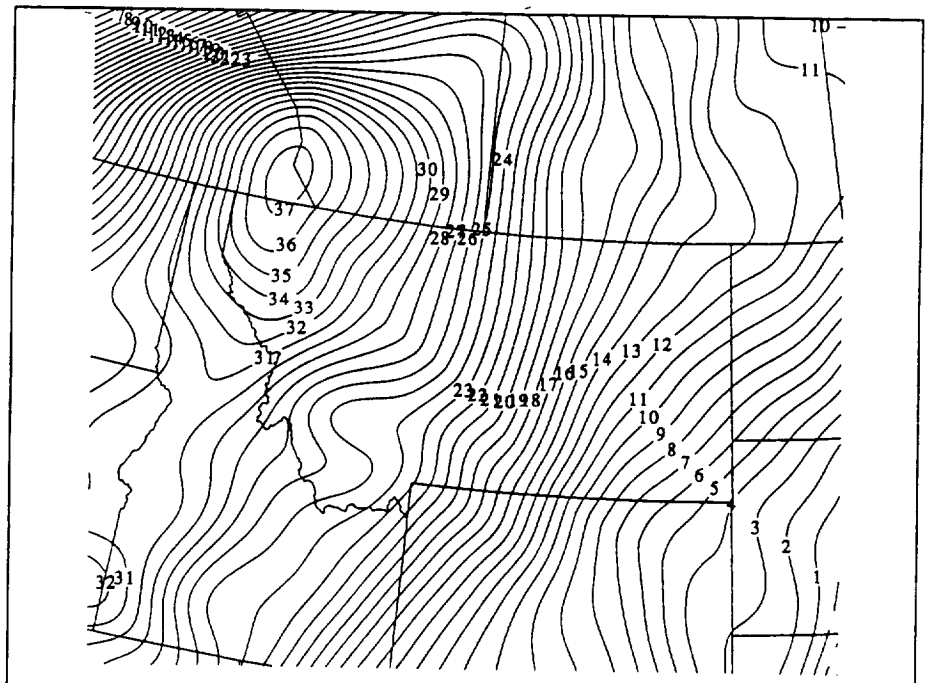

810711/0000F04 300 MB

H

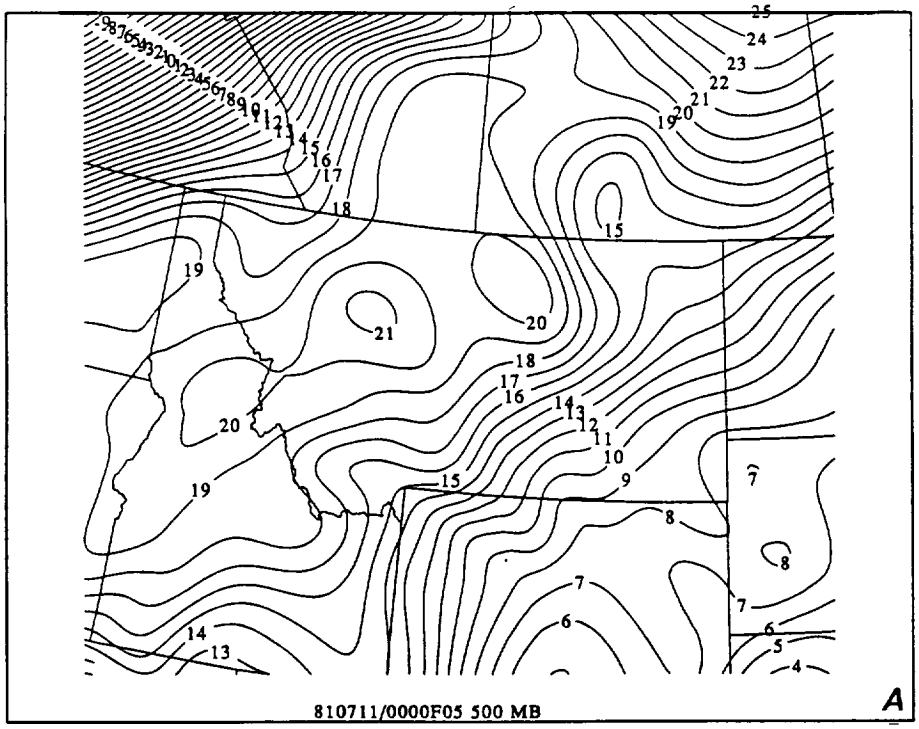
810711/0000F05 500 MB
A

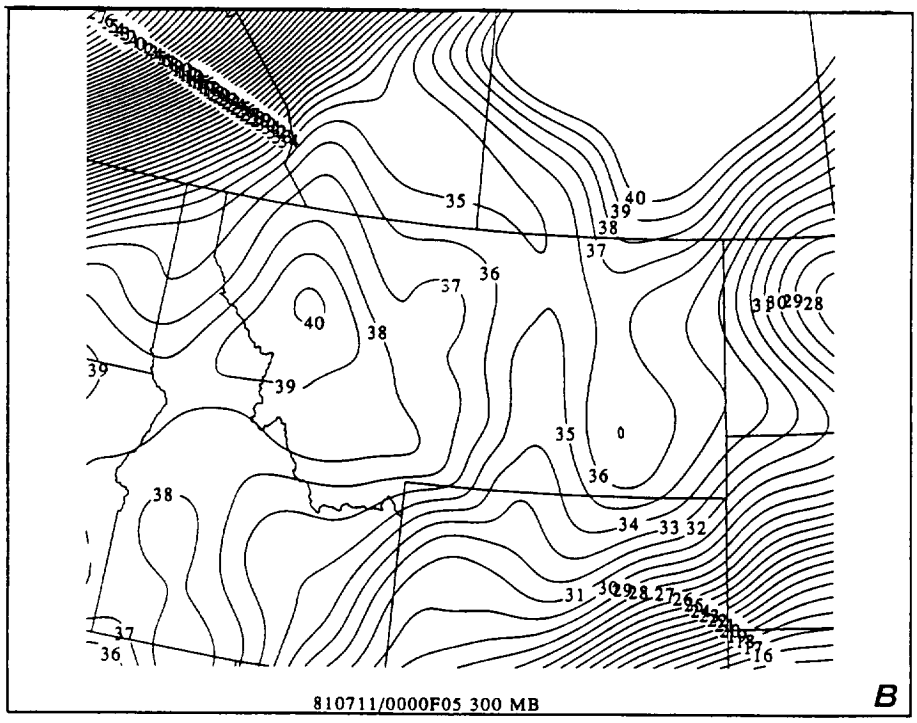
810711/0000F05 300 MB
B

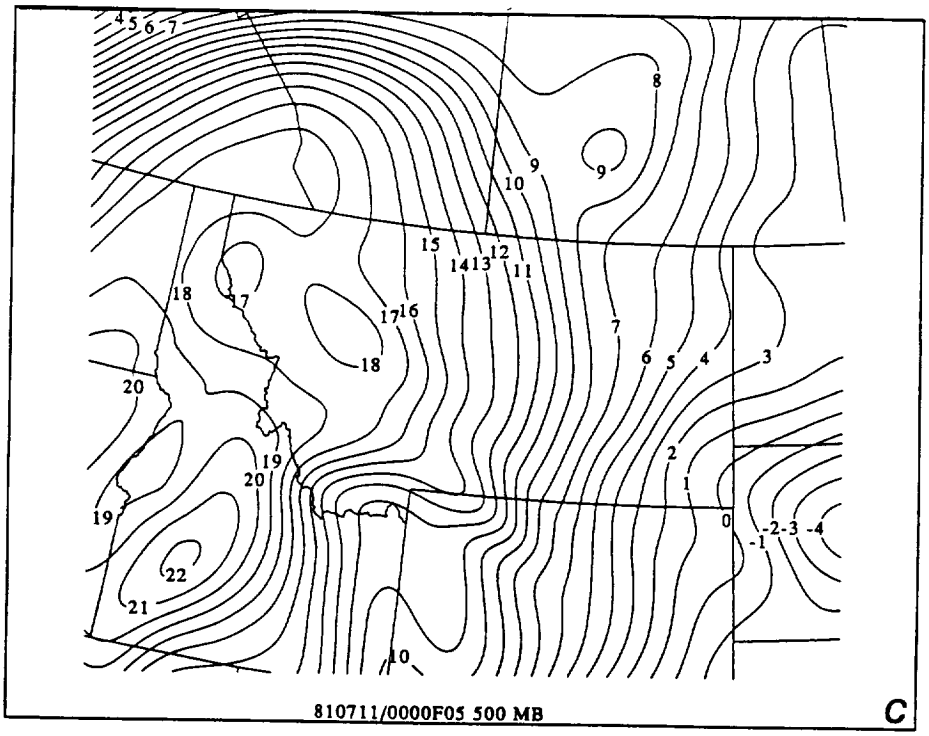
810711/0000F05 500 MB
C

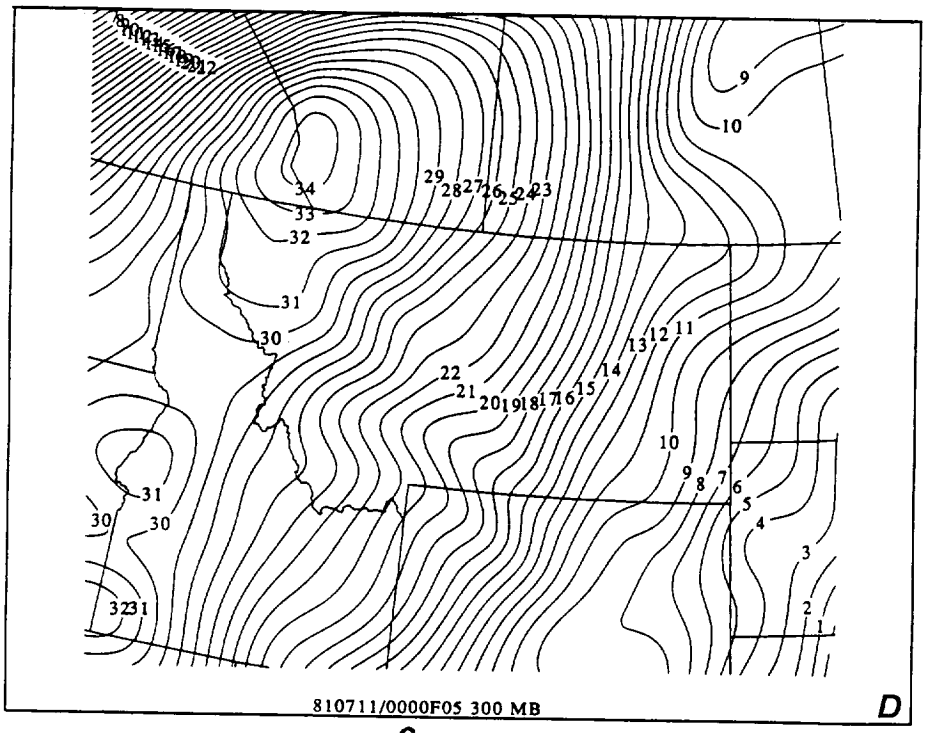
810711/0000F05 300 MB
D

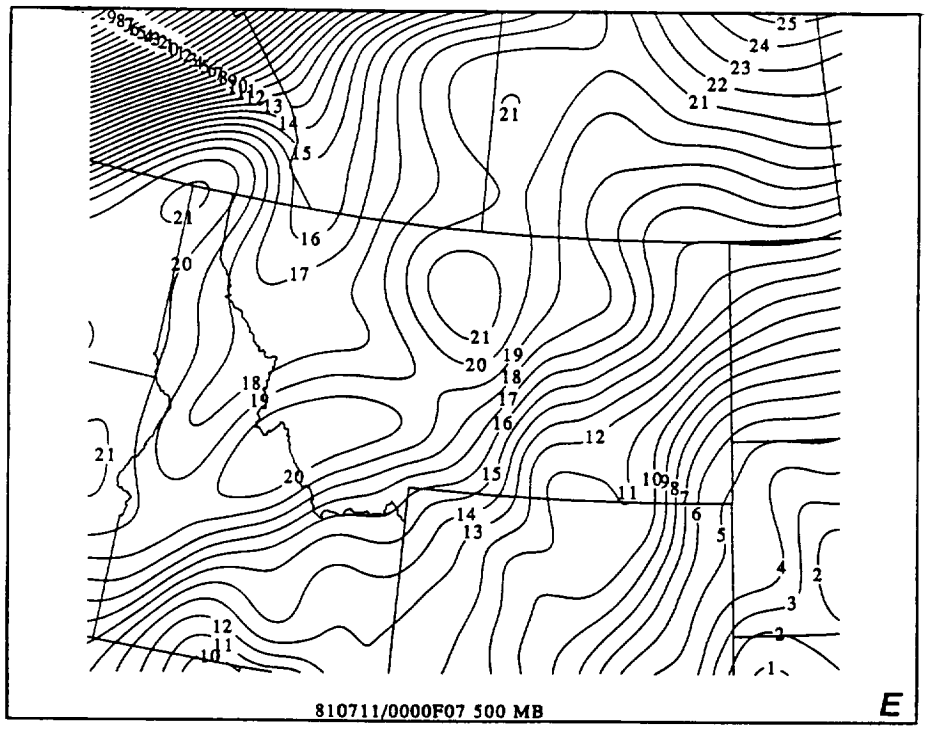
810711/0000F07 500 MB
E

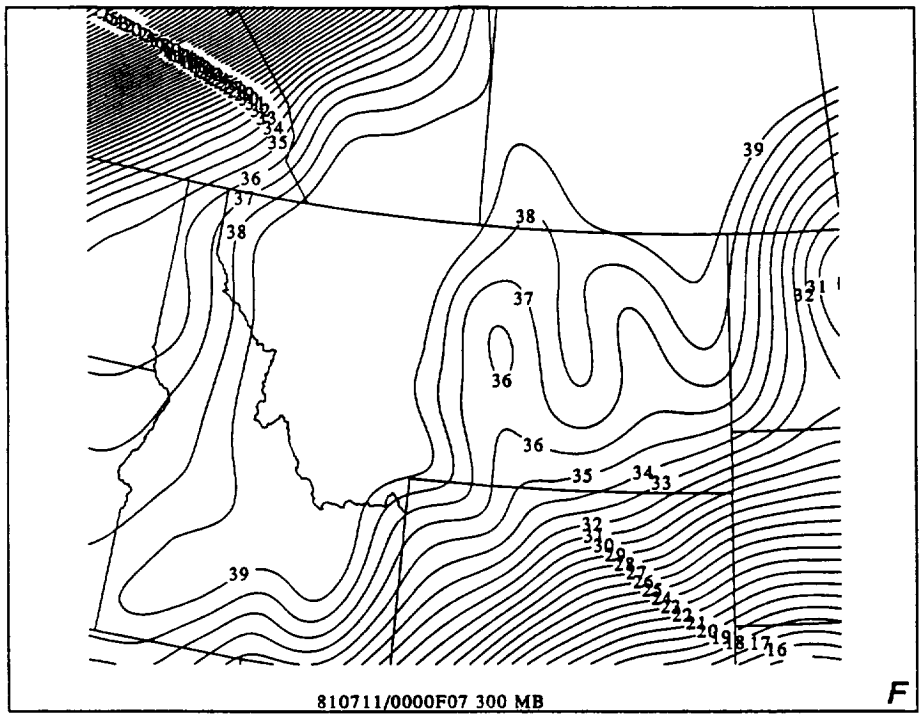
810711/0000F07 300 MB
F

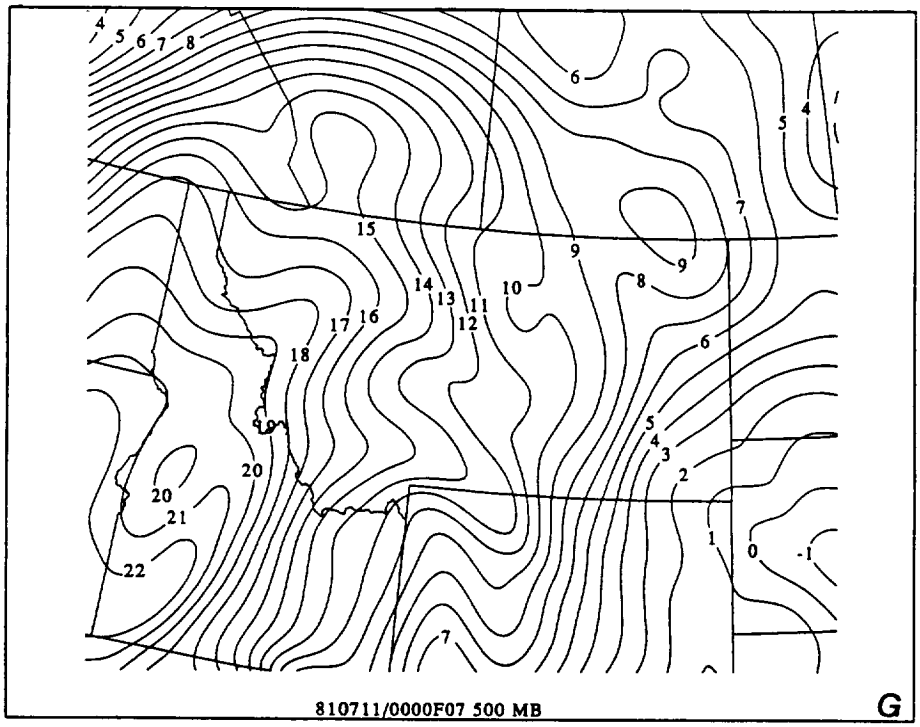
810711/0000F07 500 MB
G

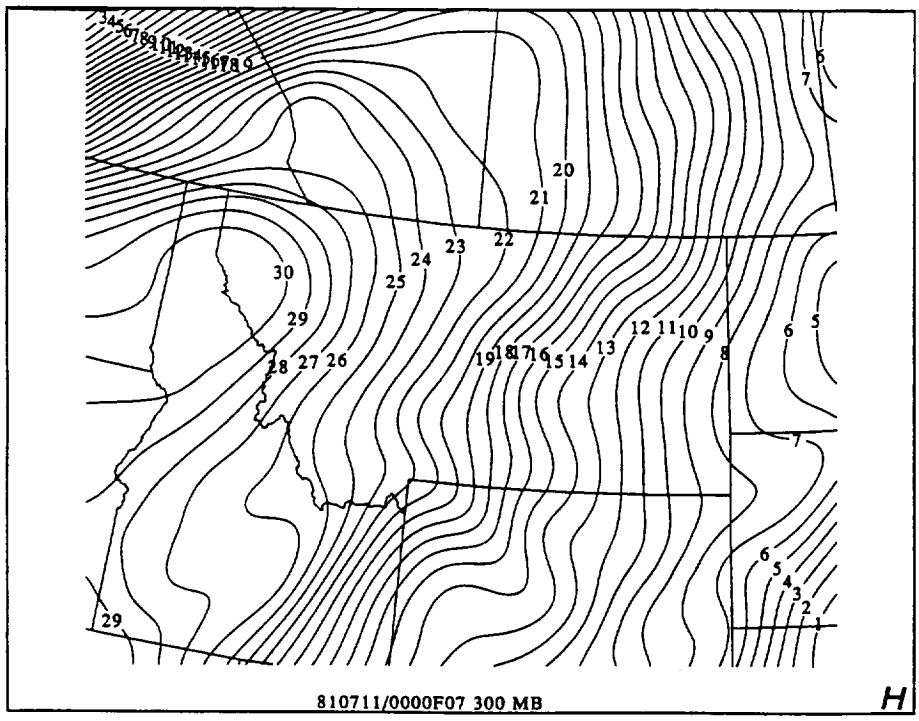
810711/0000F07 300 MB
H

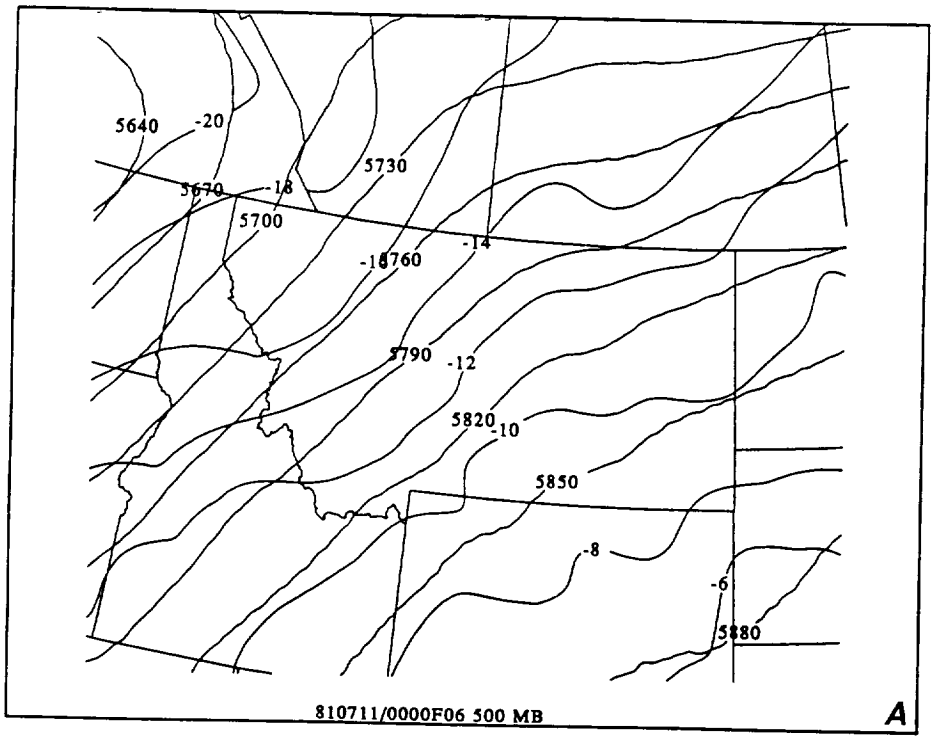
5640
-20
5730
5670
-18
5700
-14
-16
5760
5790
-12
5820
-10
5850
-8
-6
5880
810711/0000F06 500 MB
A

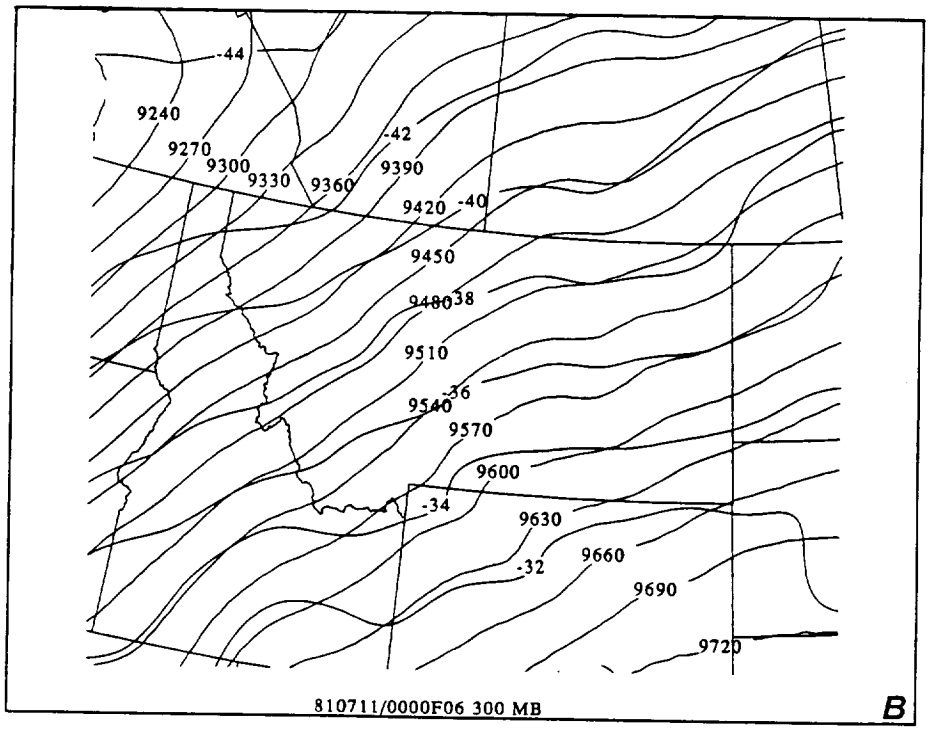
-44
9240
9270
9300
9330
9360
-42
9390
9420
-40
9450
9480
38
9510
9540
-36
9570
9600
-34
9630
9660
-32
9690
9720
810711/0000F06 300 MB
B

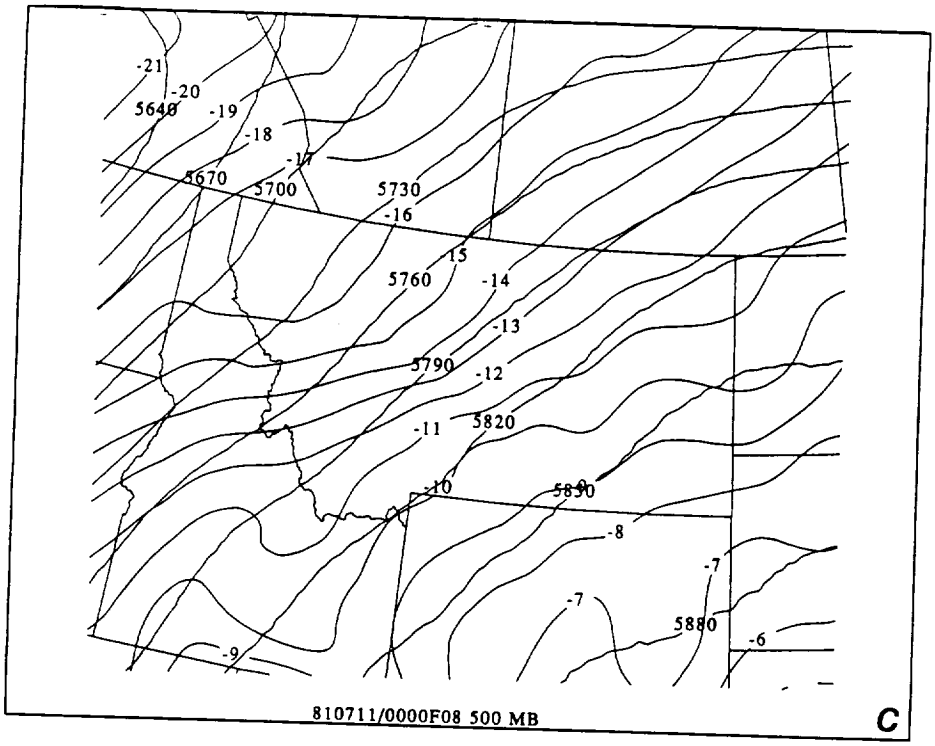
-21
-20
5640
-19
-18
-17
5670
5700
5730
-16
-15
5760
-14
-13
5790
-12
-11
5820
-10
5850
-8
-7
-7
5880
-6
-9
810711/0000F08 500 MB
C

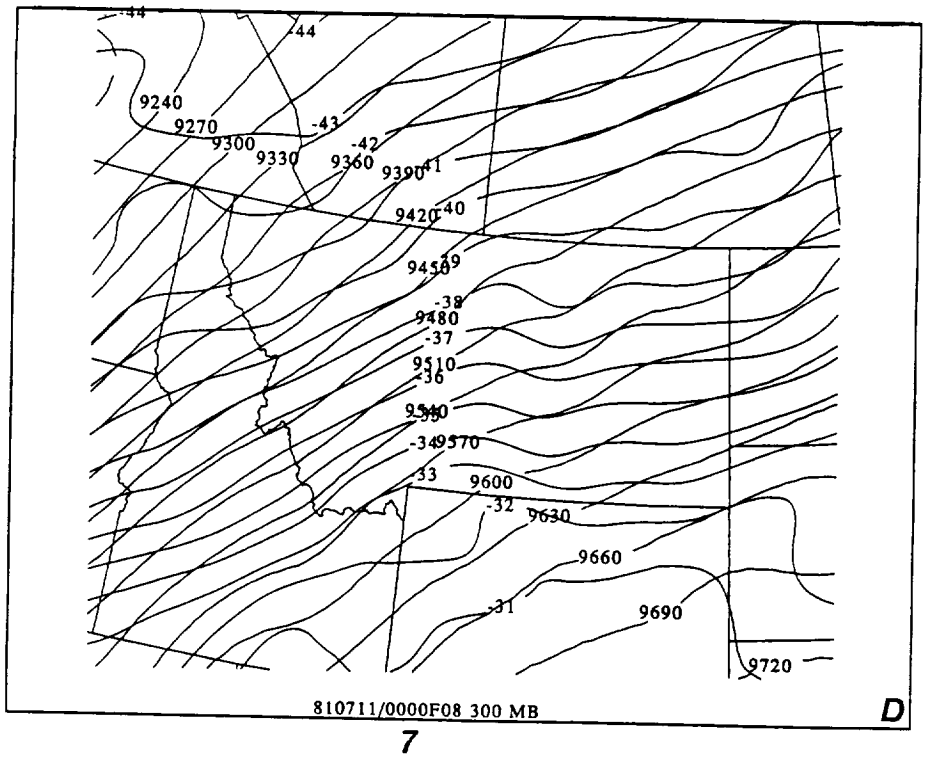
-44
-44
9240
9270
-43
9300
-42
9330
9360
9390
-41
9420
-40
9450
-39
-38
9480
-37
9510
-36
9540
-35
-34
9570
-33
9600
-32
9630
9660
-31
9690
9720
810711/0000F08 300 MB
D

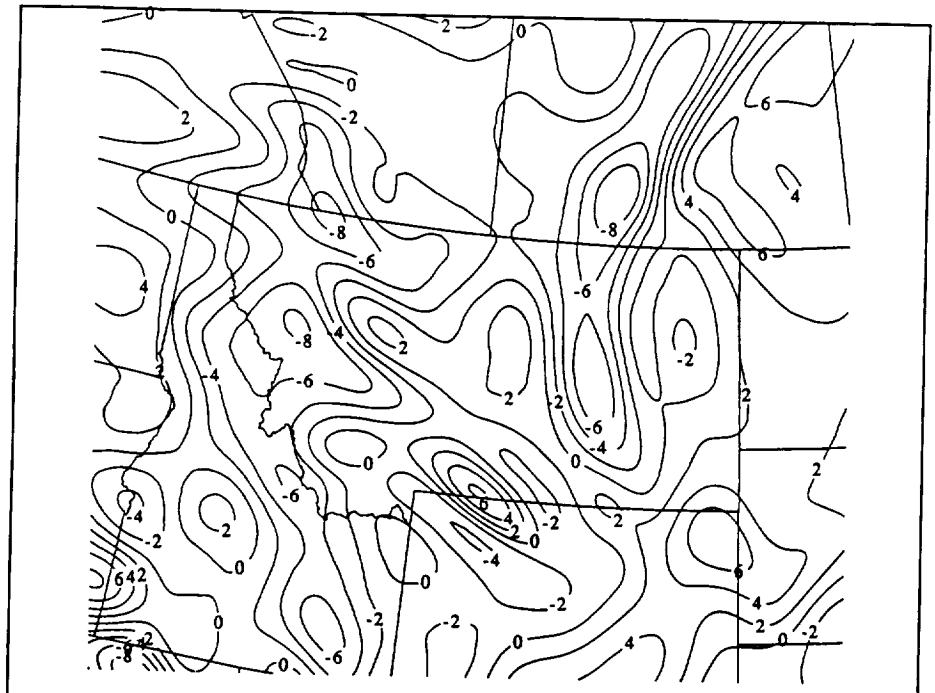

810711/0000F05 500 MB

E

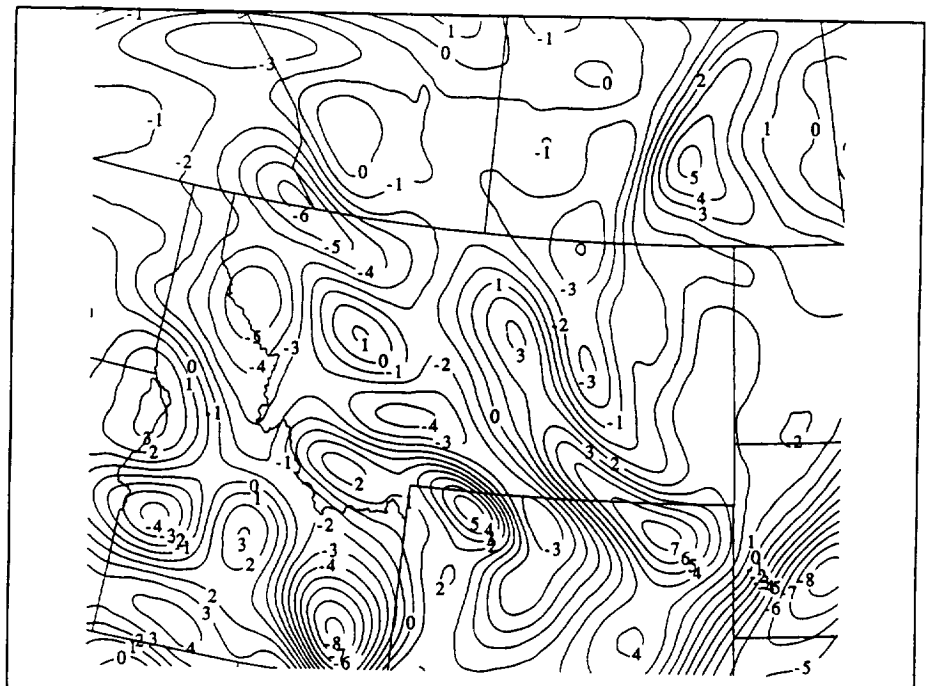

810711/0000F05 300 MB

F

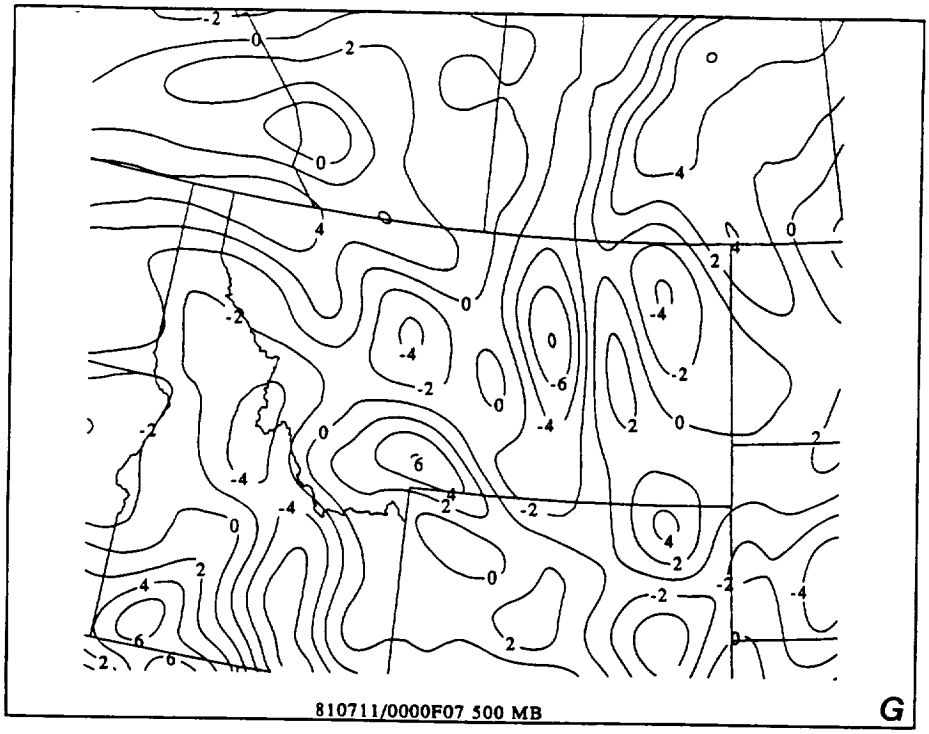
810711/0000F07 500 MB
G

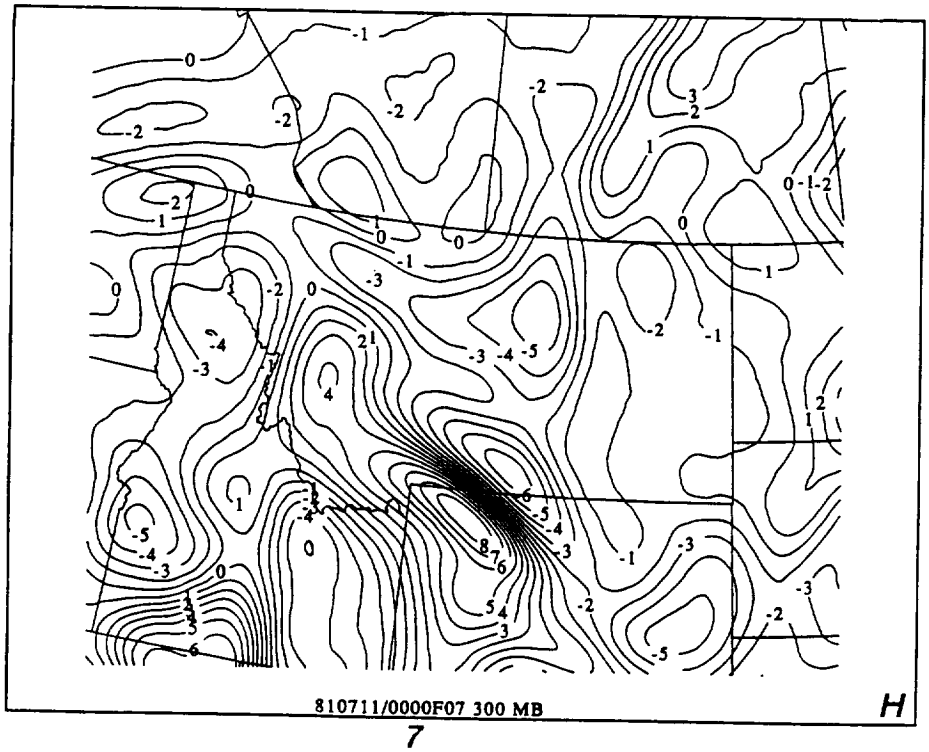
810711/0000F07 300 MB
H

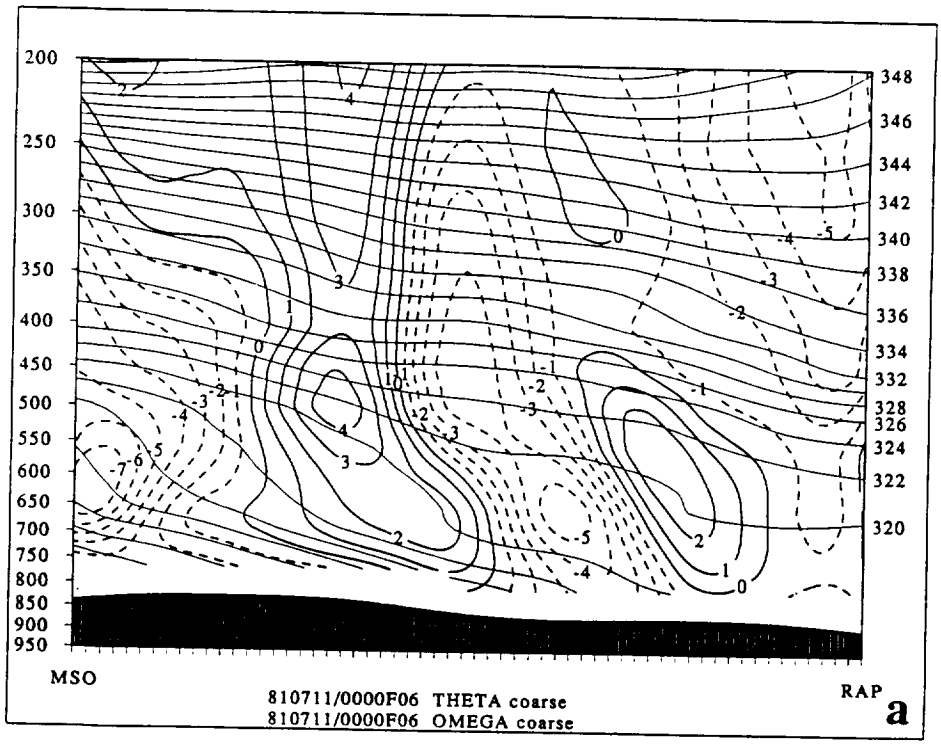
MSO
RAP
810711/0000F06 THETA coarse
810711/0000F06 OMEGA coarse
a

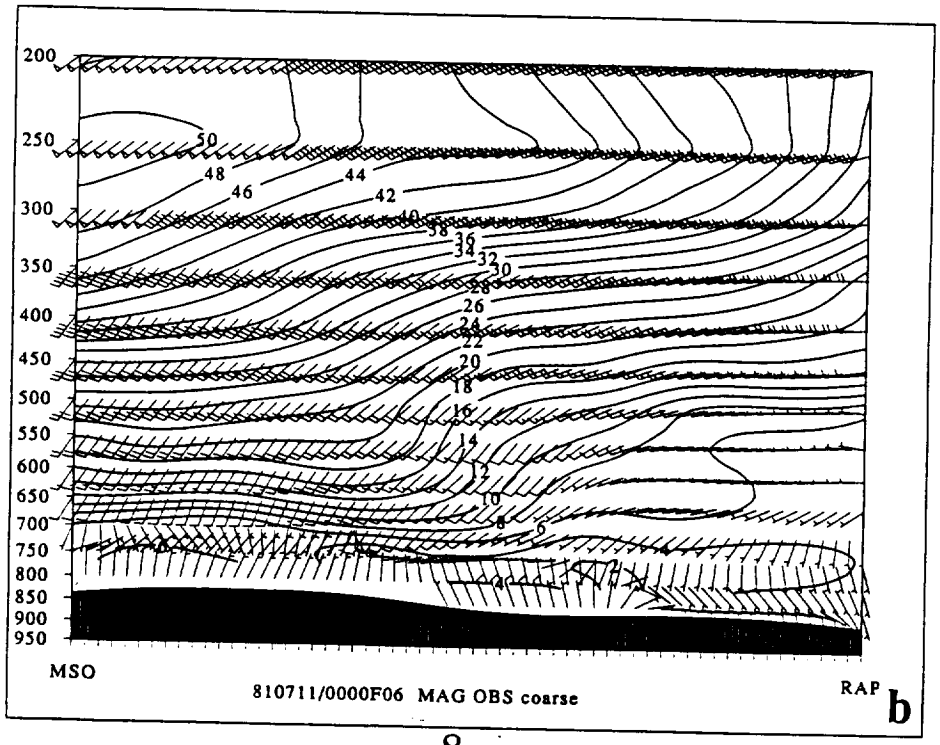
MSO
RAP
810711/0000F06 MAG OBS coarse
b

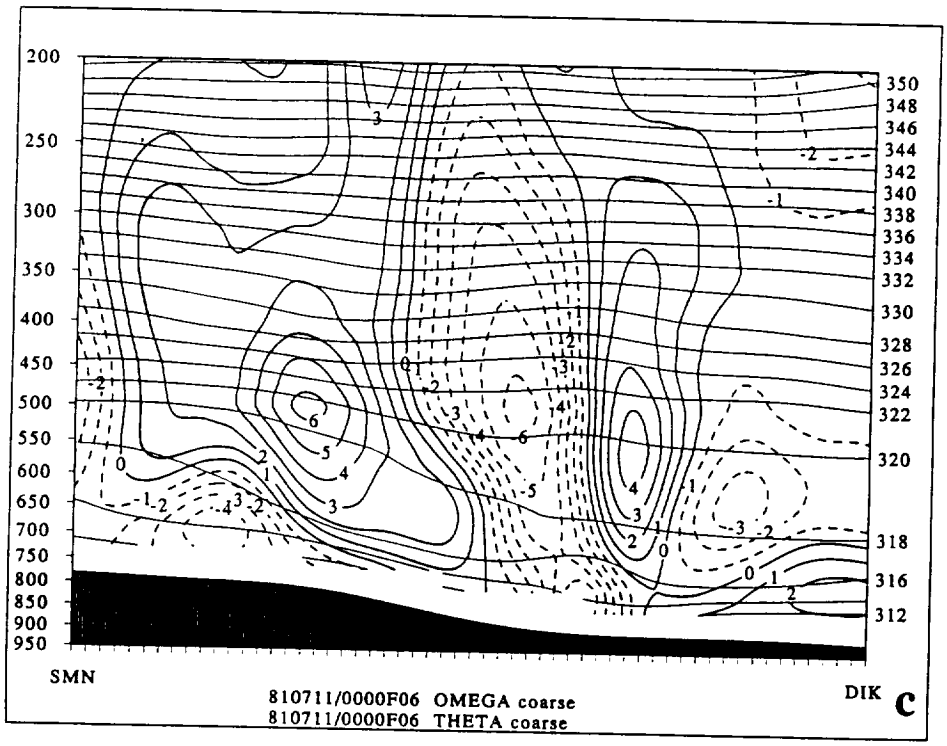
SMN
DIK
810711/0000F06 OMEGA coarse
810711/0000F06 THETA coarse
c

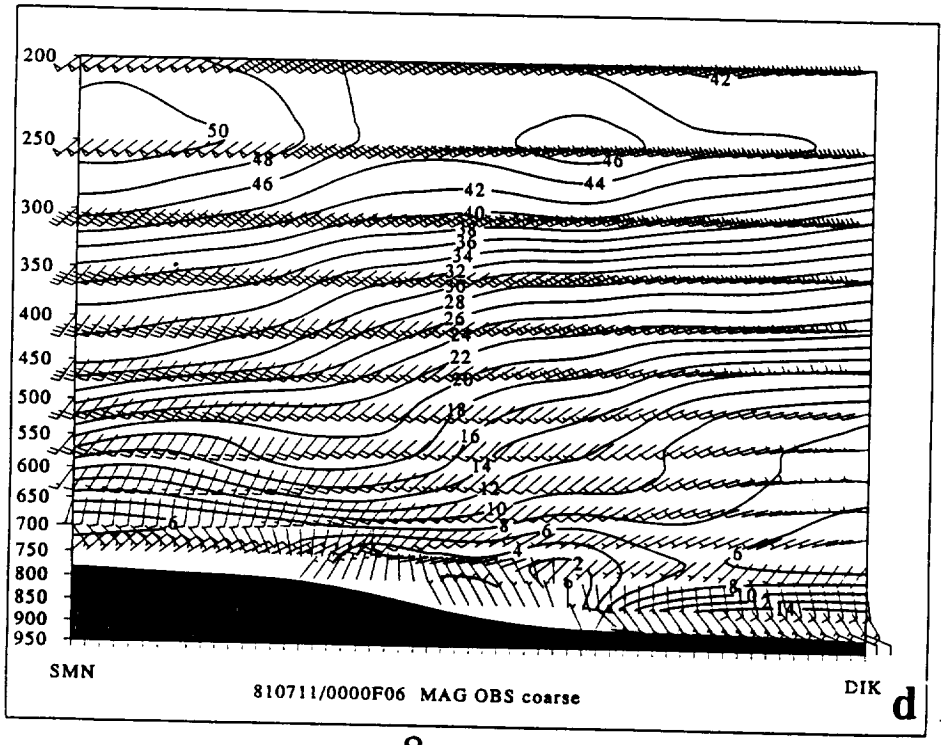
SMN
DIK
810711/0000F06 MAG OBS coarse
d

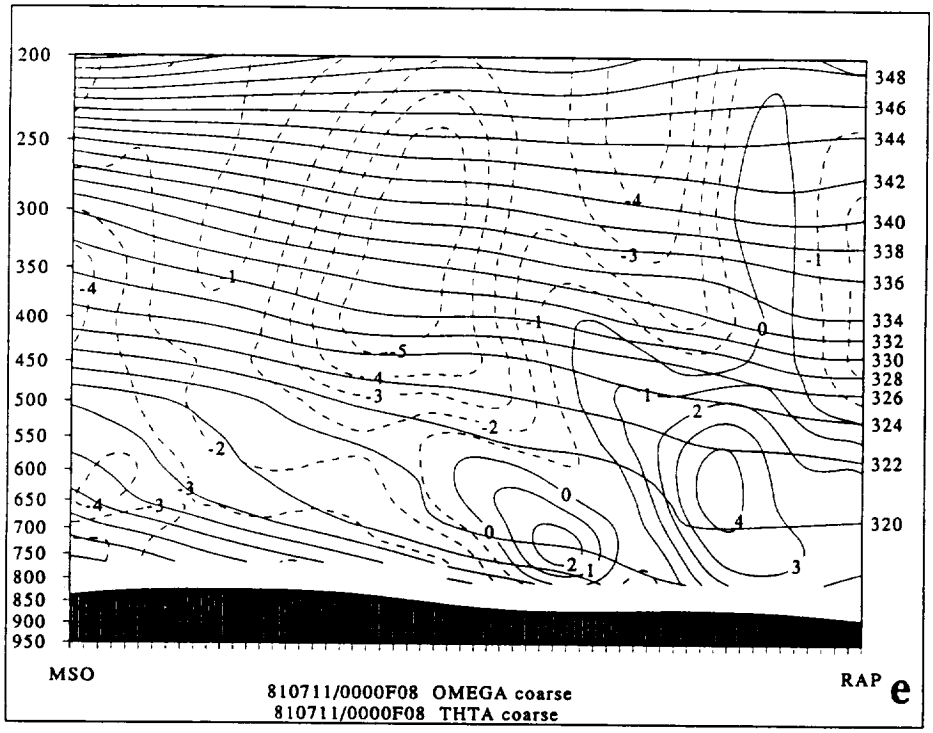
200
250
300
350
400
450
500
550
600
650
700
750
800
850
900
950
348
346
344
342
340
338
336
334
332
330
328
326
324
322
320
MSO
RAP
e
810711/0000F08 OMEGA coarse
810711/0000F08 THTA coarse

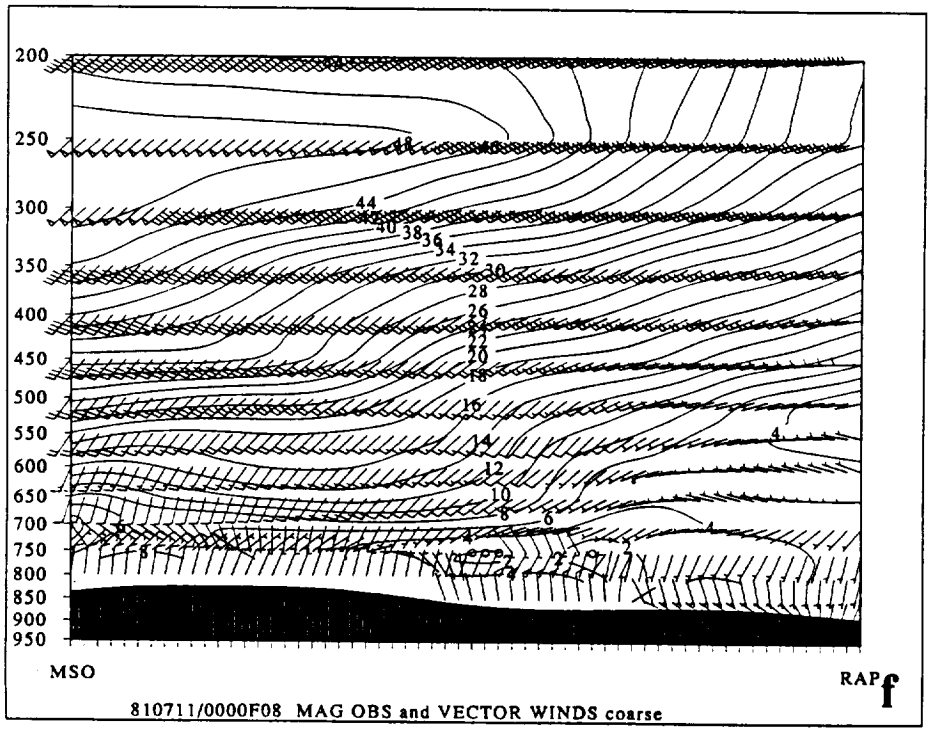
200
250
300
350
400
450
500
550
600
650
700
750
800
850
900
950
MSO
RAP
f
810711/0000F08 MAG OBS and VECTOR WINDS coarse

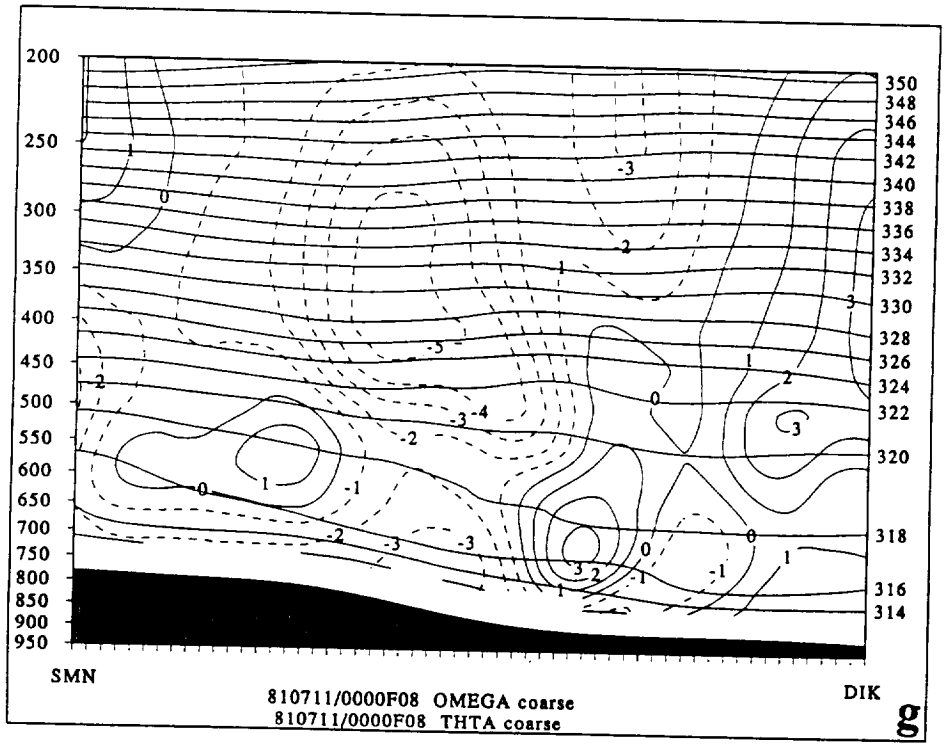
SMN
DIK
810711/0000F08 OMEGA coarse
810711/0000F08 THTA coarse
g

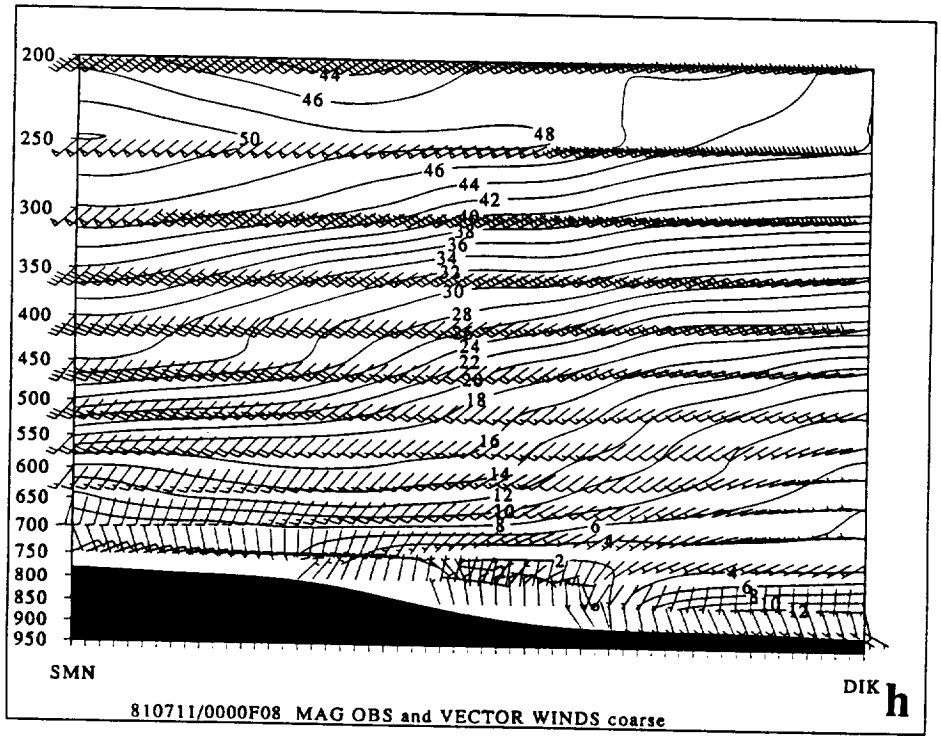
SMN
DIK
810711/0000F08 MAG OBS and VECTOR WINDS coarse
h

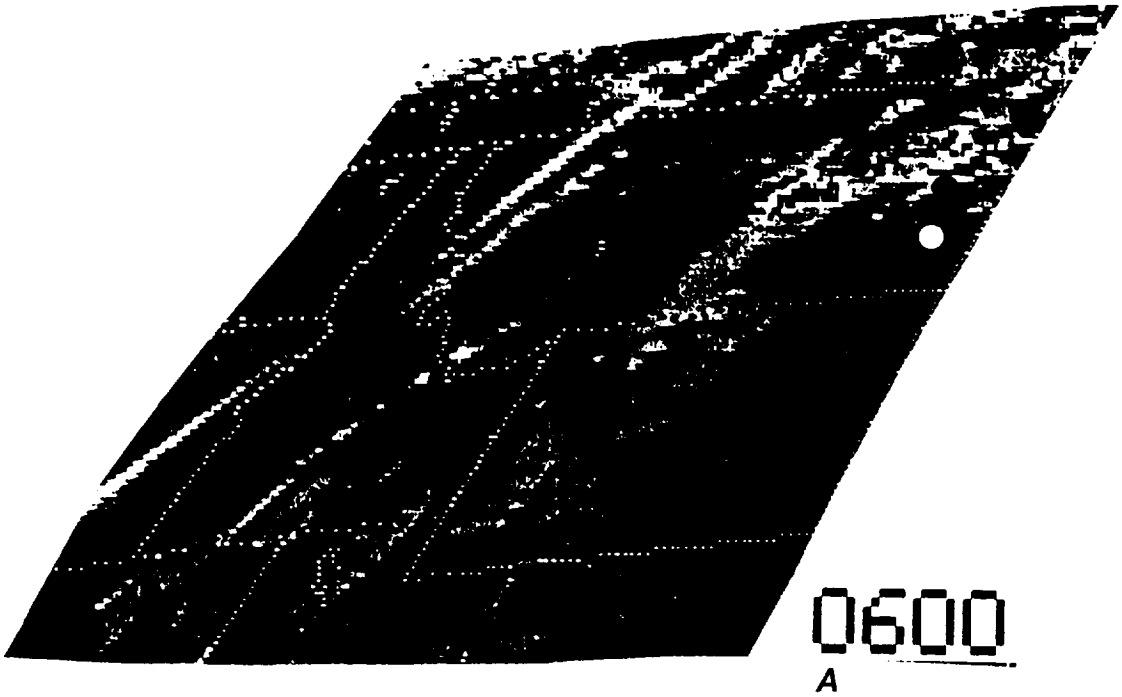

A

B

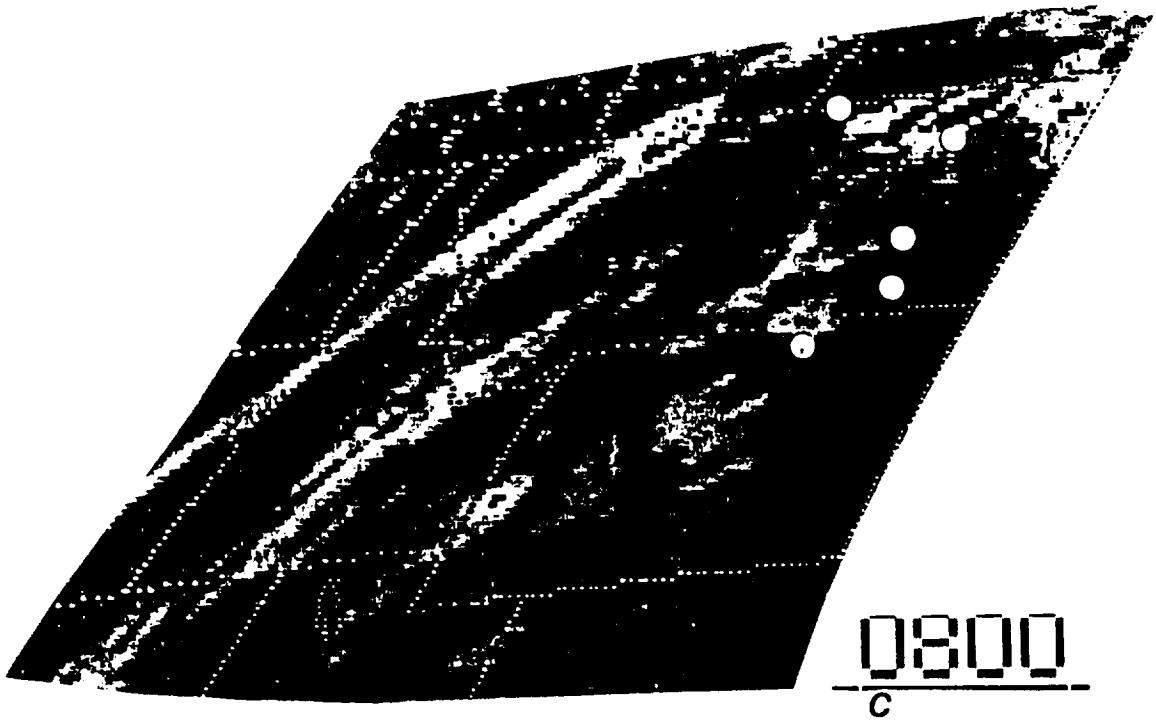

C

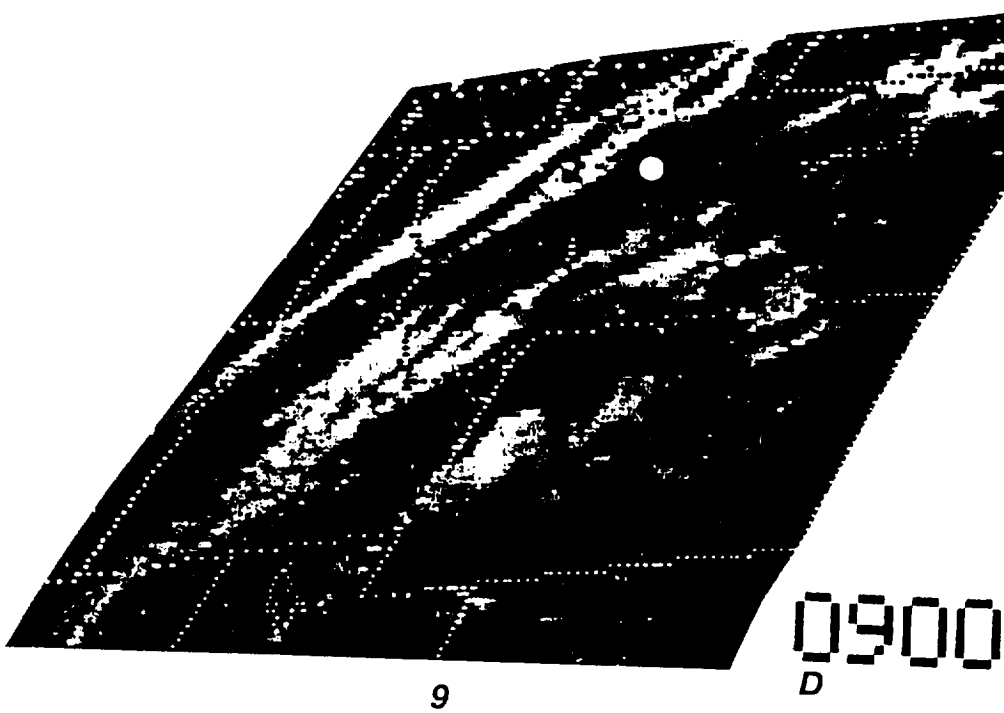

D

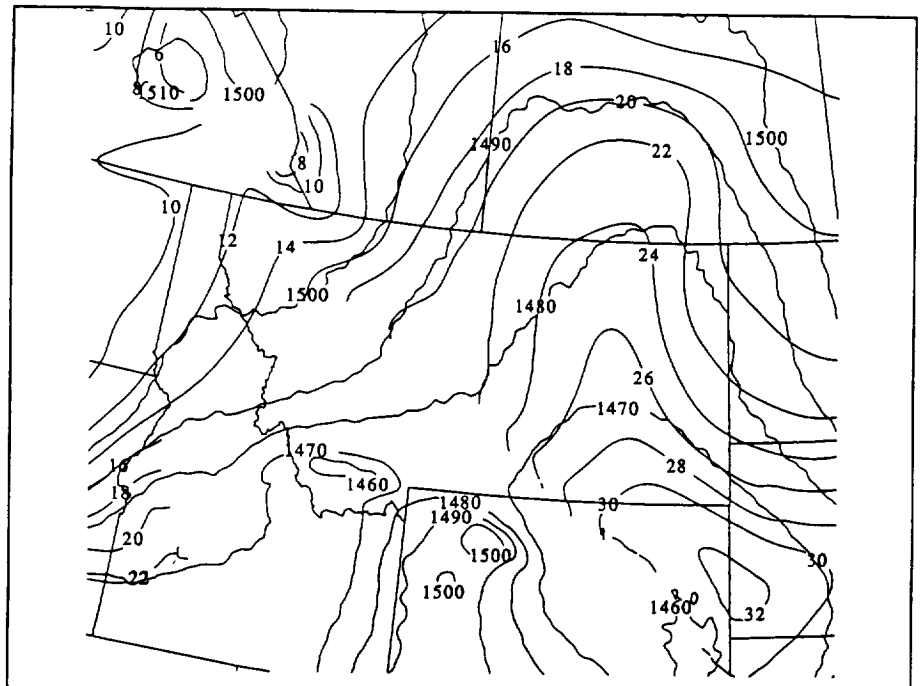

810711/0000F03 850 MB

A

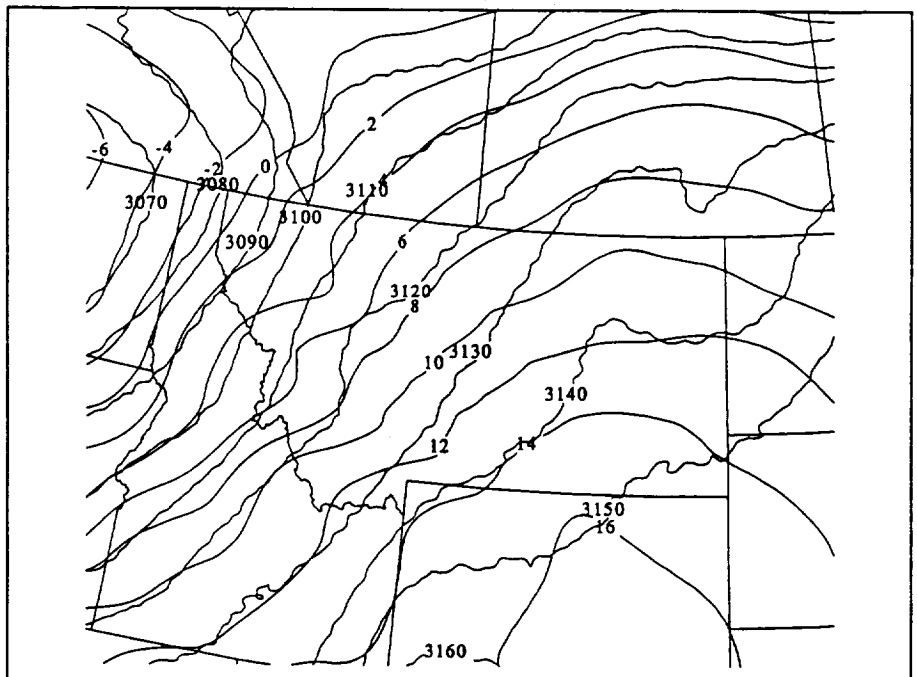

810711/0000F03 700 MB

B

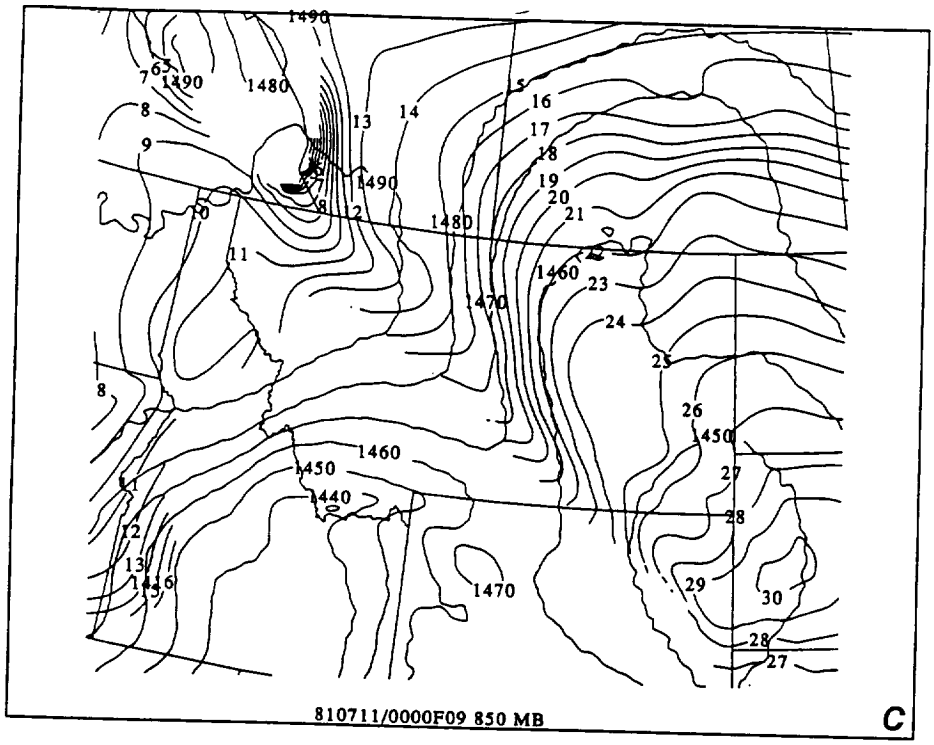
1490
1480
1460
1450
1440
1470
810711/0000F09 850 MB
C

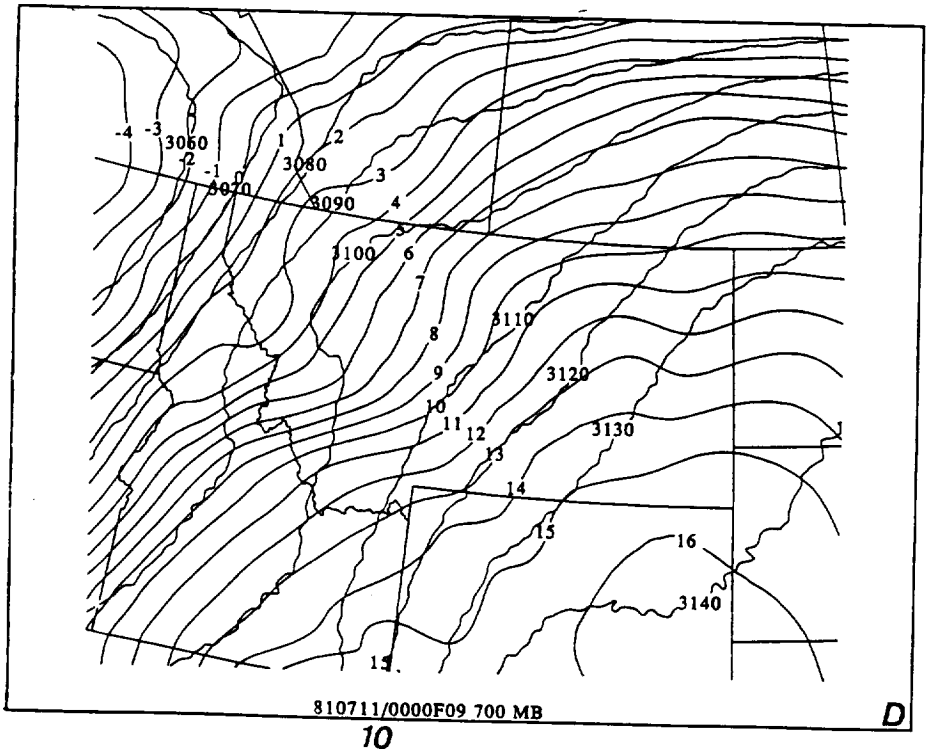
3060
3080
3090
3100
3110
3120
3130
3140
810711/0000F09 700 MB
D

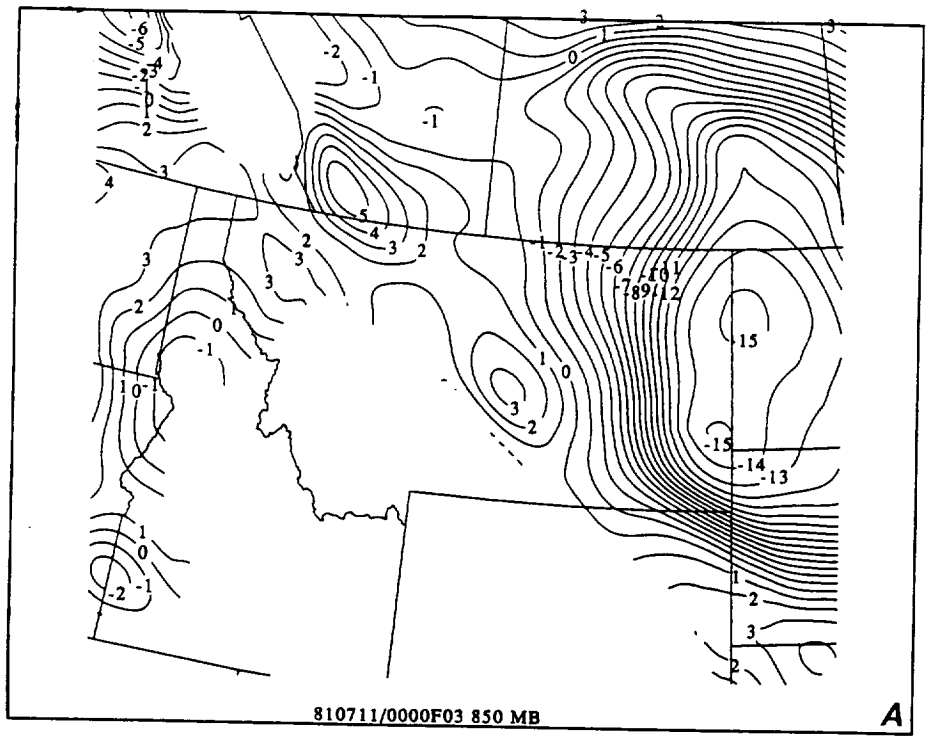
810711/0000F03 850 MB
A

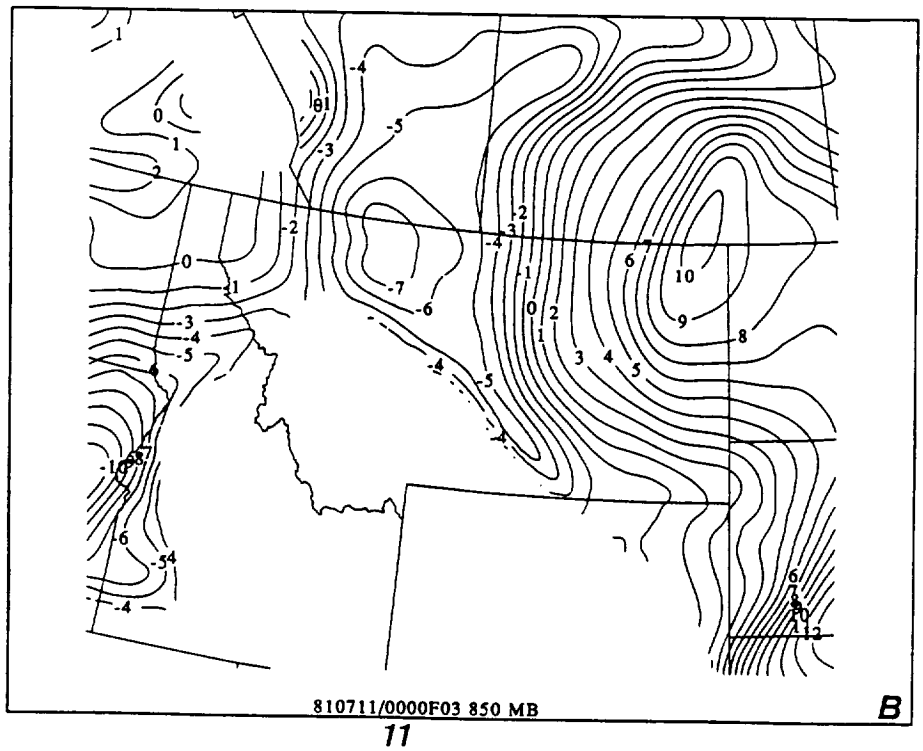
810711/0000F03 850 MB
B

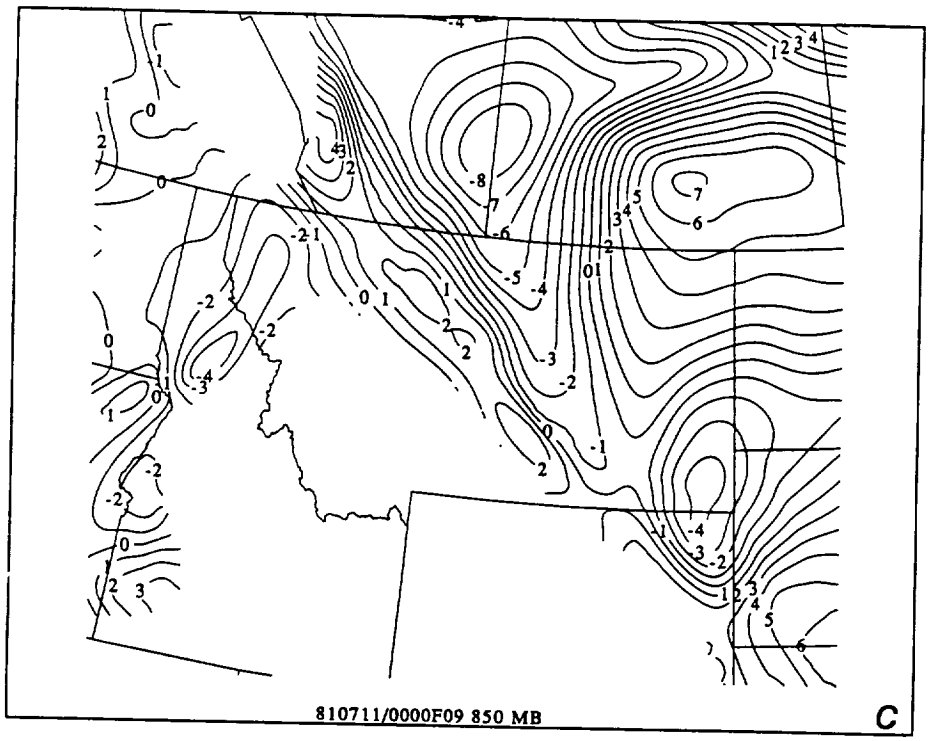
810711/0000F09 850 MB
C

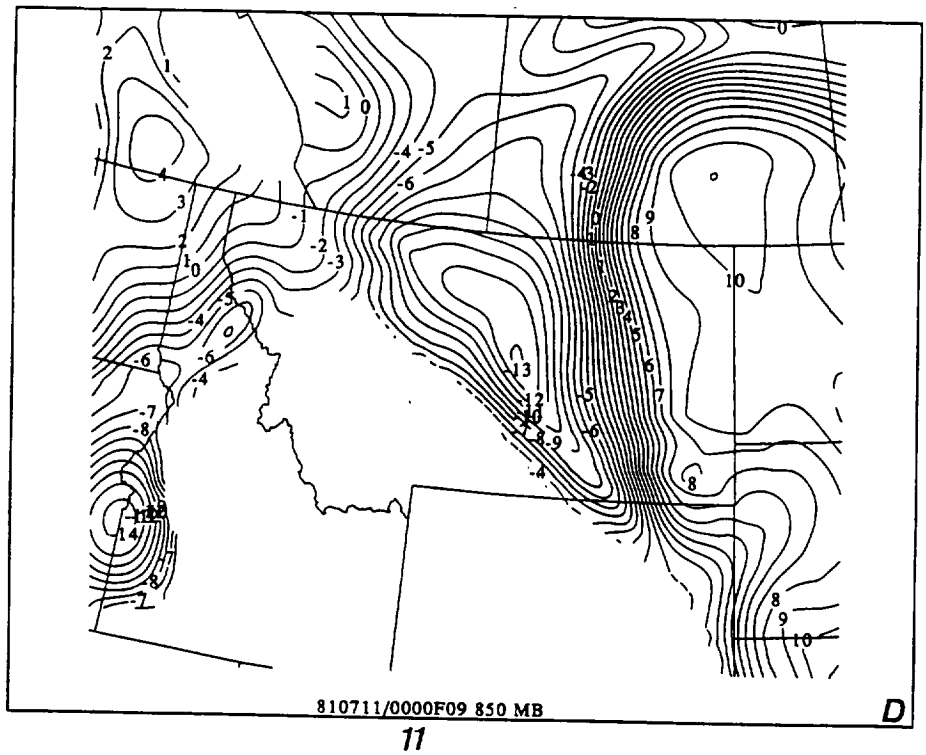
810711/0000F09 850 MB
D

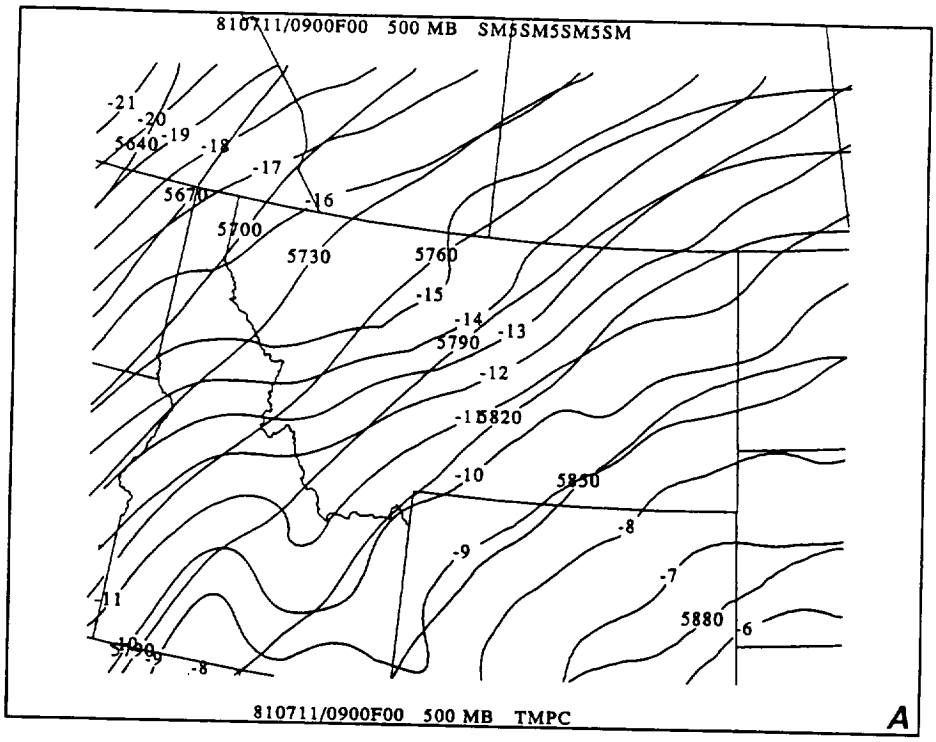
810711/0900F00 500 MB SM5SM5SM5SM
-21
-20
5640
-19
-18
-17
5670
-16
5700
5730
5760
-15
-14
5790
-13
-12
-11
5820
-10
5850
-8
-9
-7
5880
-6
810711/0900F00 500 MB TMPC
A

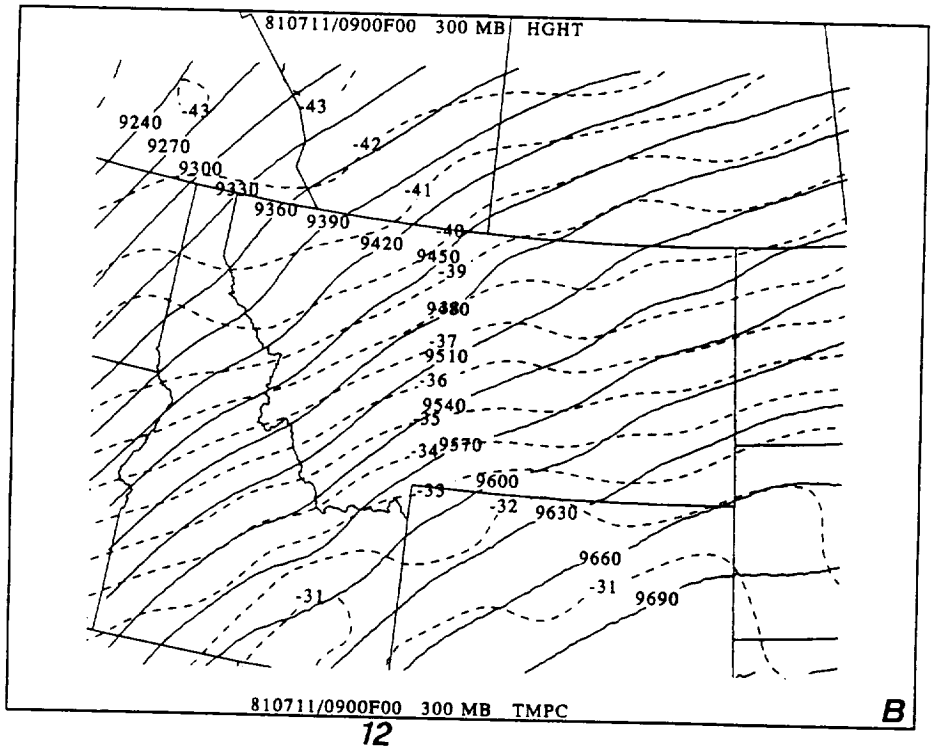
810711/0900F00 300 MB HGHT
9240
-43
-43
9270
-42
9300
9330
-41
9360
9390
-40
9420
9450
-39
9480
-37
9510
-36
9540
-35
-34
9570
9600
-33
-32
9630
9660
-31
9690
-31
810711/0900F00 300 MB TMPC
B

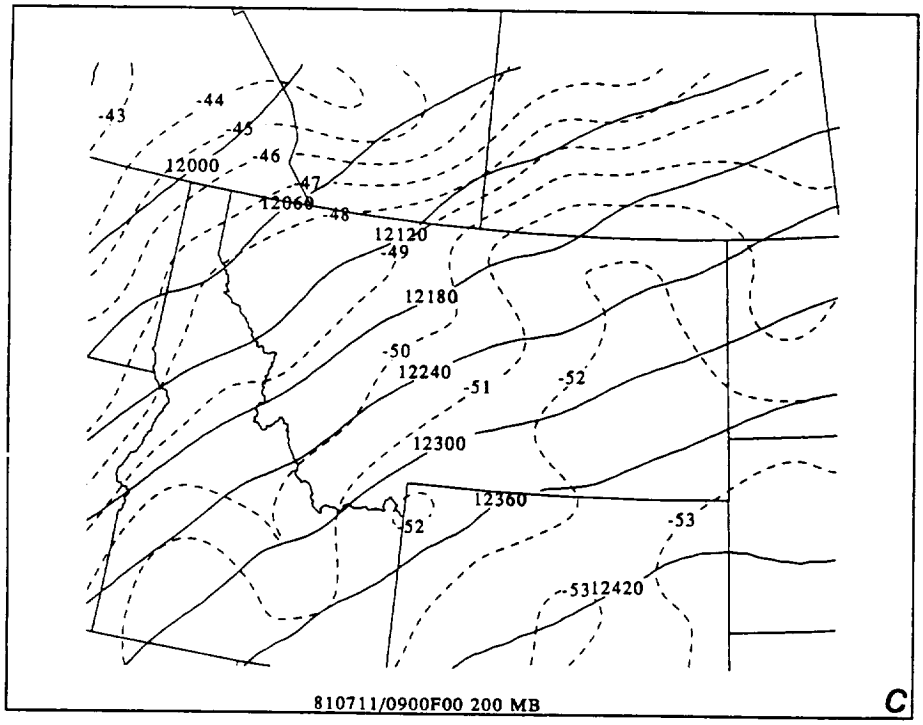
-43
-44
-45
-46
-47
-48
-49
-50
-51
-52
-52
-53
-5312420
12000
12060
12120
12180
12240
12300
12360
810711/0900F00 200 MB
C

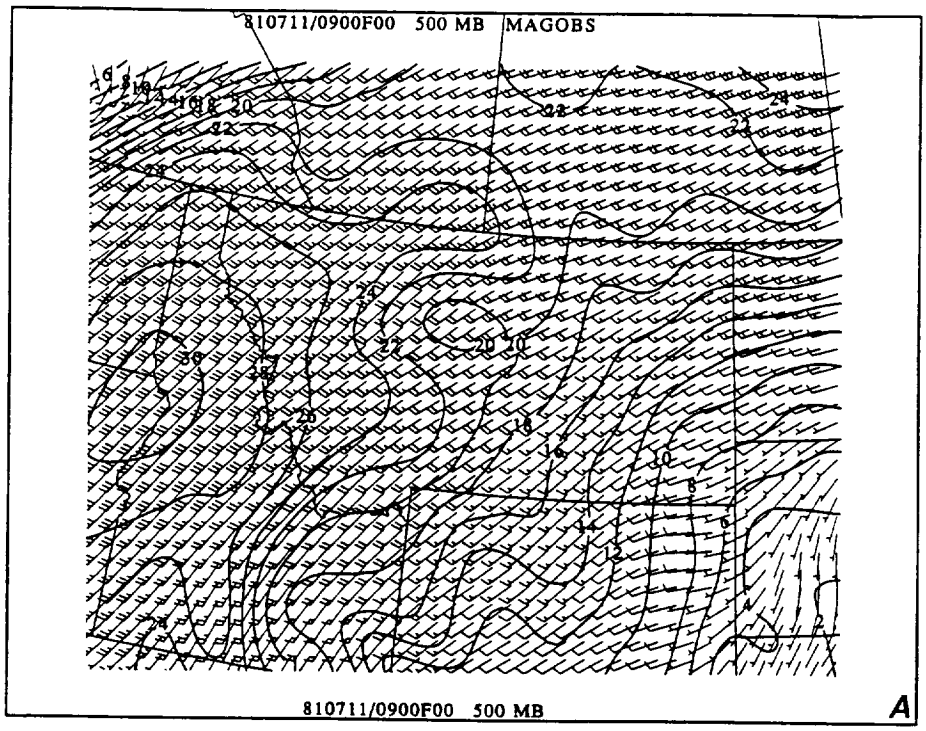
810711/0900F00 500 MB MAGOBS
810711/0900F00 500 MB
A

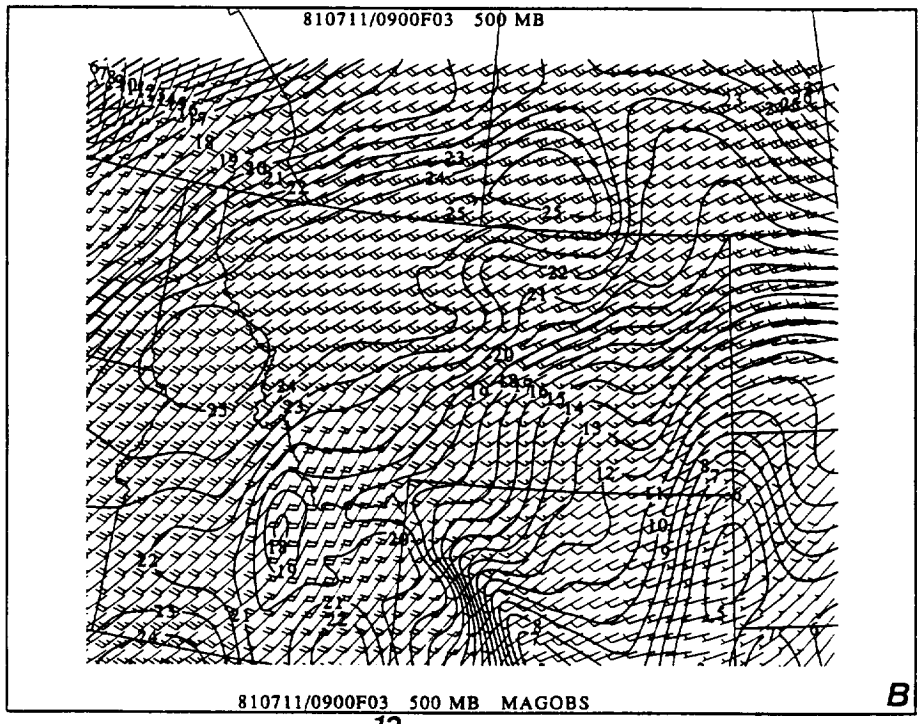
810711/0900F03 500 MB
810711/0900F03 500 MB MAGOBS
B

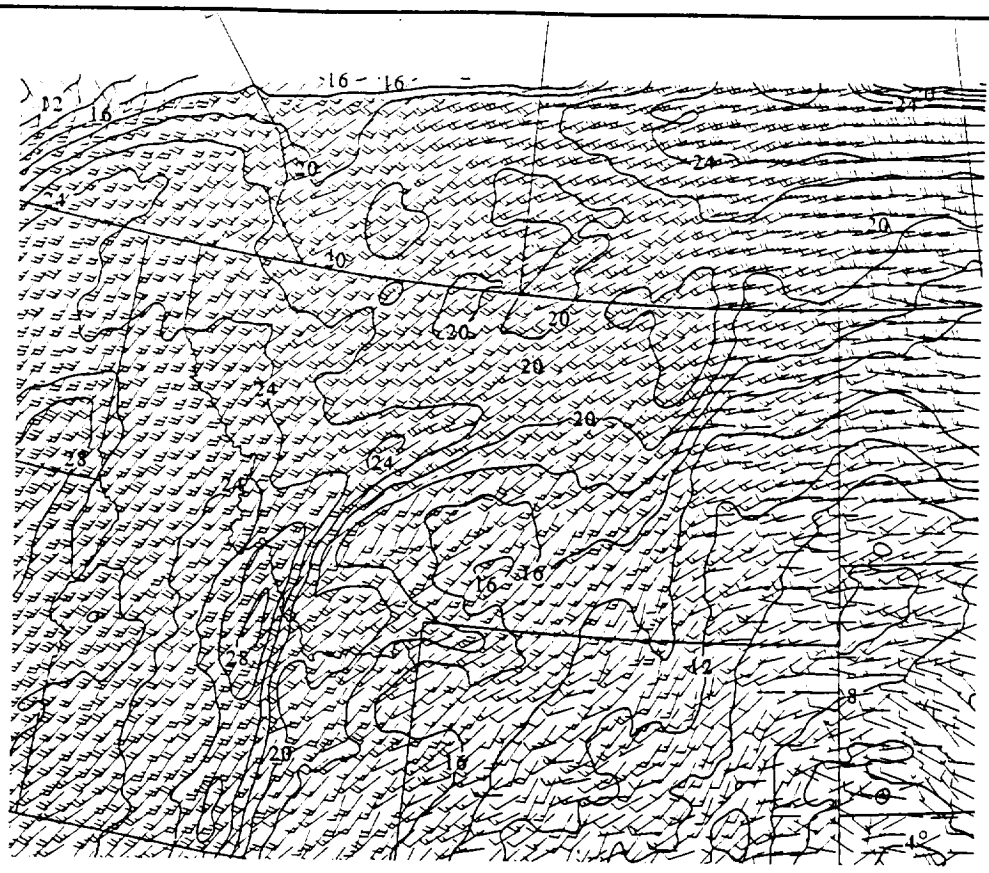

c

810711/0900F03 500 MB MAG GEO nest

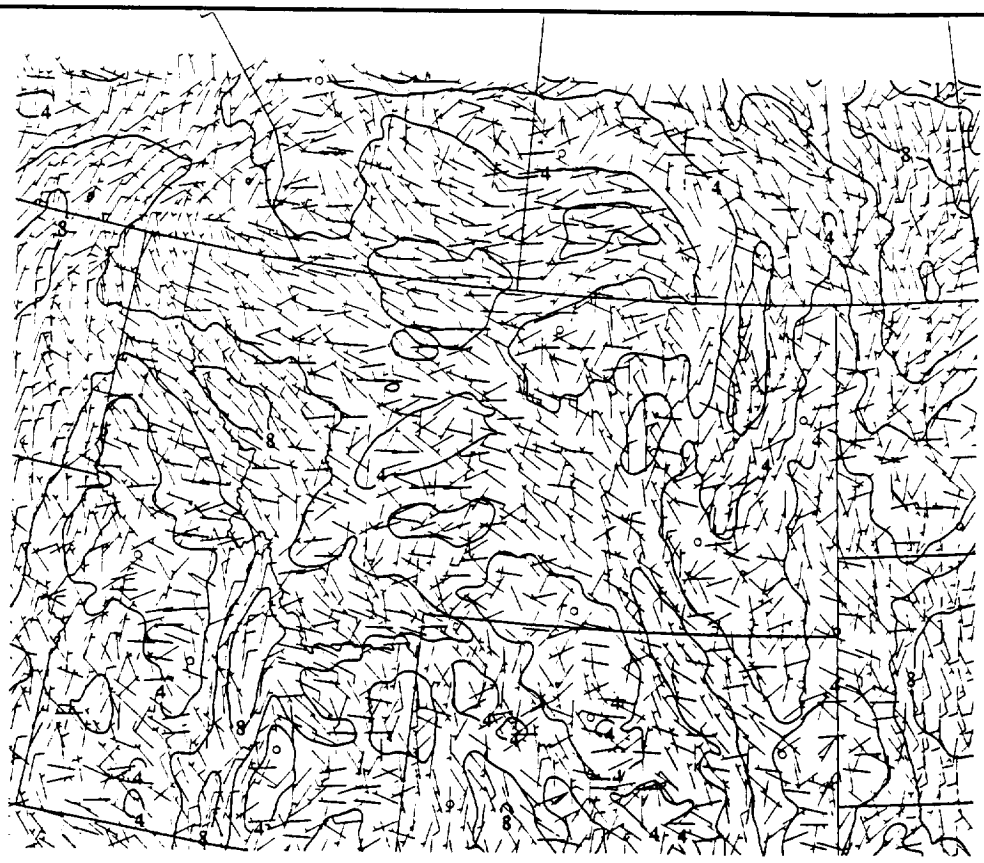

d

810711/0900F03 500 MB MAG AGE nest

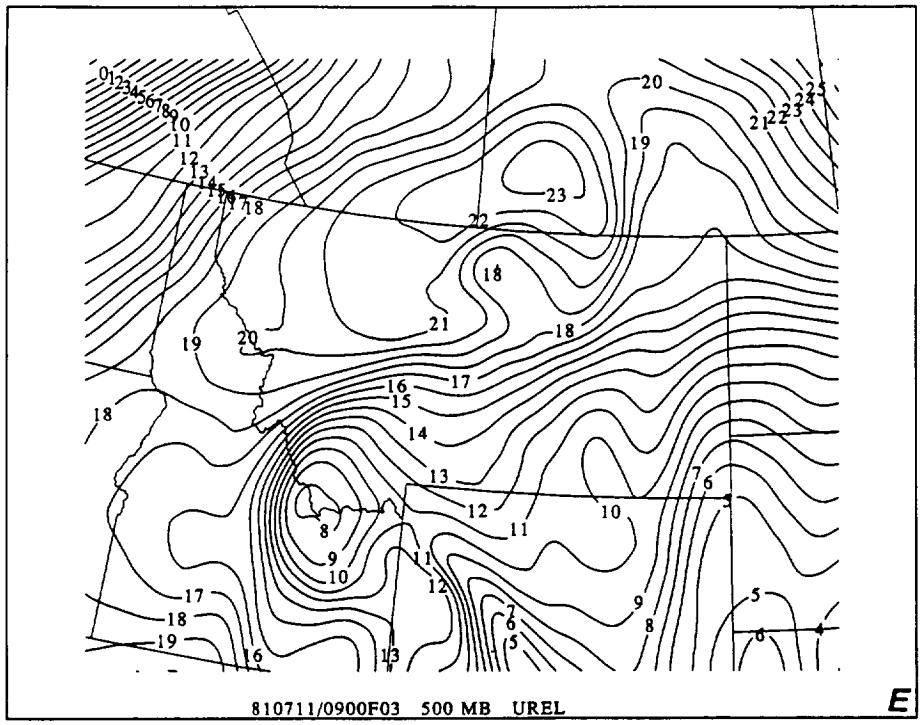
810711/0900F03 500 MB UREL
E

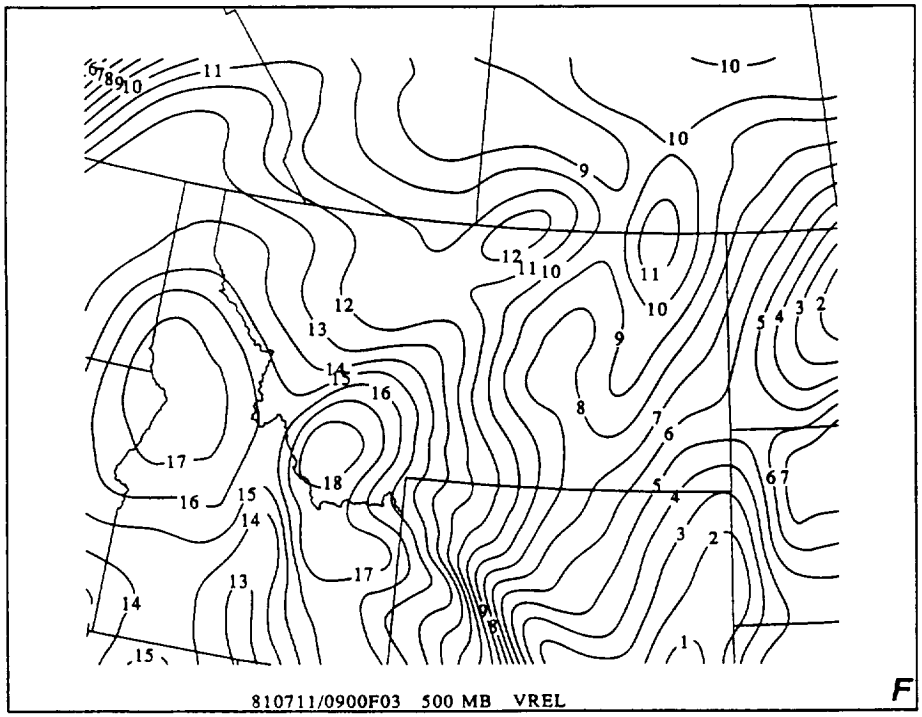
810711/0900F03 500 MB VREL
F

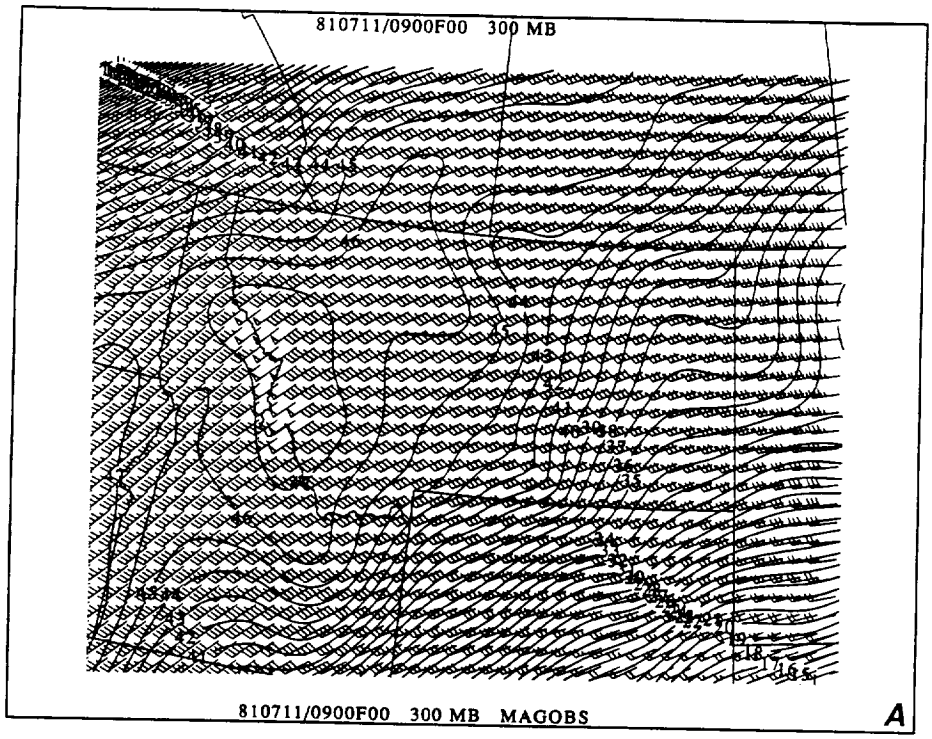
810711/0900F00 300 MB
810711/0900F00 300 MB MAGOBS
A

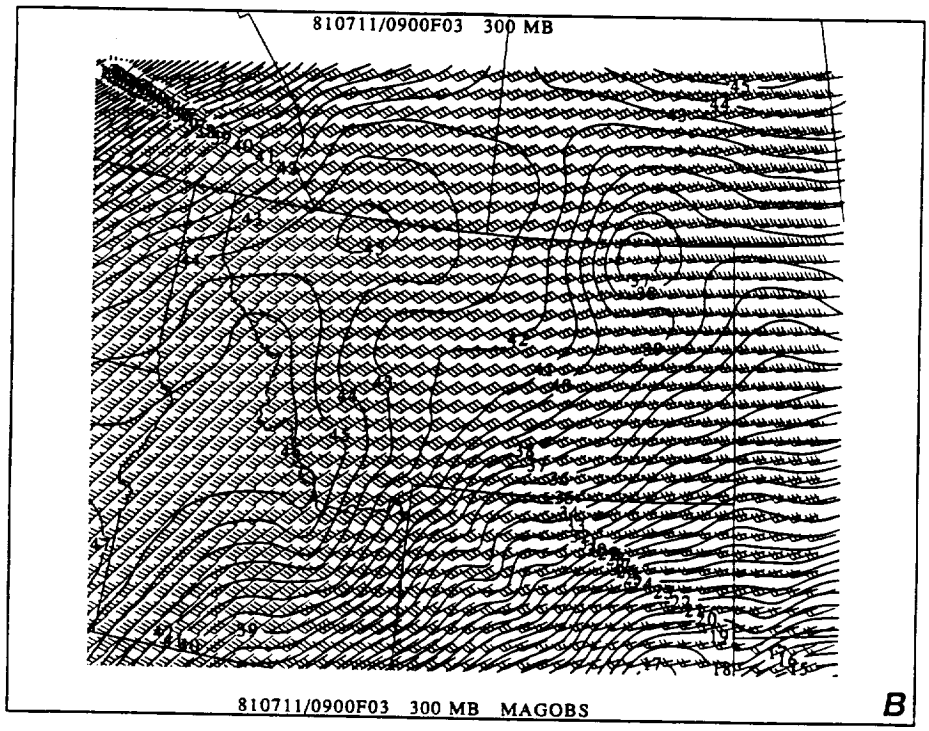
810711/0900F03 300 MB
810711/0900F03 300 MB MAGOBS
B

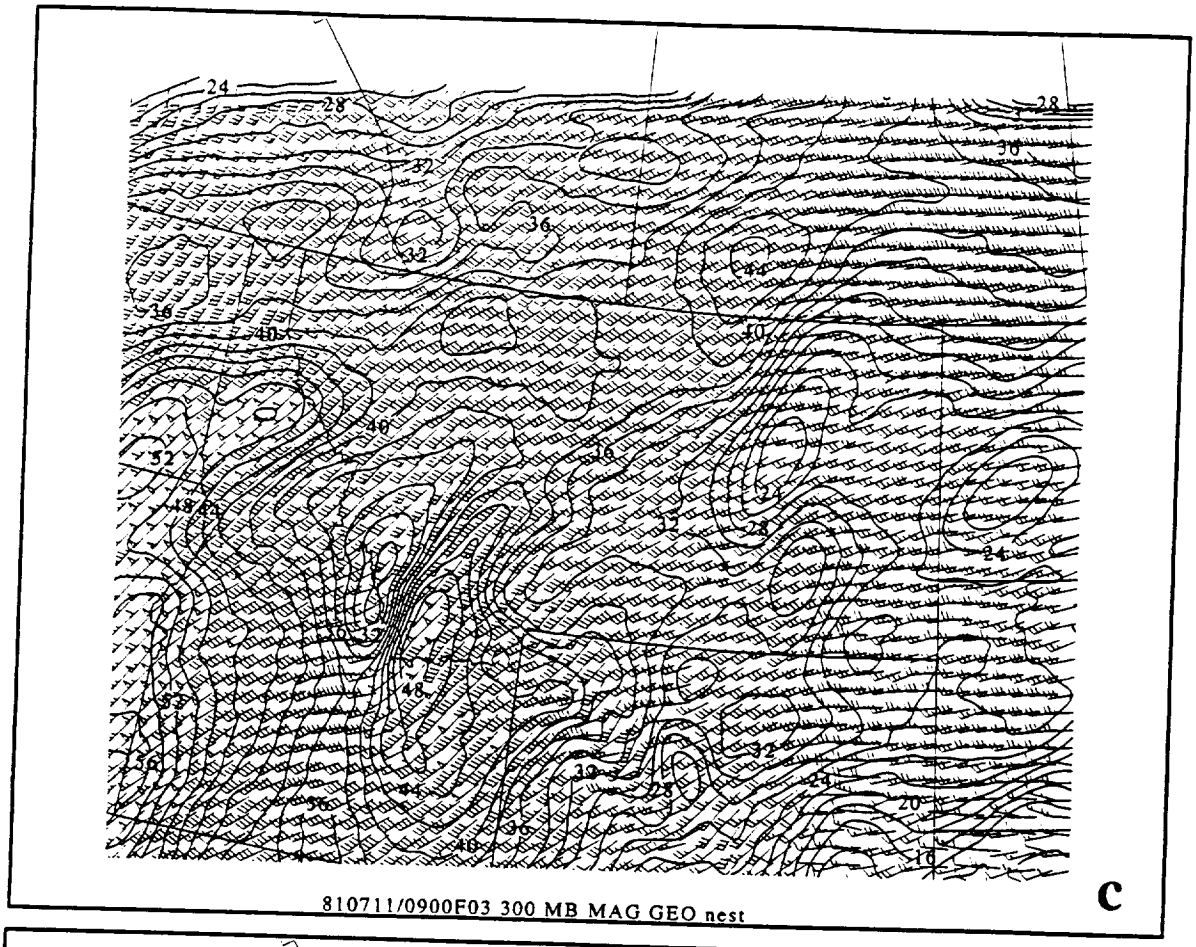

810711/0900F03 300 MB MAG GEO nest

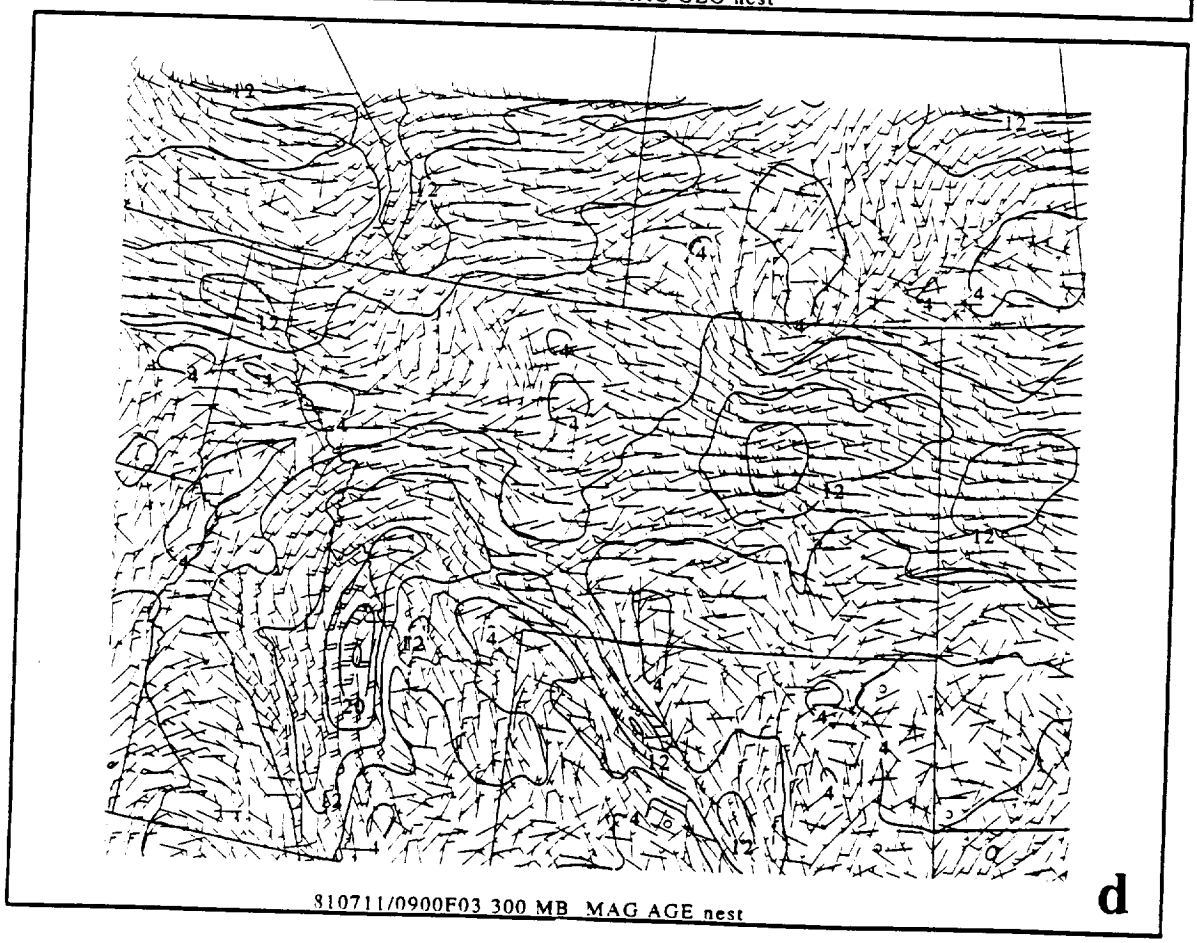

810711/0900F03 300 MB MAG AGE nest

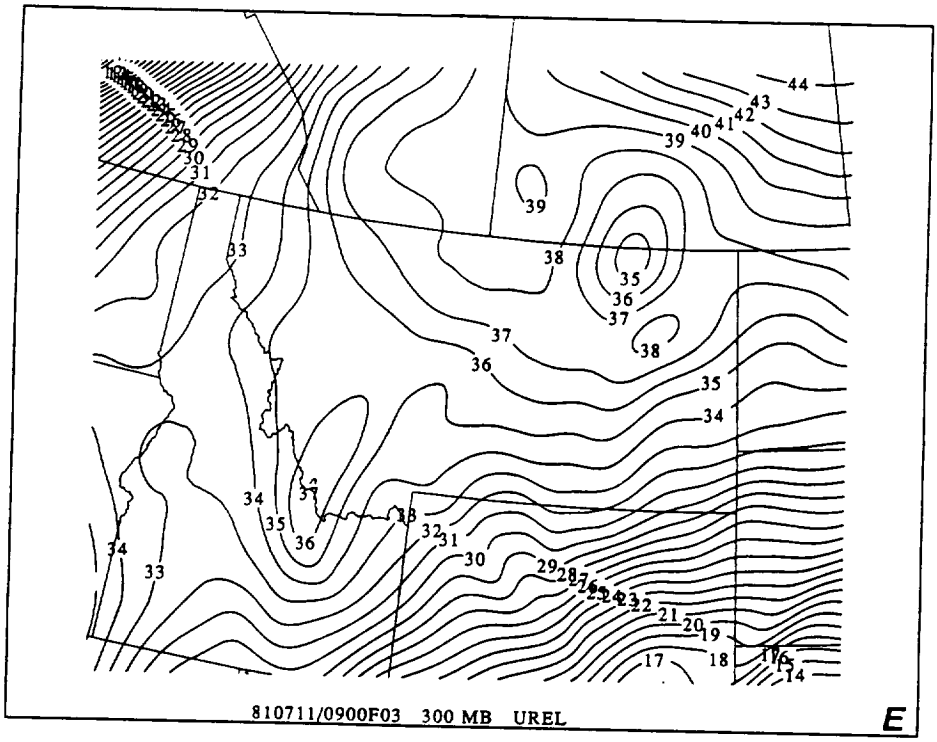
810711/0900F03 300 MB UREL
E

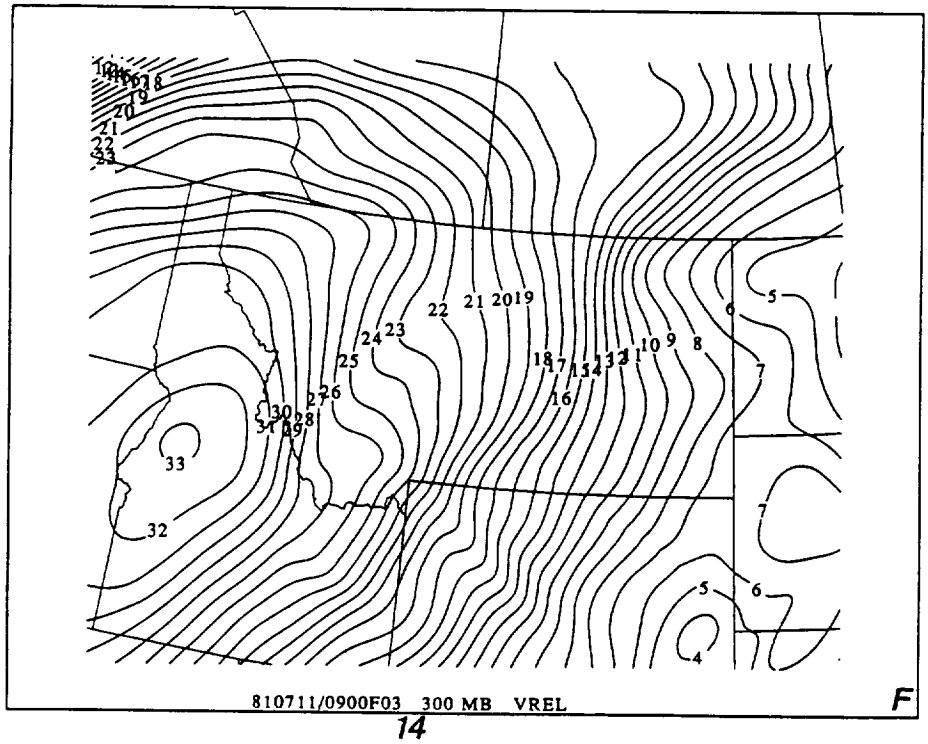
810711/0900F03 300 MB VREL
F

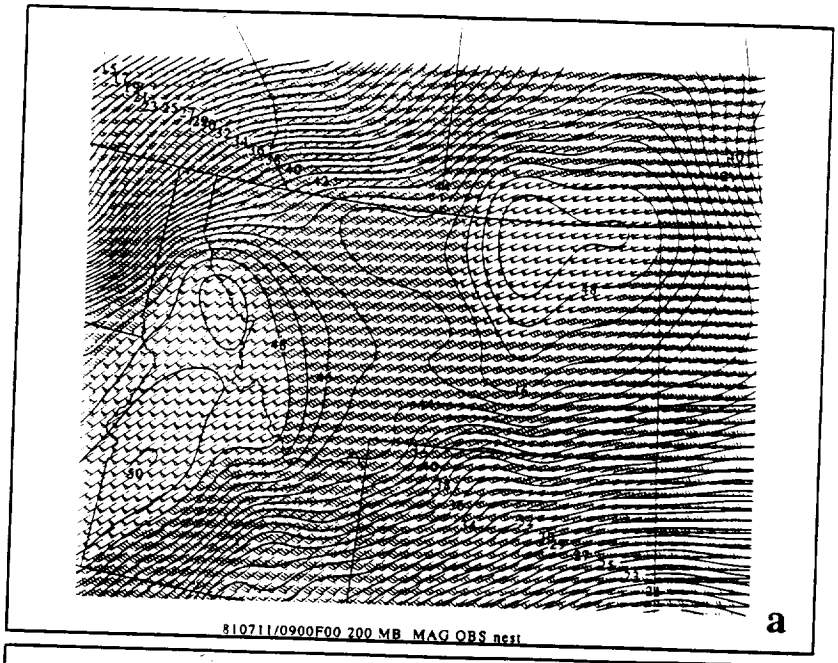
810711/0900F00 200 MB MAG OBS nest
a

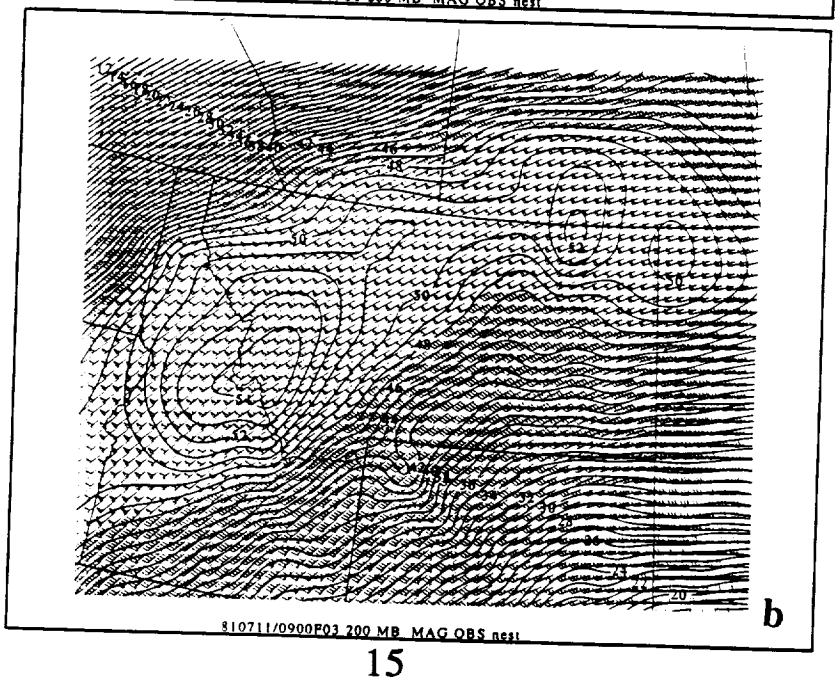
810711/0900F03 200 MB MAG OBS nest
b

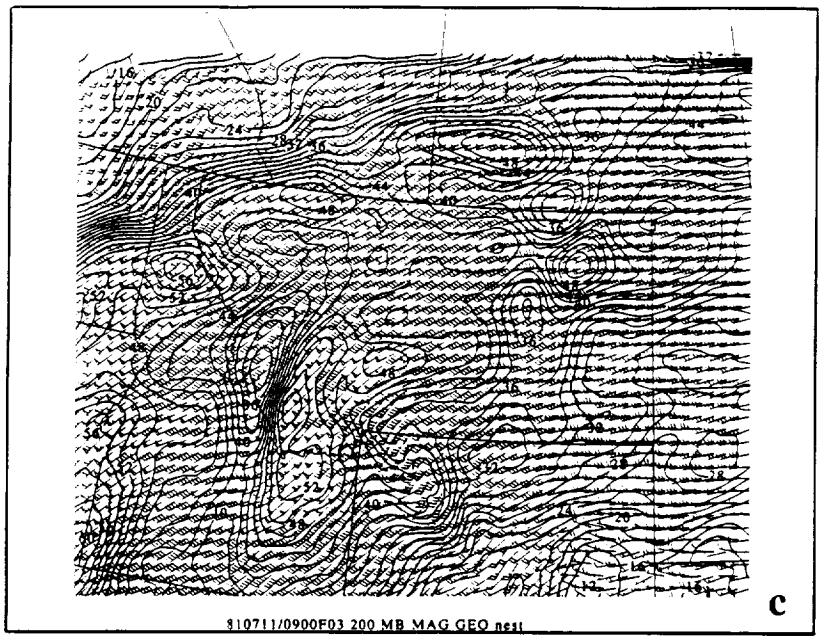
c
810711/0900F03 200 MB MAG GEO nest

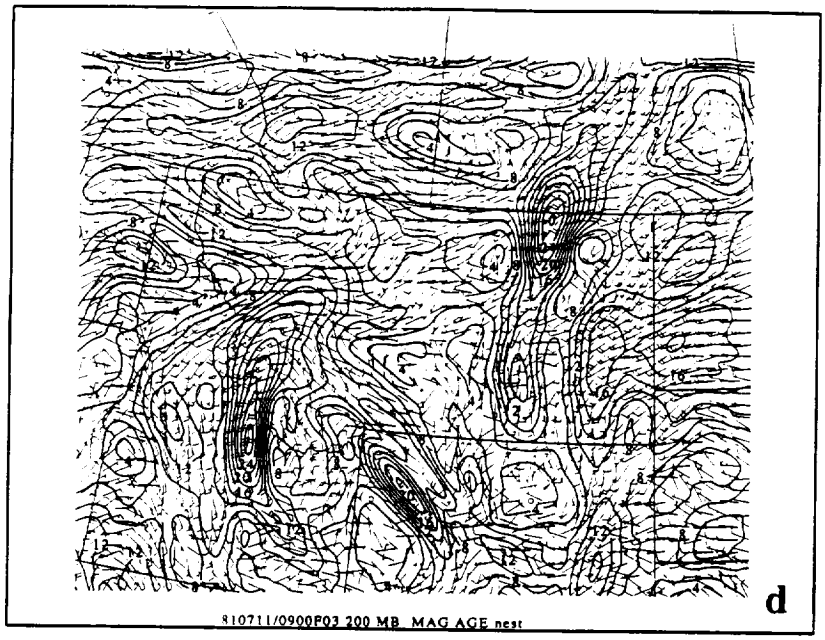
d
810711/0900F03 200 MB MAG AGE nest

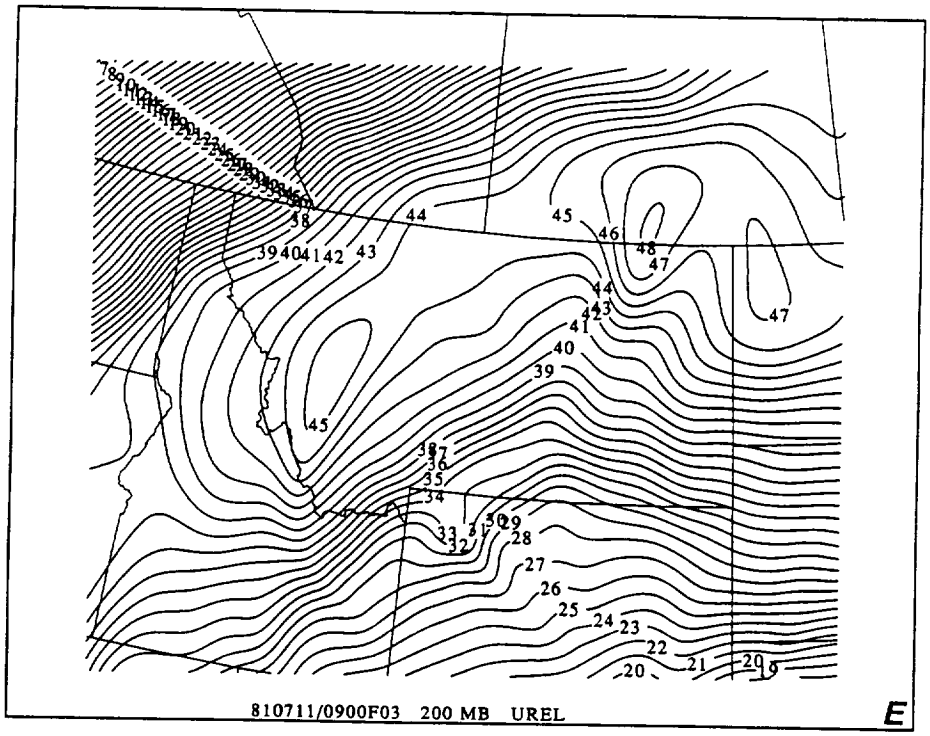
810711/0900F03 200 MB UREL
E

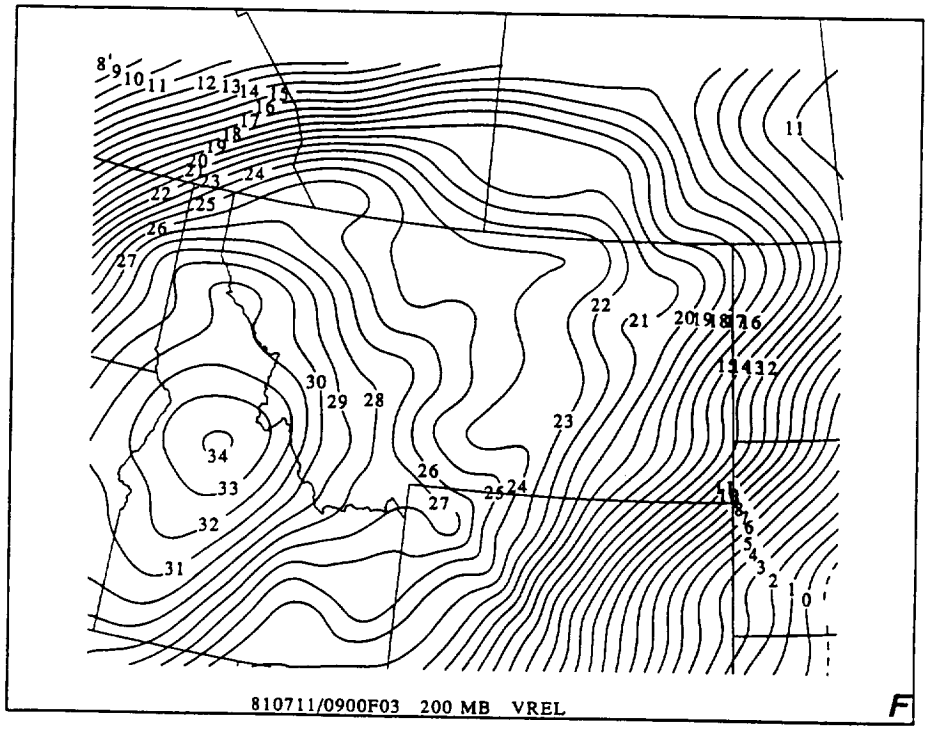
810711/0900F03 200 MB VREL
F

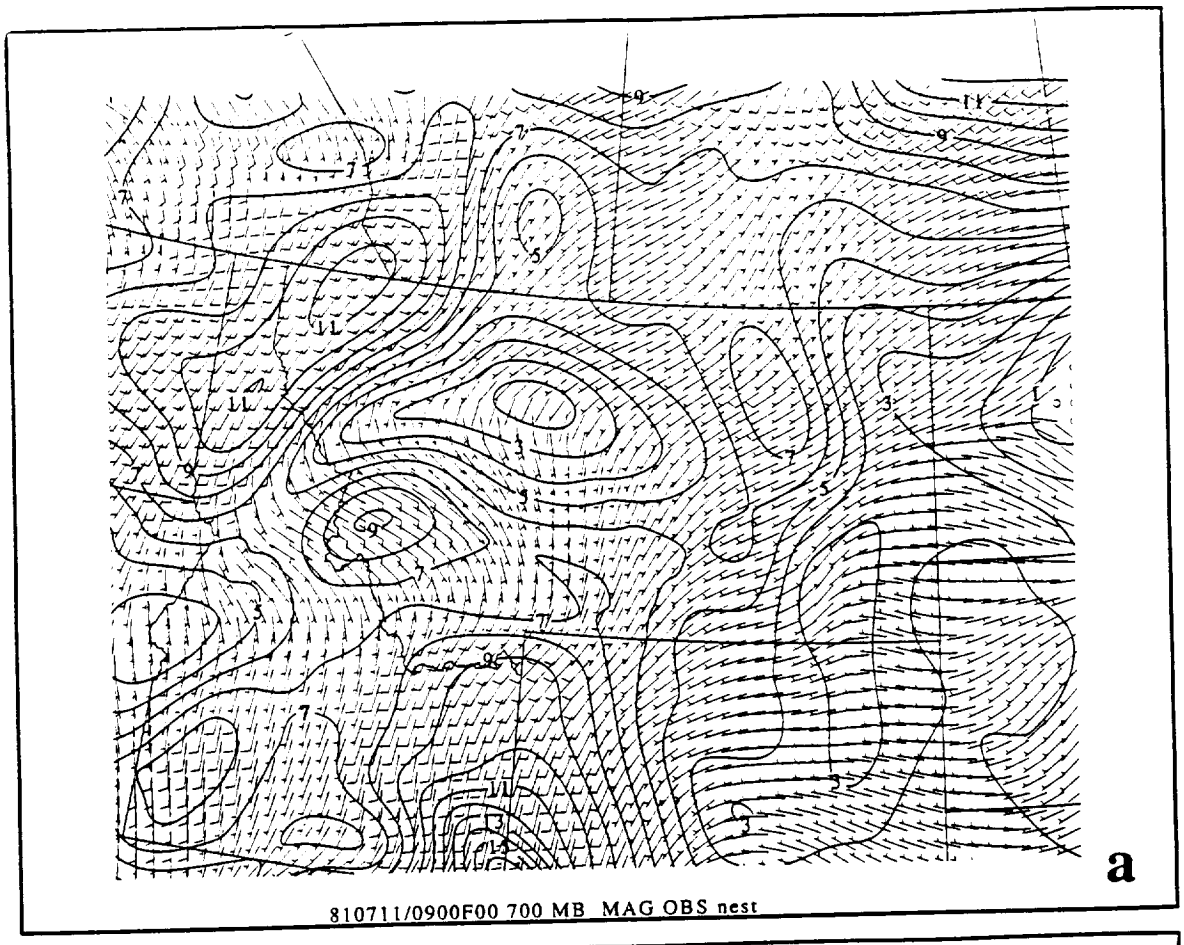

810711/0900F00 700 MB MAG OBS nest

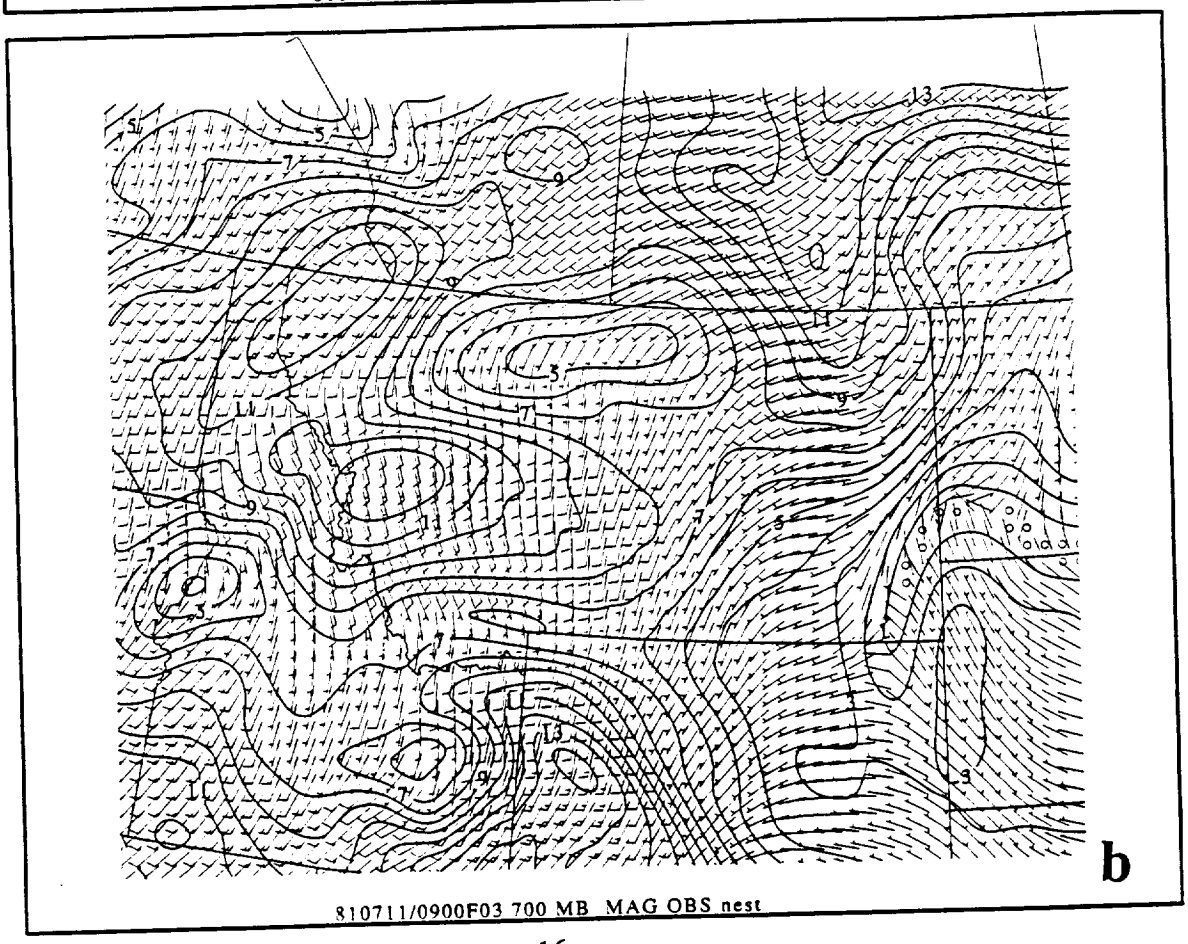

810711/0900F03 700 MB MAG OBS nest

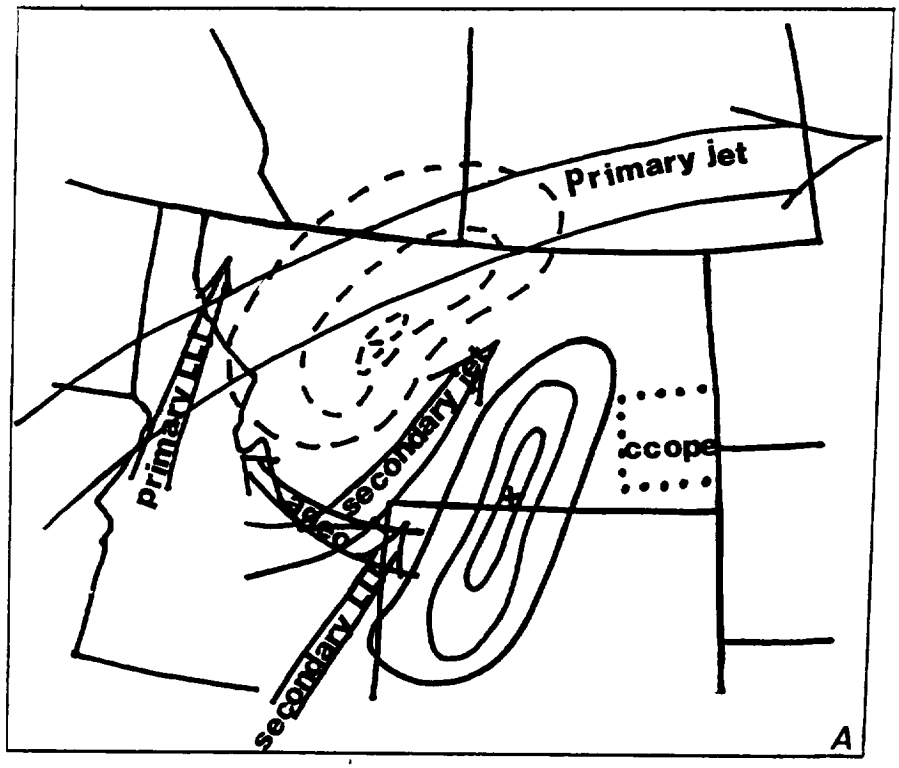
Primary jet
primary LLJ
secondary jet
secondary LLJ
ccope
A

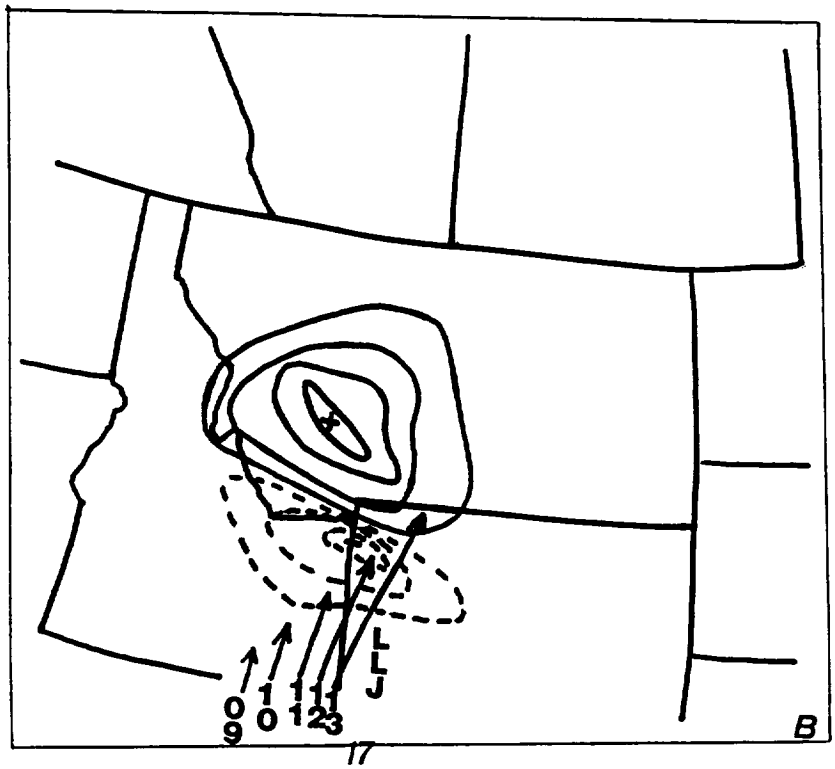
LLJ
09
00
12
23
B

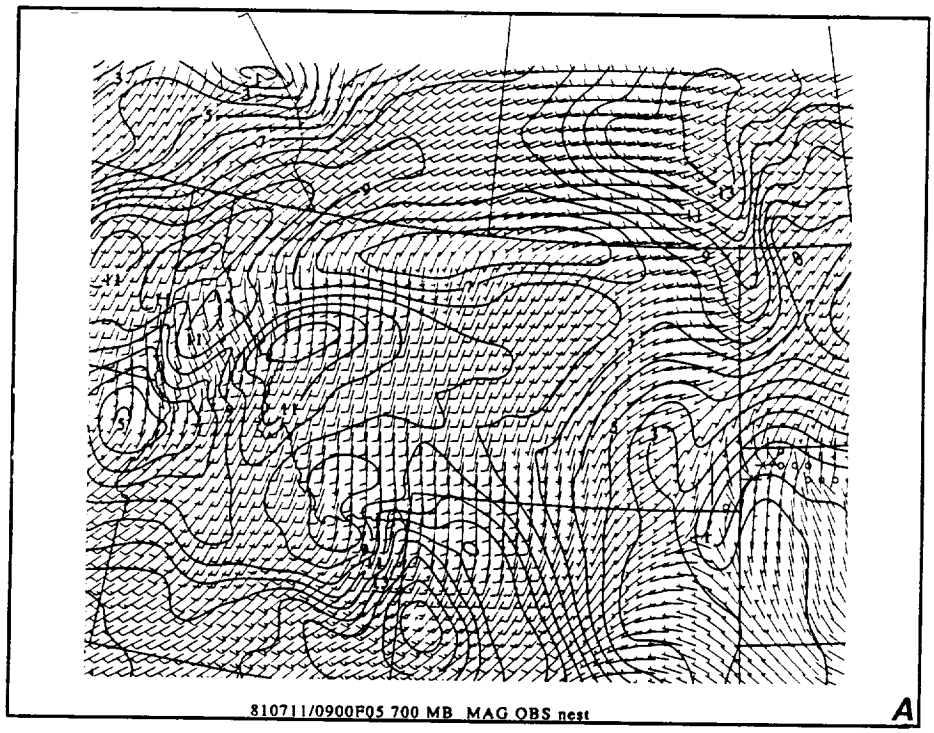

810711/0900F05 700 MB MAG OBS nest

A

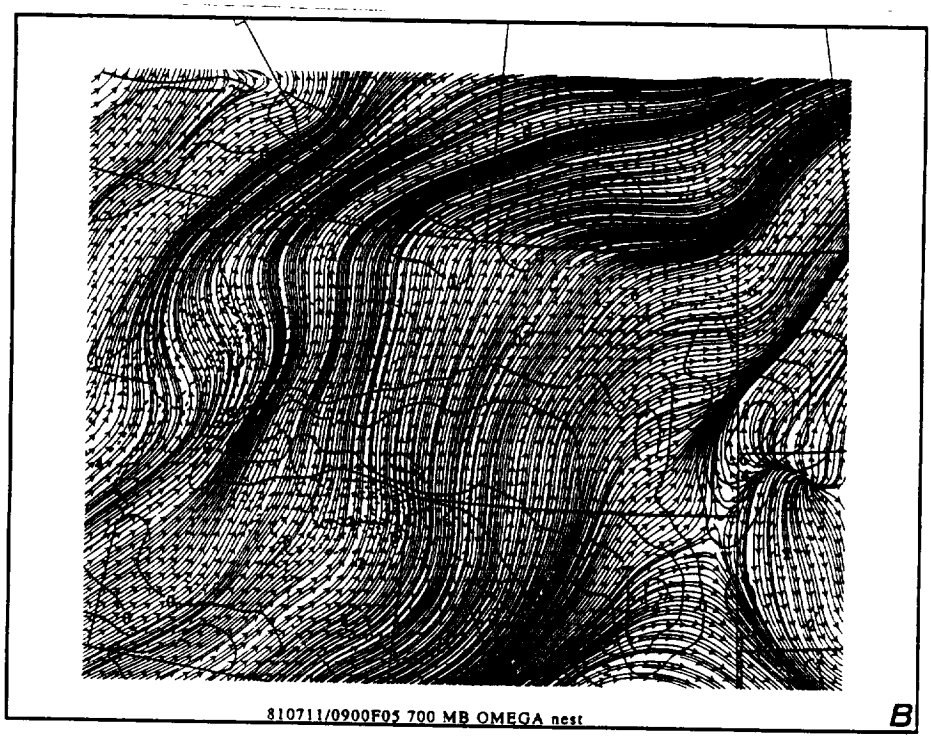

810711/0900F05 700 MB OMEGA nest

B

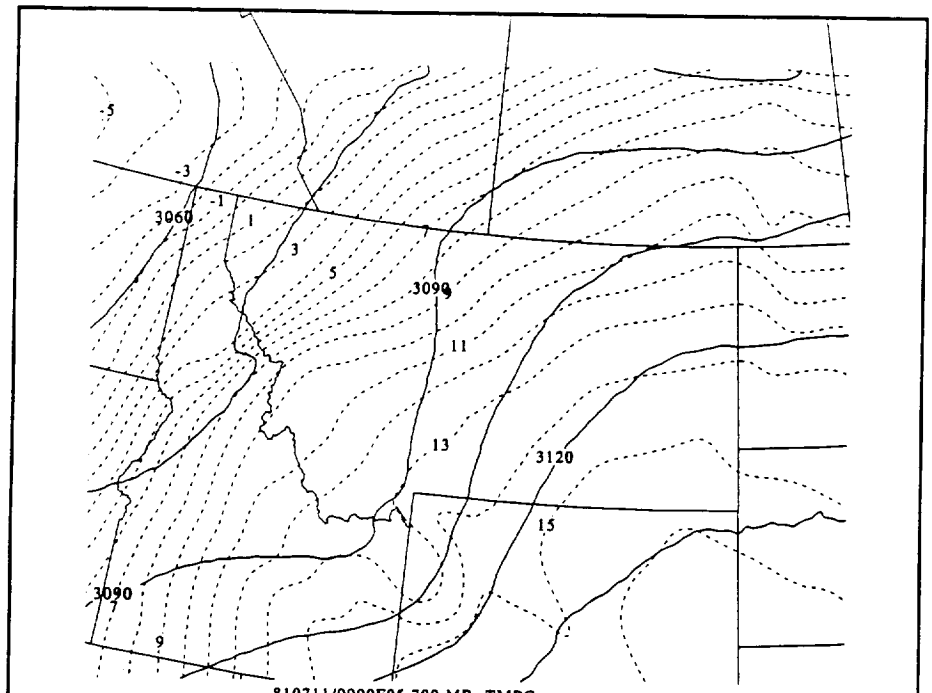

810711/0900F05 700 MB TMPC nest
810711/0900F05 700 MB HEIGHT nest

C

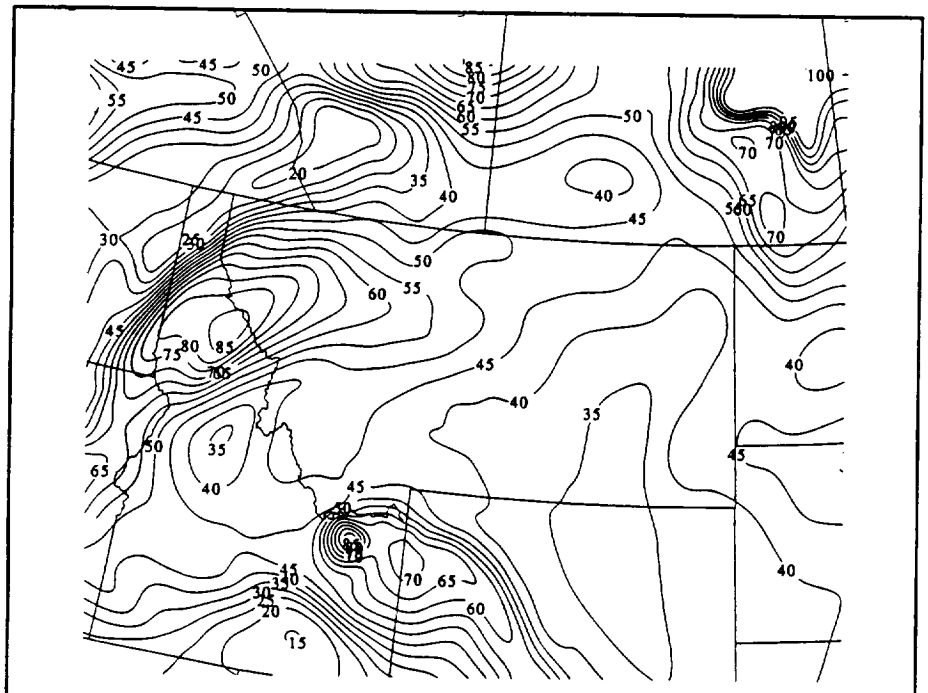

810711/0900F05 700 MB RELH nest

D

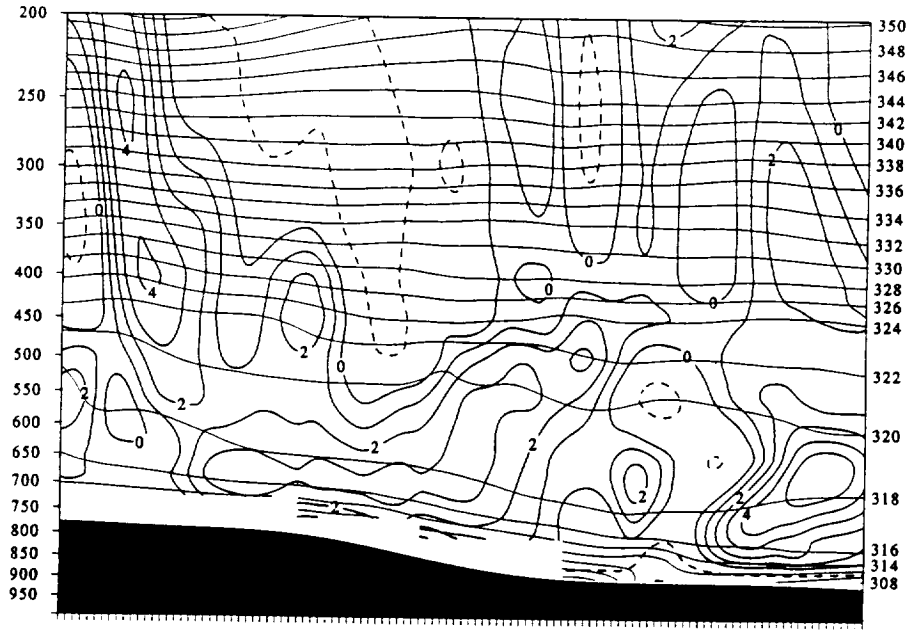

810711/0900F05 OMEGA nest
810711/0900F05 THETA nest

A

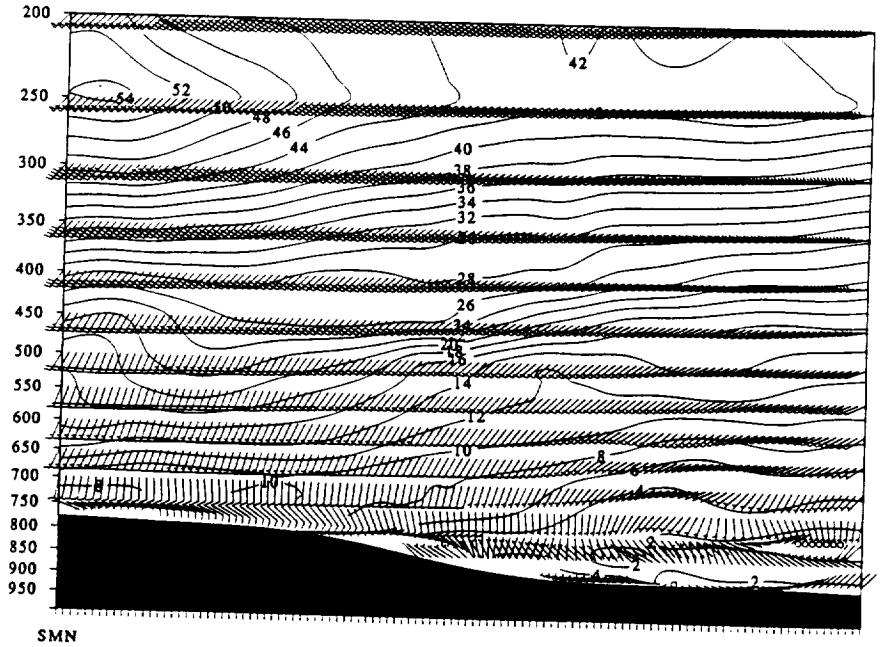

810711/0900F05 MAGOBS nest

B

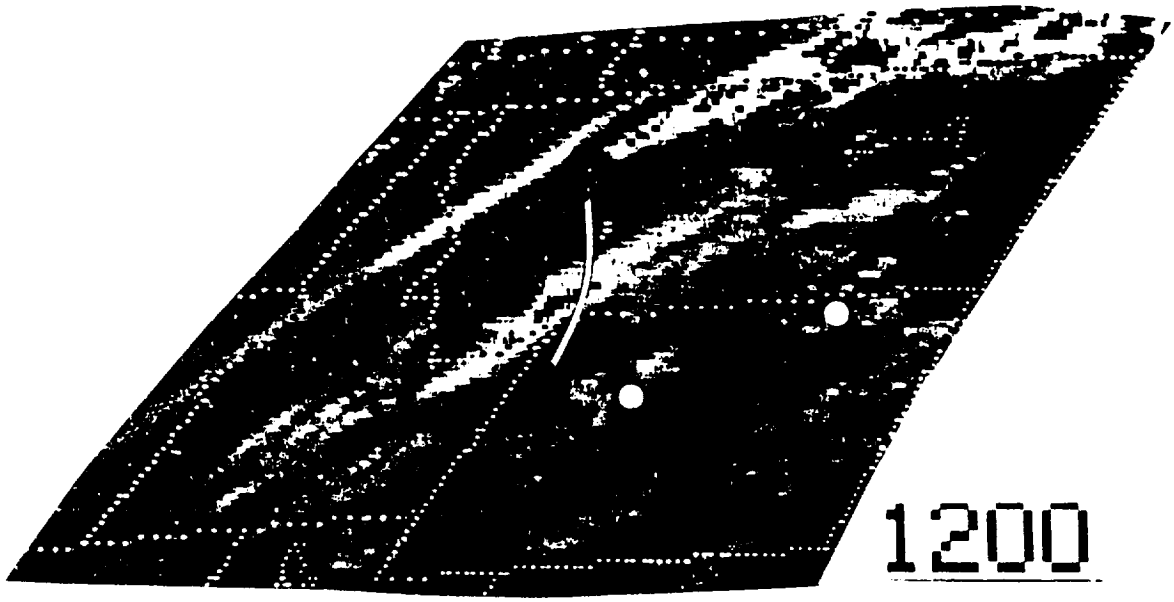

A

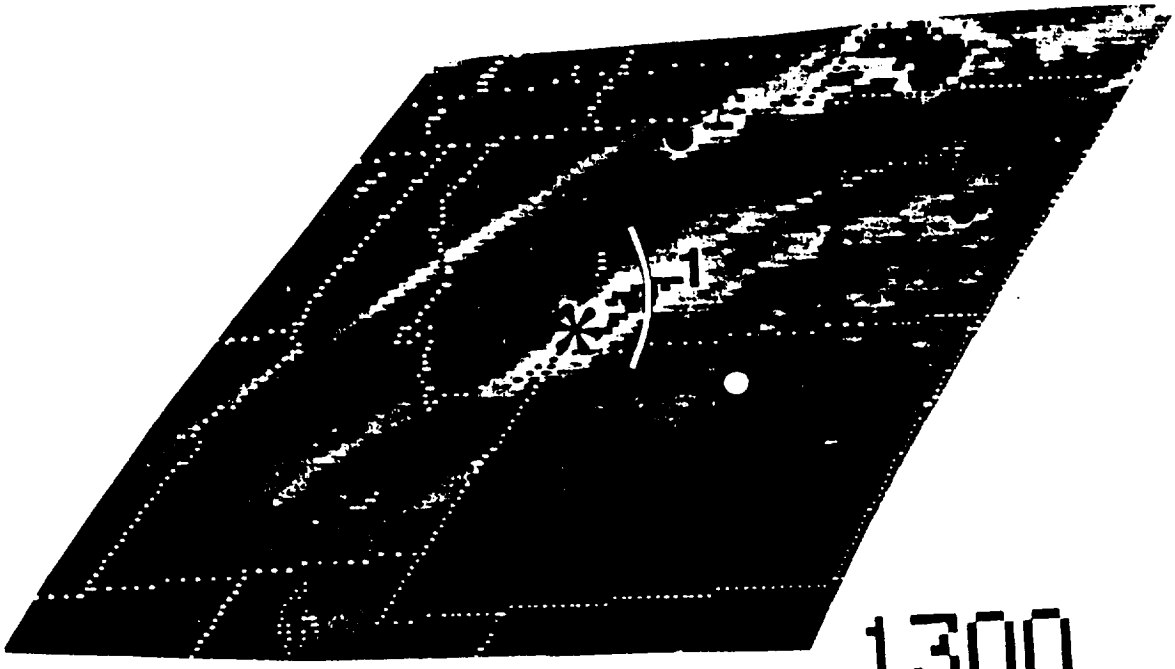

B

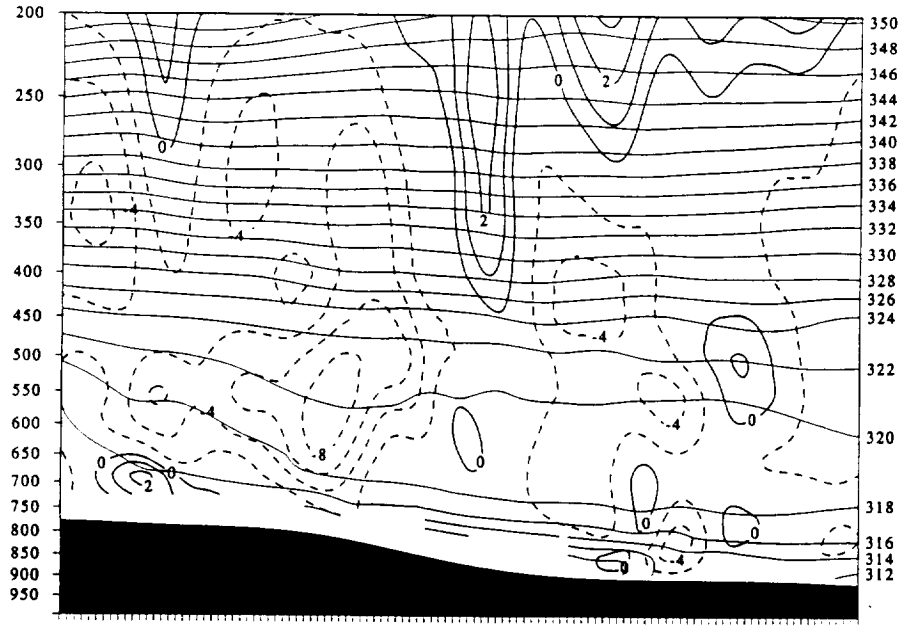

810711/0900F07 OMEGA nest
810711/0900F07 THETA nest

A

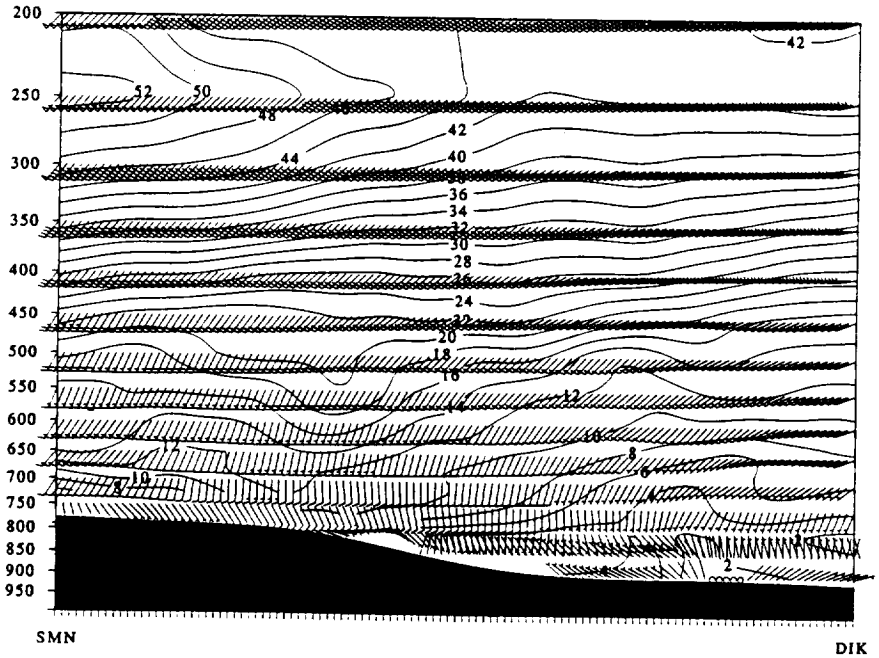

810711/0900F07 MAGOBS nest

B

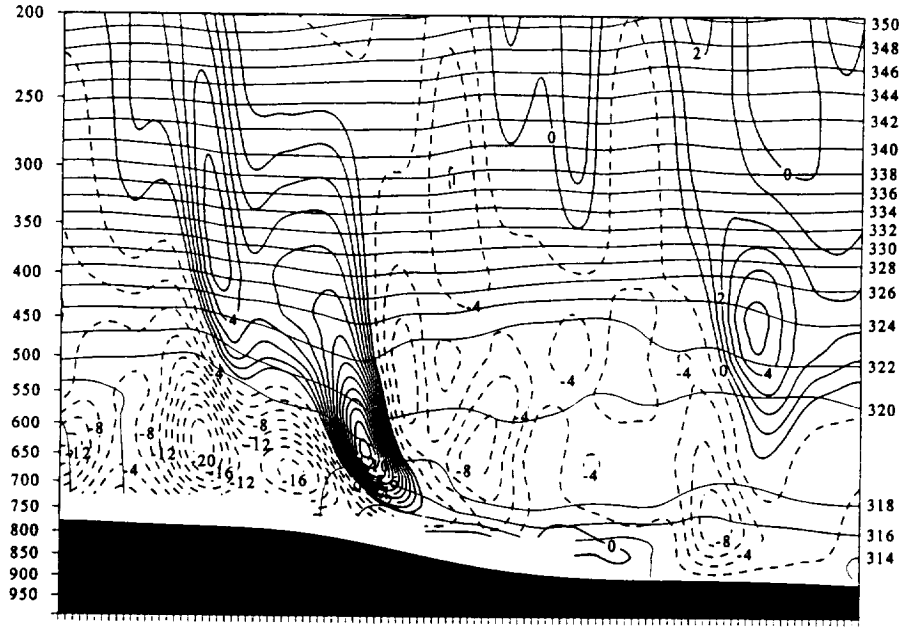

810711/0900F10 OMEGA nest
810711/0900F10 THETA nest

C

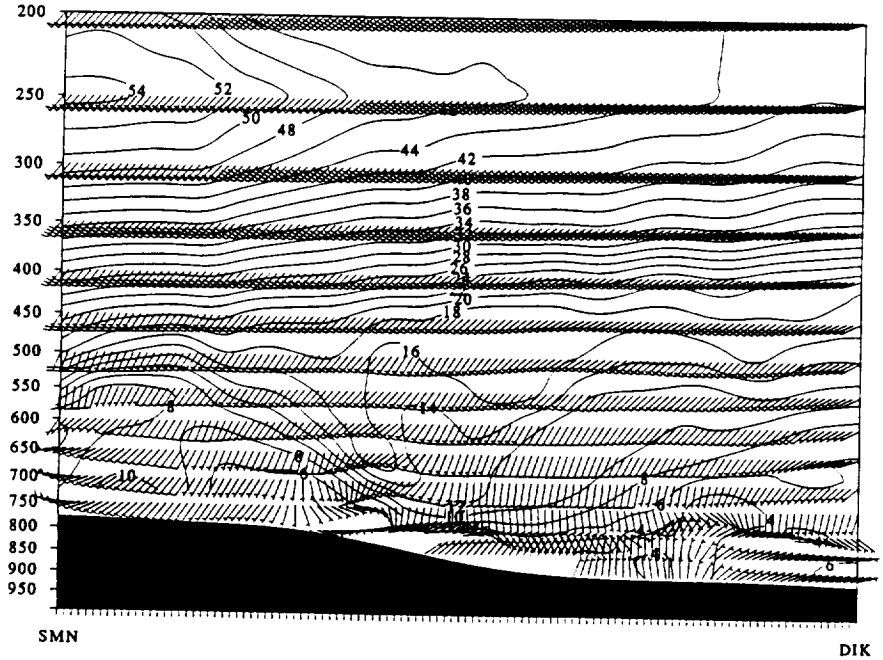

810711/0900F10 MAGOBS nest

D

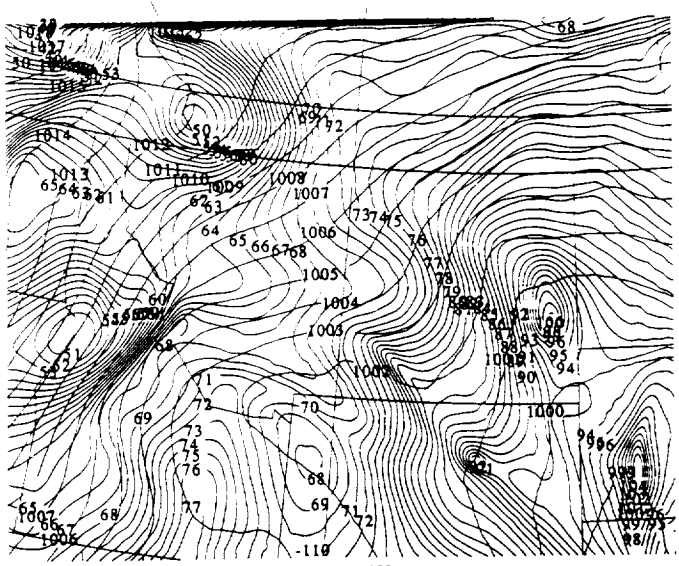

810711/0900F07 SFC PMSL nest
810711/0900F07 SFC TMPF nest

a

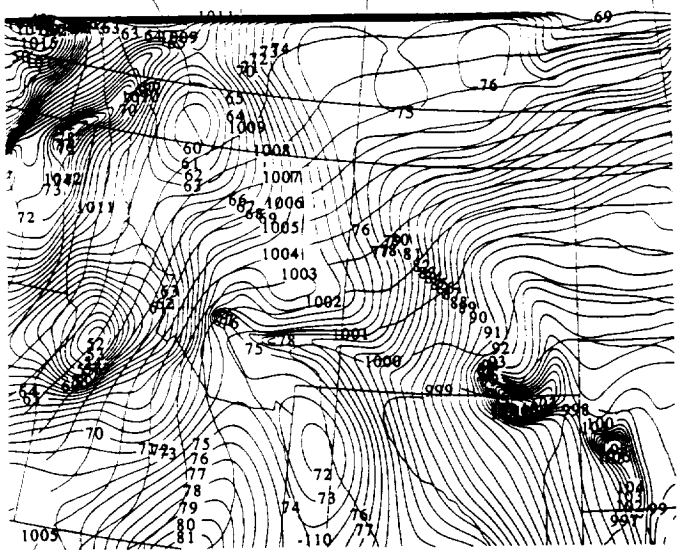

810711/0900F10 SFC PMSL nest
810711/0900F10 SFC TMPF nest

b

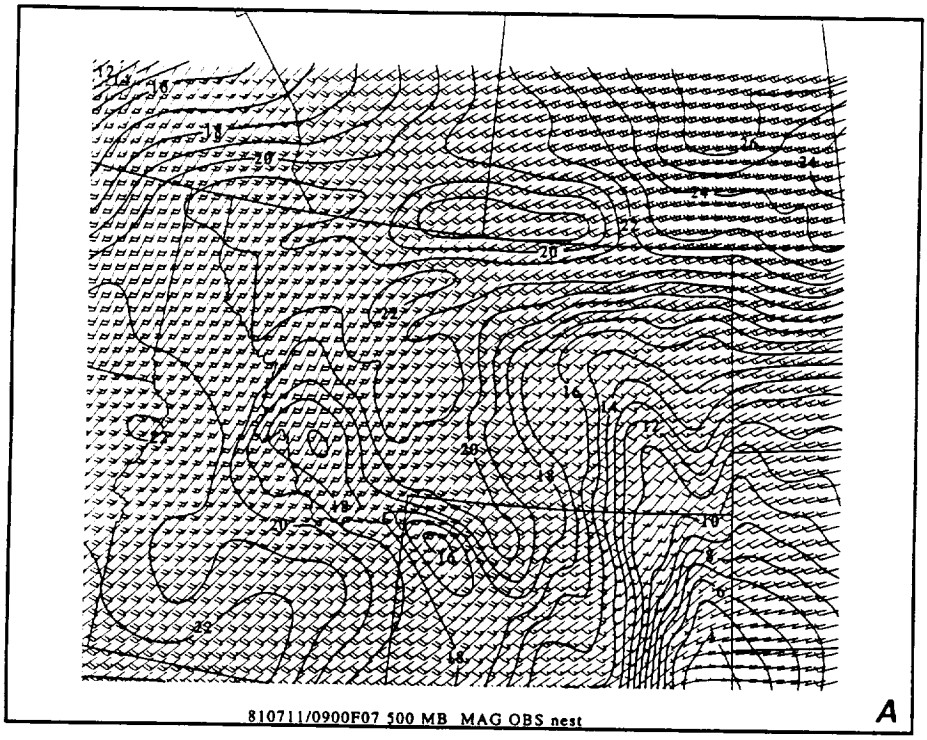
810711/0900F07 500 MB MAG OBS nest
A

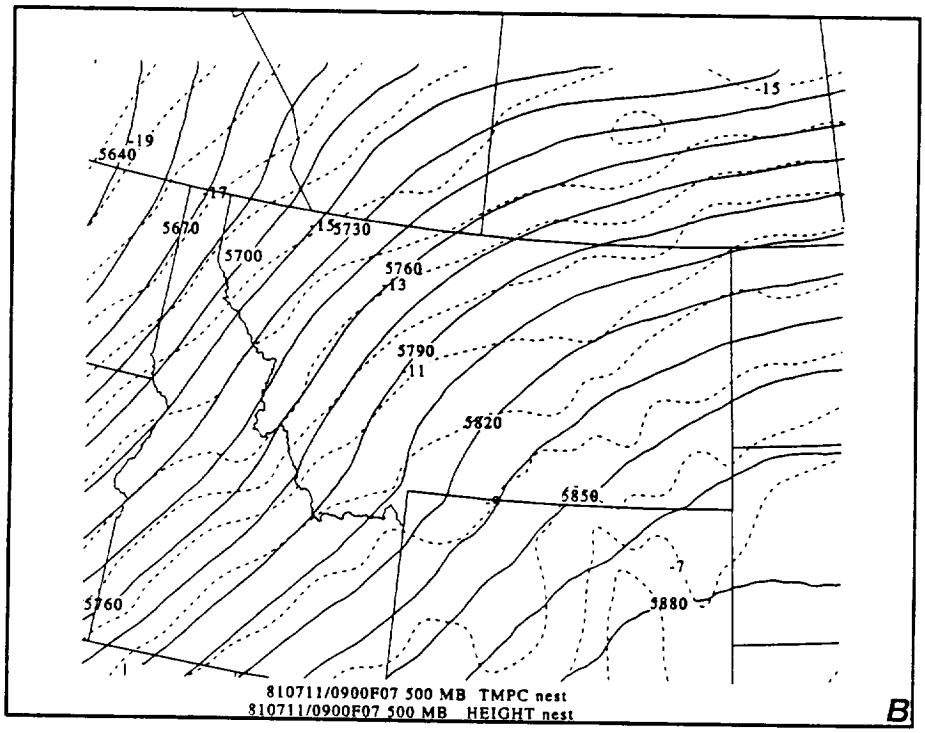
5640
5670
5700
5730
5760
5790
5820
5850
5880
810711/0900F07 500 MB TMPC nest
810711/0900F07 500 MB HEIGHT nest
B

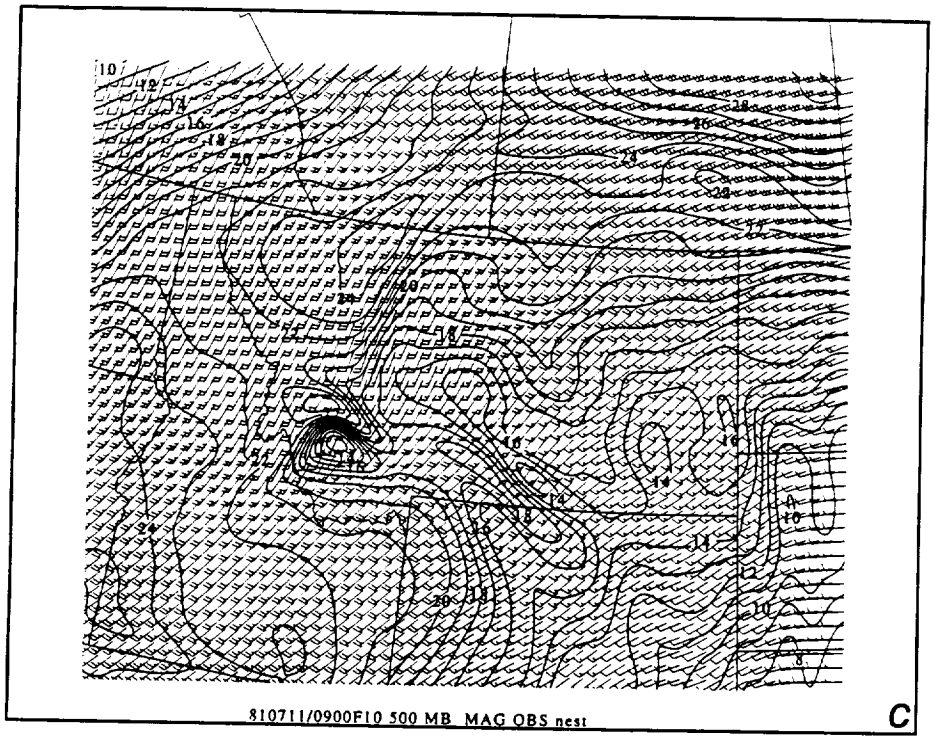
810711/0900F10 500 MB MAG OBS nest
C

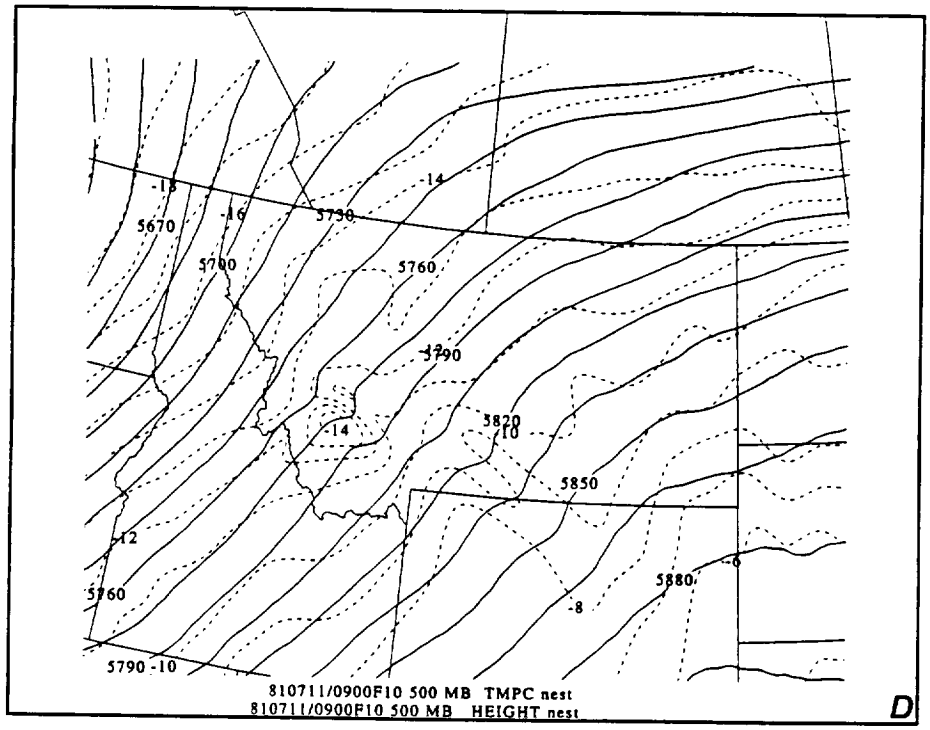
5670
5700
5730
5760
5790
5820
5850
5880
810711/0900F10 500 MB TMPC nest
810711/0900F10 500 MB HEIGHT nest
D

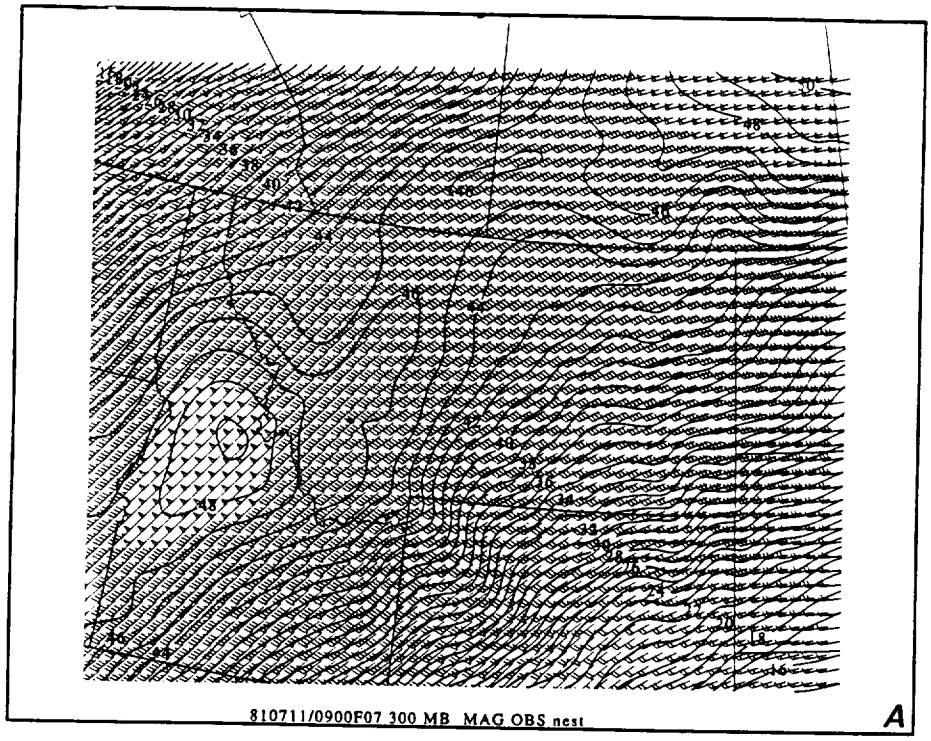
810711/0900F07 300 MB MAG OBS nest
A

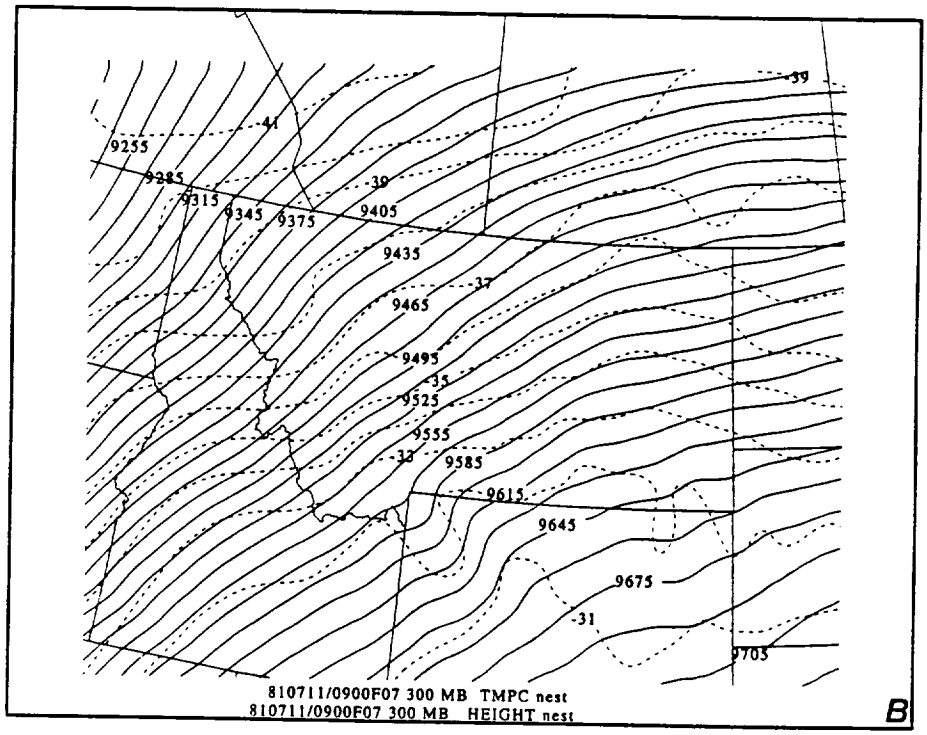
9255
9285
9315
9345
9375
9405
9435
9465
9495
9525
9555
9585
9615
9645
9675
9705
-41
-39
-37
-35
-33
-31
810711/0900F07 300 MB TMPC nest
810711/0900F07 300 MB HEIGHT nest
B

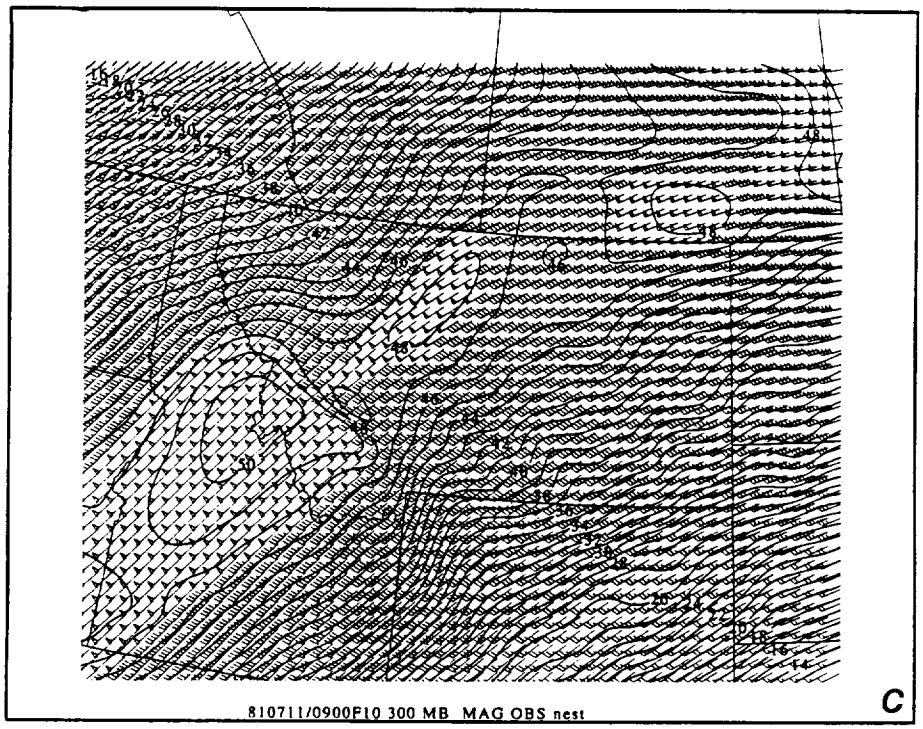

810711/0900F10 300 MB MAG OBS nest

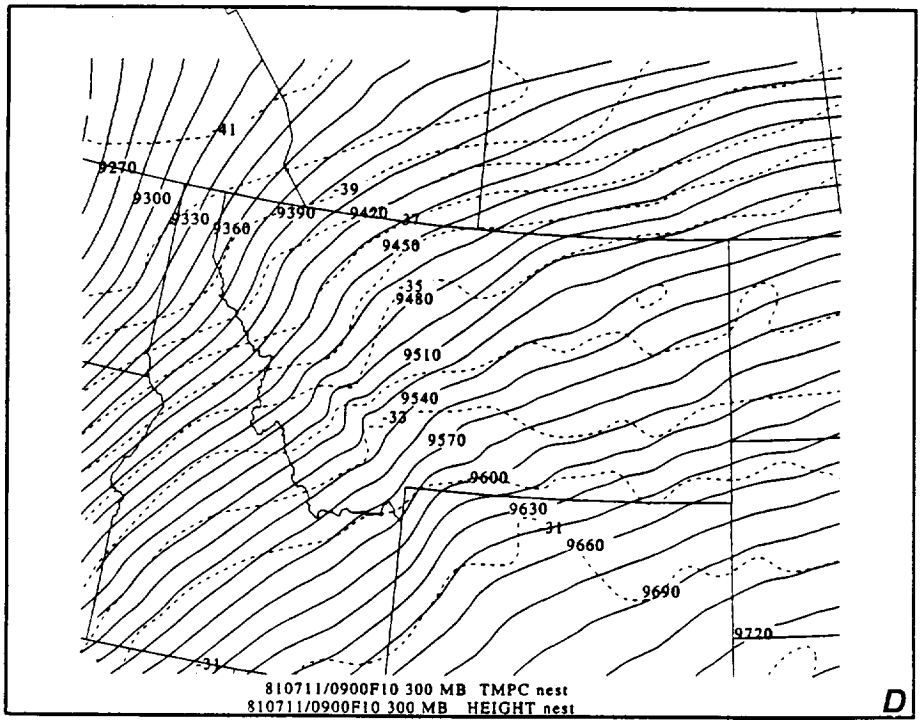

810711/0900F10 300 MB TMPC nest
810711/0900F10 300 MB HEIGHT nest

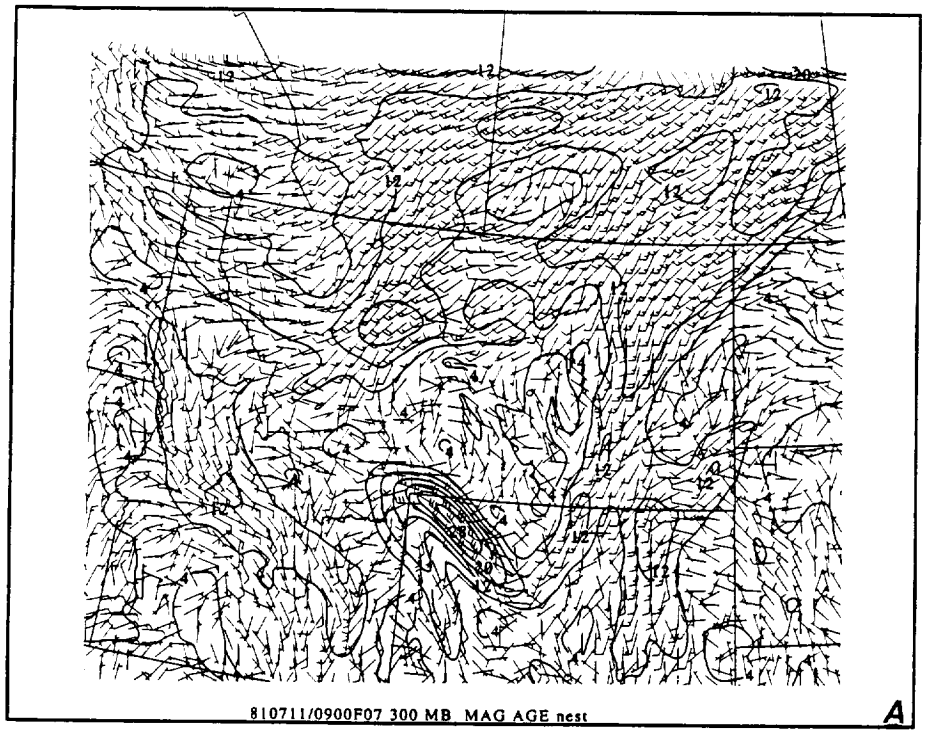

810711/0900F07 300 MB MAG AGE nest

A

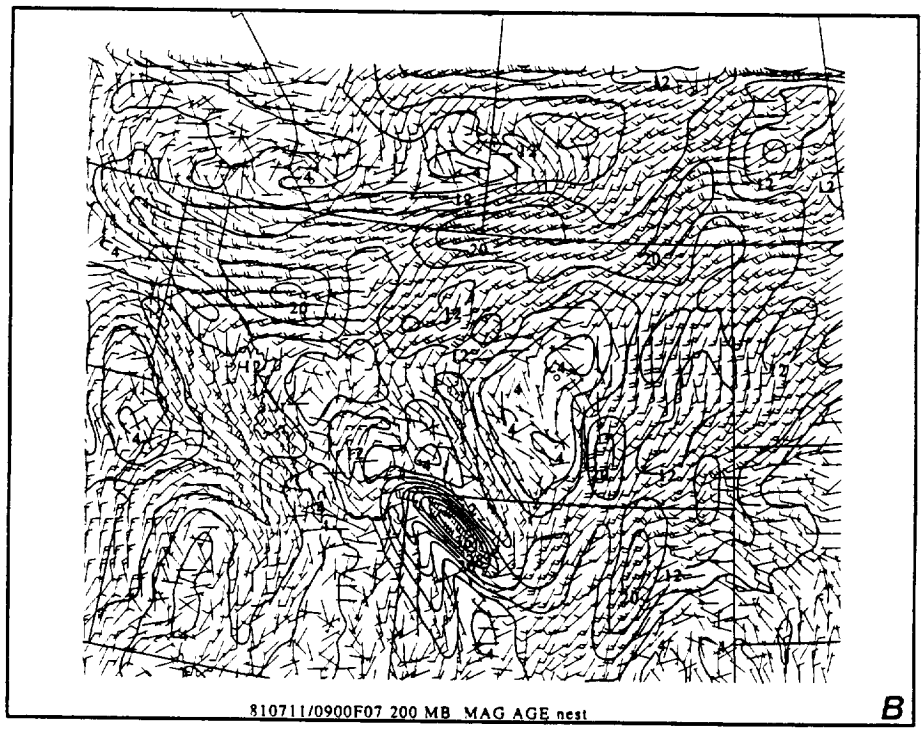

810711/0900F07 200 MB MAG AGE nest

B

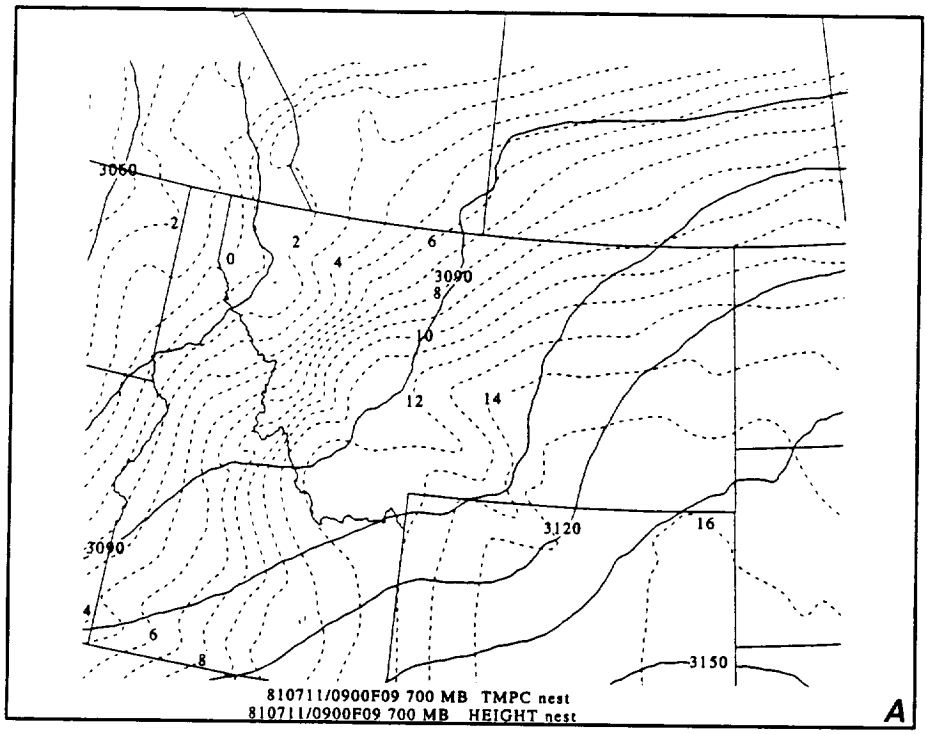
3060
-2
0
2
4
6
3090
8
10
12
14
3120
16
3090
4
6
8
3150
810711/0900F09 700 MB TMPC nest
810711/0900F09 700 MB HEIGHT nest
A

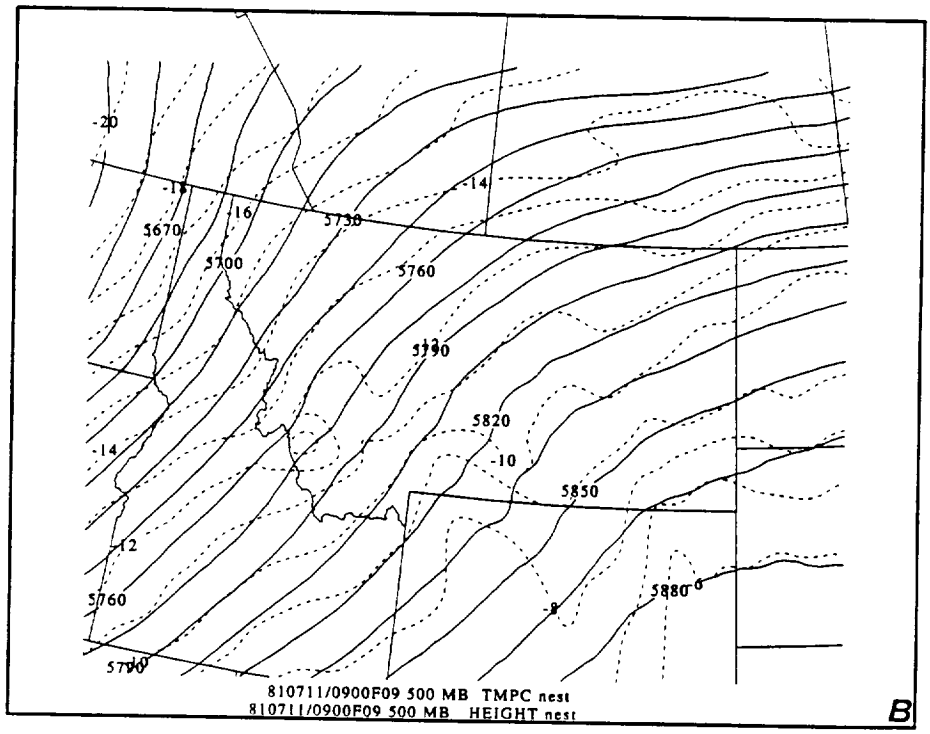
-20
-18
-16
5670
5700
5730
-14
5760
5790
5820
-14
-10
5850
-12
5760
5880
-8
810711/0900F09 500 MB TMPC nest
810711/0900F09 500 MB HEIGHT nest
B

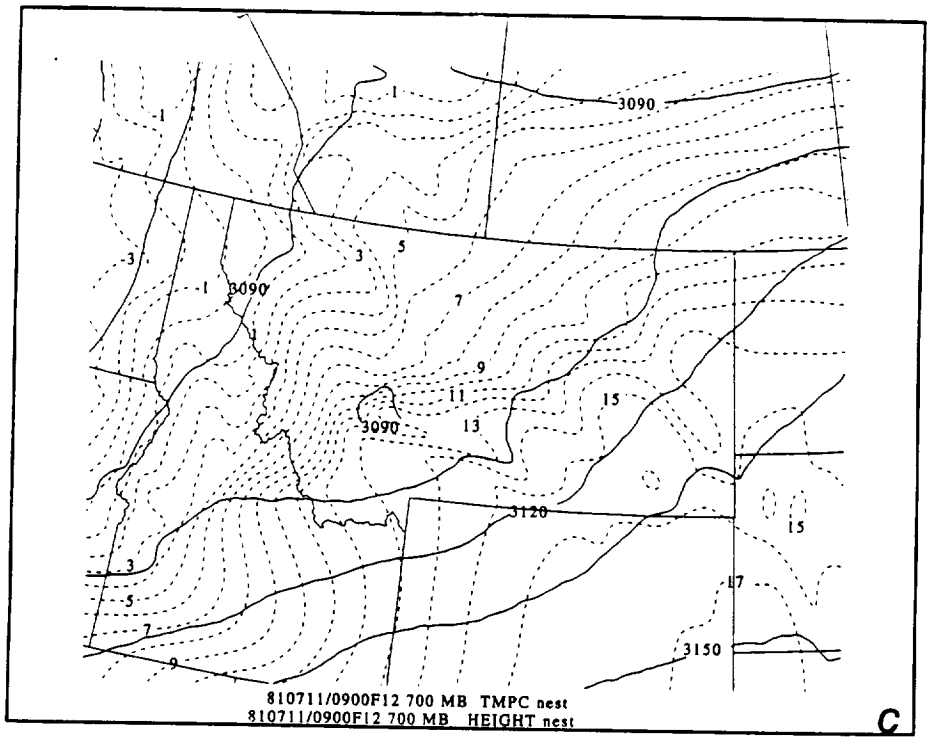
3090
3090
3090
3120
3150
810711/0900F12 700 MB TMPC nest
810711/0900F12 700 MB HEIGHT nest
C

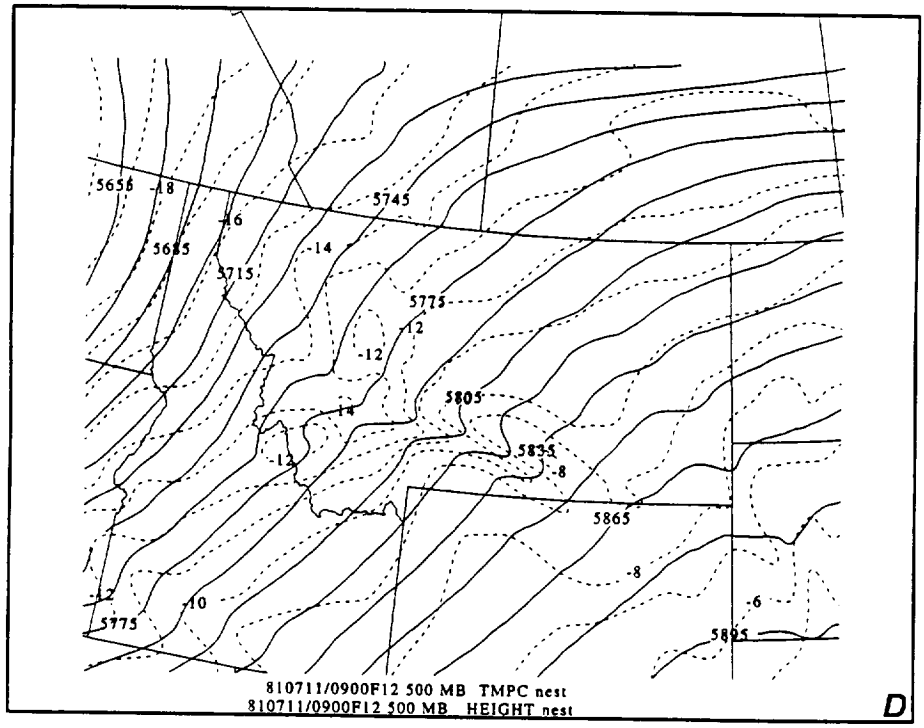
5745
5775
5805
5835
5865
5895
810711/0900F12 500 MB TMPC nest
810711/0900F12 500 MB HEIGHT nest
D

810711/0900F06 OMEGA nest
810711/0900F06 THETA nest

A

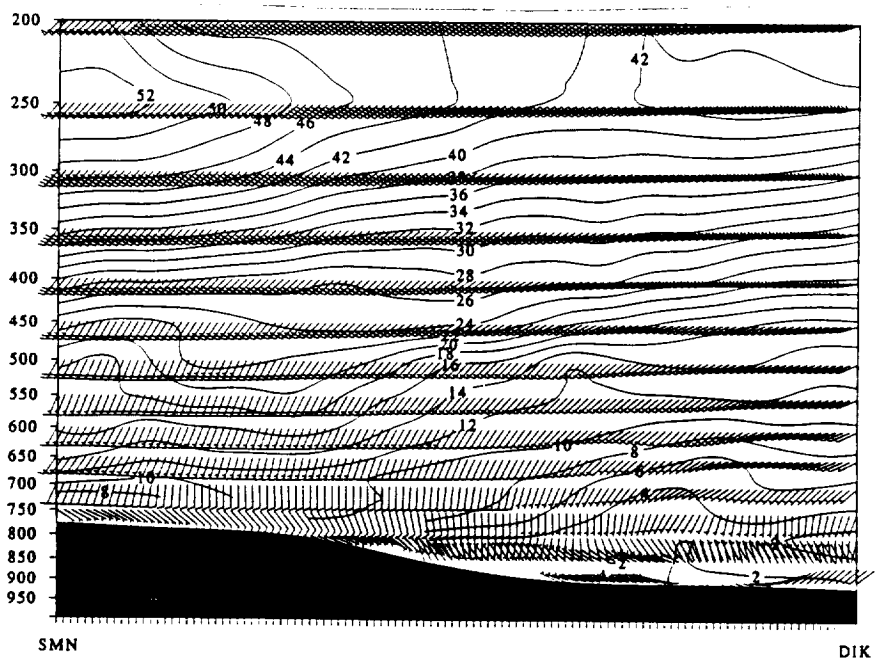

810711/0900F06 MAGOBS nest

B

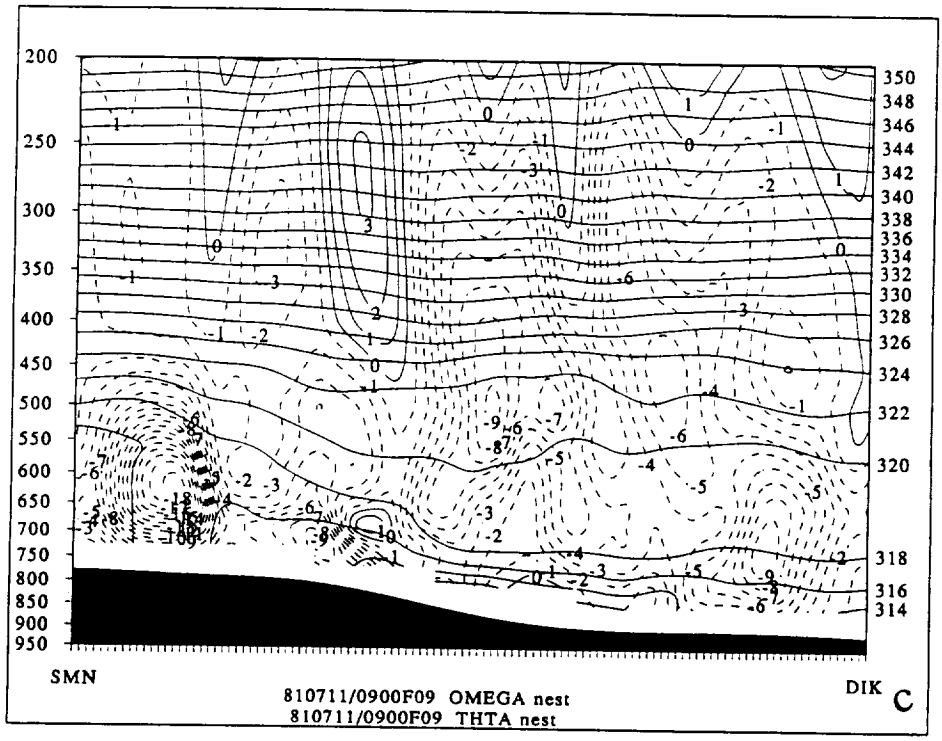
SMN
DIK
810711/0900F09 OMEGA nest
810711/0900F09 THTA nest
C

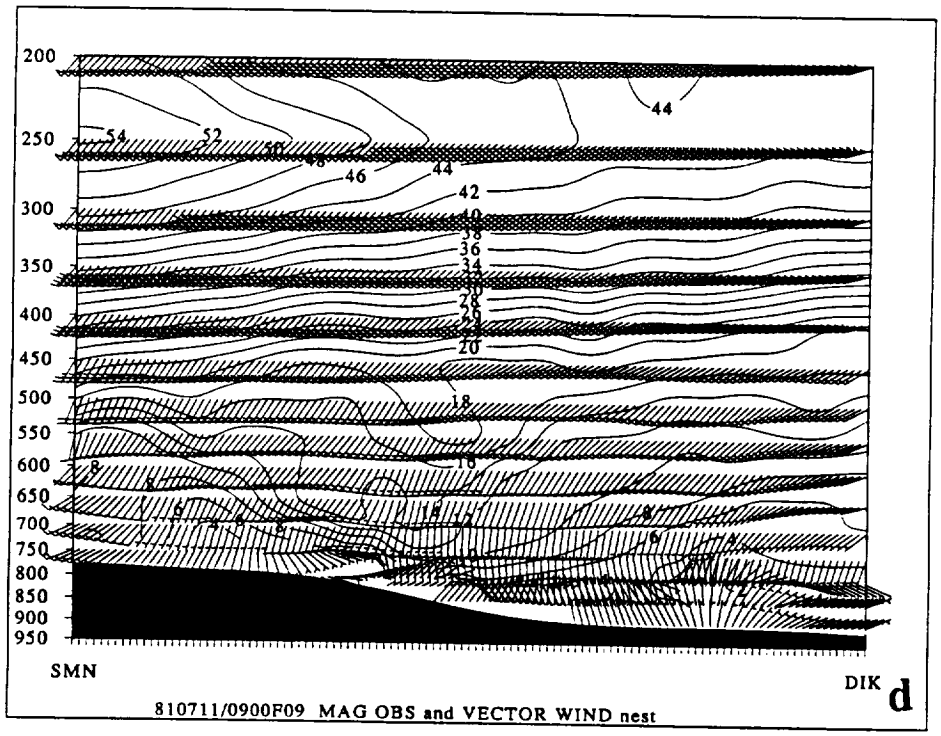
SMN
DIK
810711/0900F09 MAG OBS and VECTOR WIND nest
d

C-2

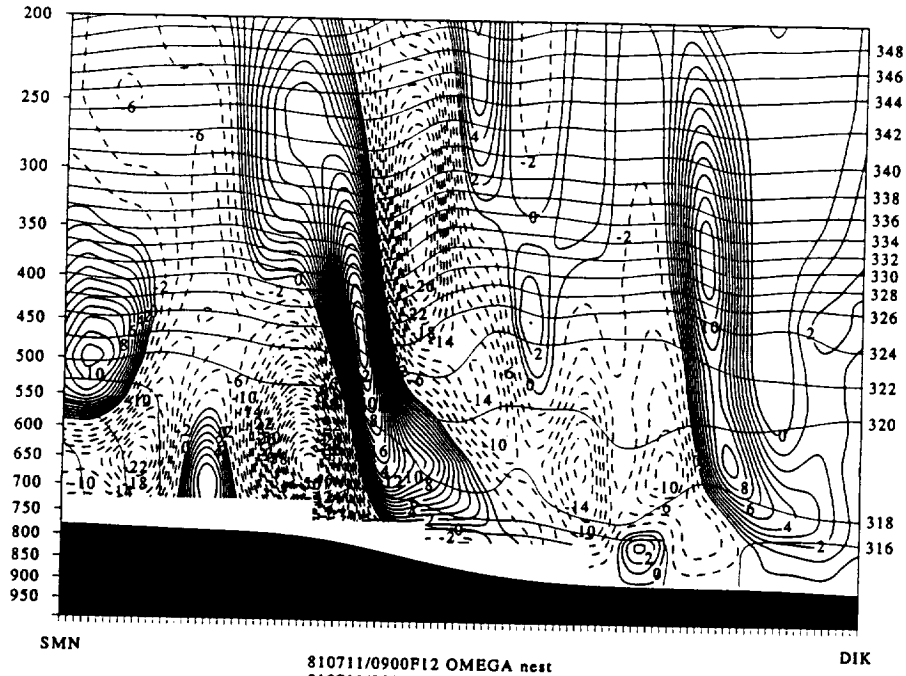

810711/0900F12 OMEGA nest
810711/0900F12 THETA nest

E

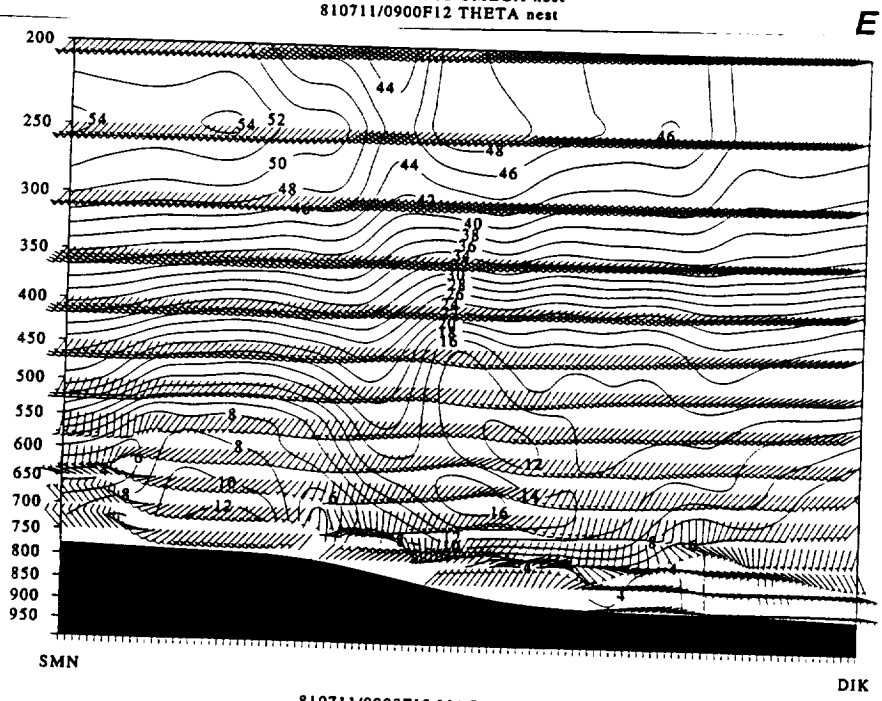

810711/0900F12 MAGOBS nest

F

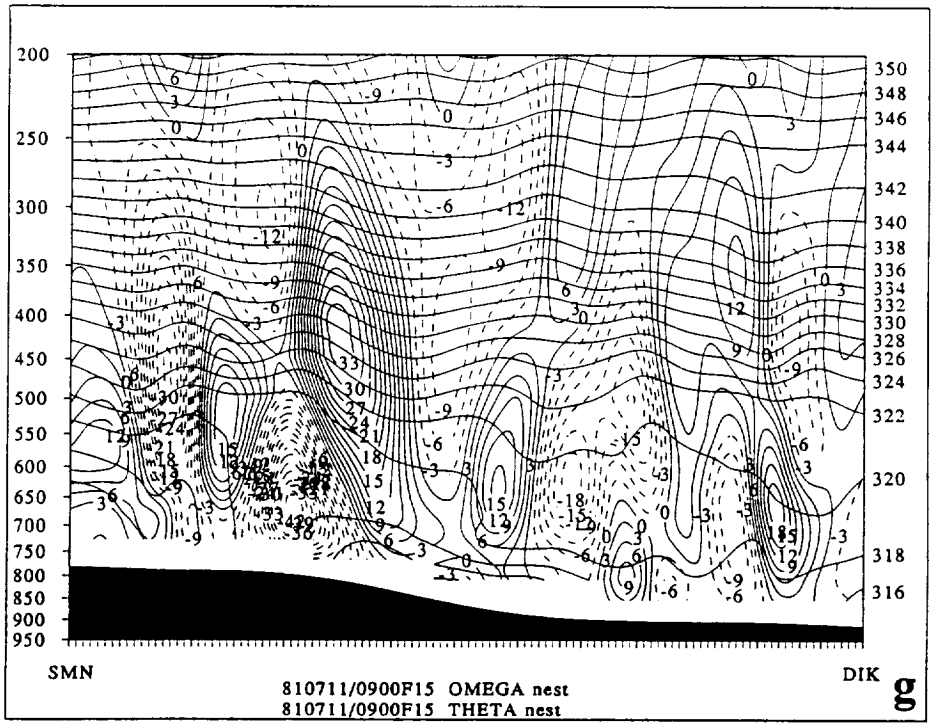
SMN
DIK
810711/0900F15 OMEGA nest
810711/0900F15 THETA nest
g

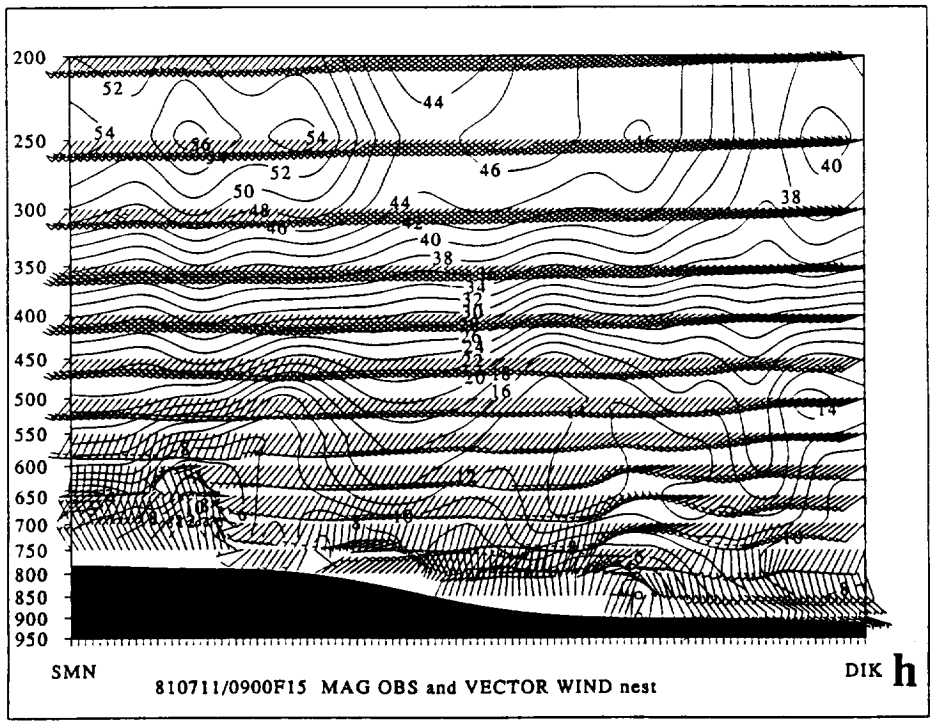
SMN
DIK
810711/0900F15 MAG OBS and VECTOR WIND nest
h

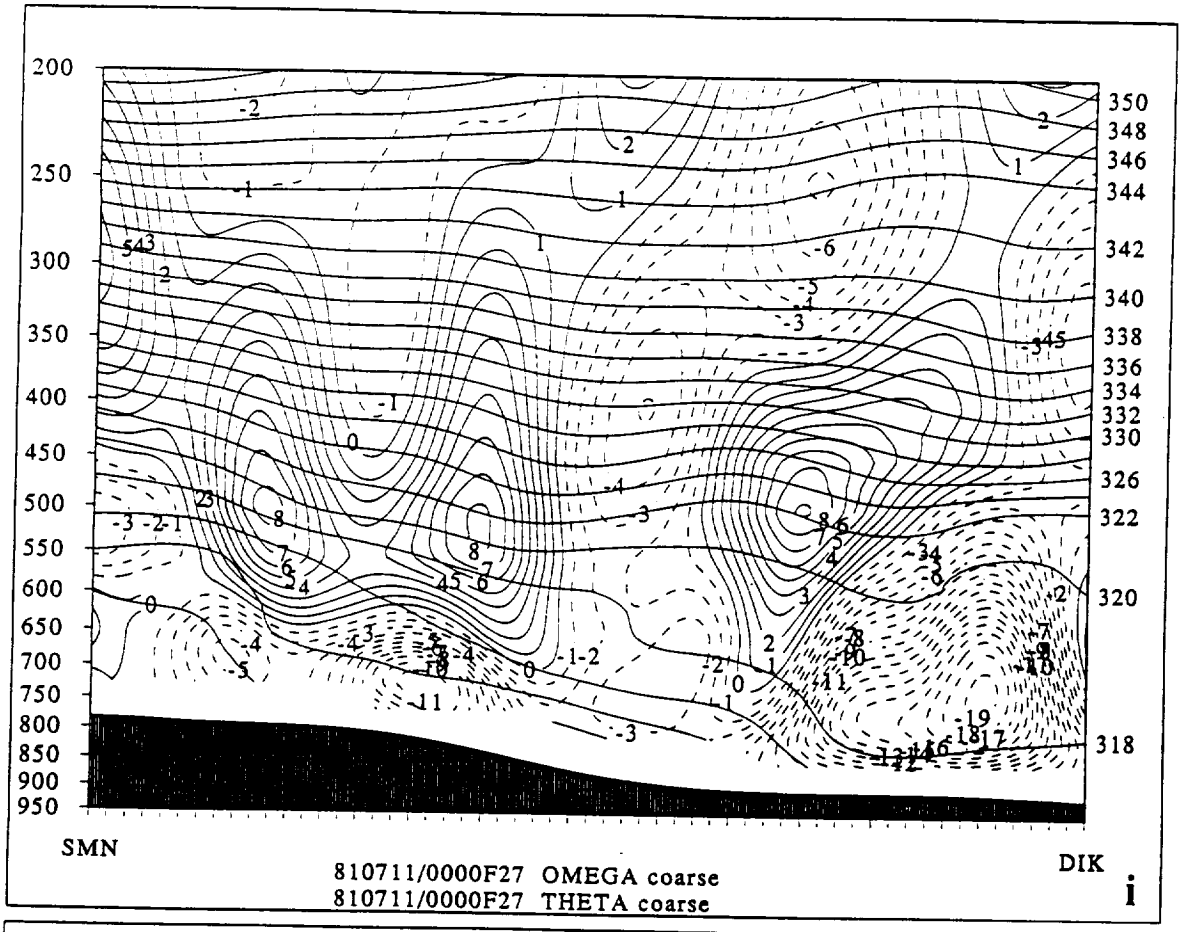
SMN
DIK
810711/0000F27 OMEGA coarse
810711/0000F27 THETA coarse
i

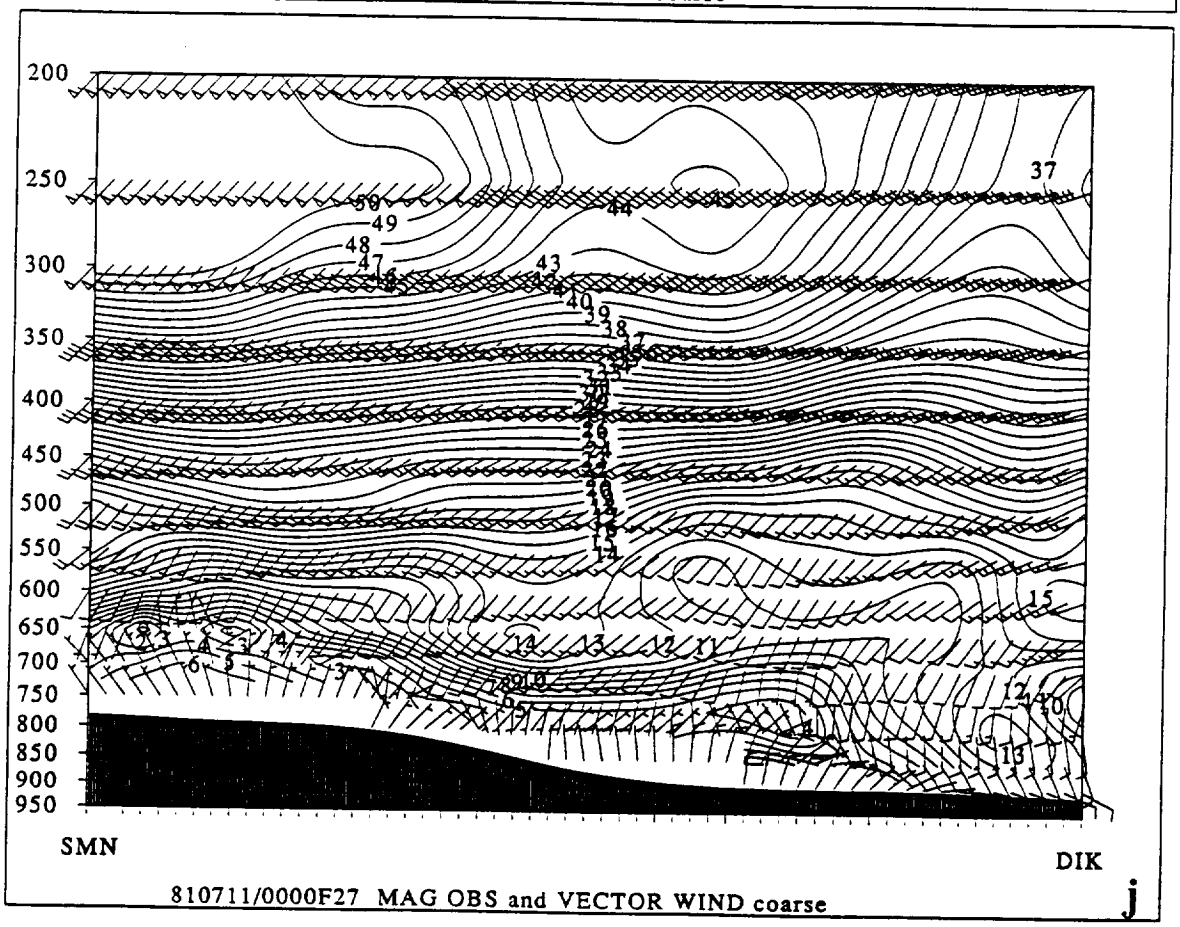
SMN
DIK
810711/0000F27 MAG OBS and VECTOR WIND coarse
j

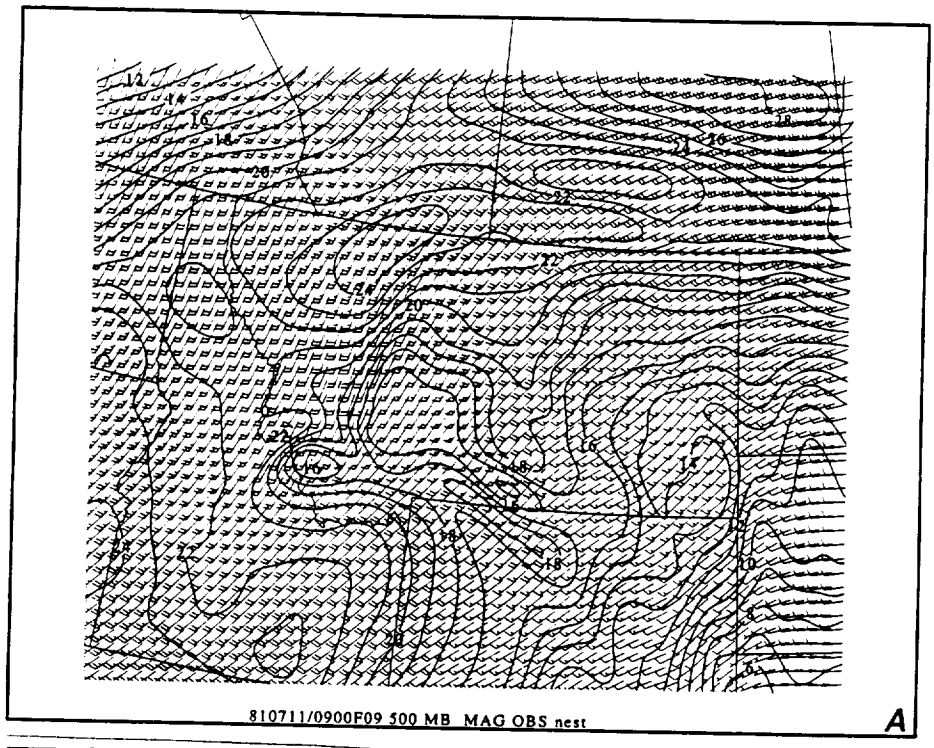
810711/0900F09 500 MB MAG OBS nest
A

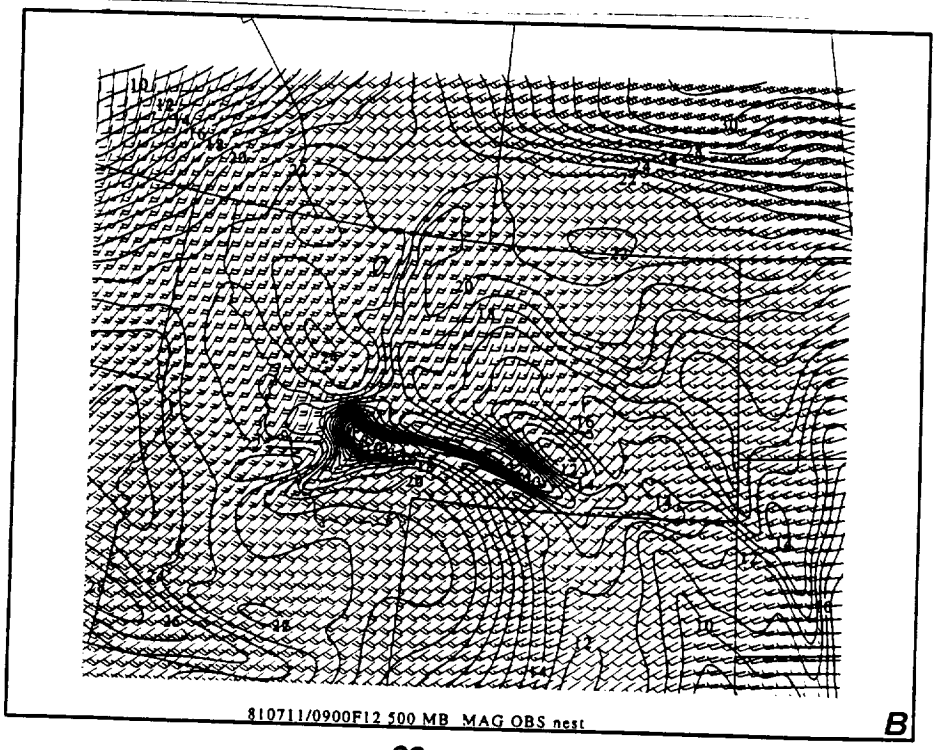
810711/0900F12 500 MB MAG OBS nest
B

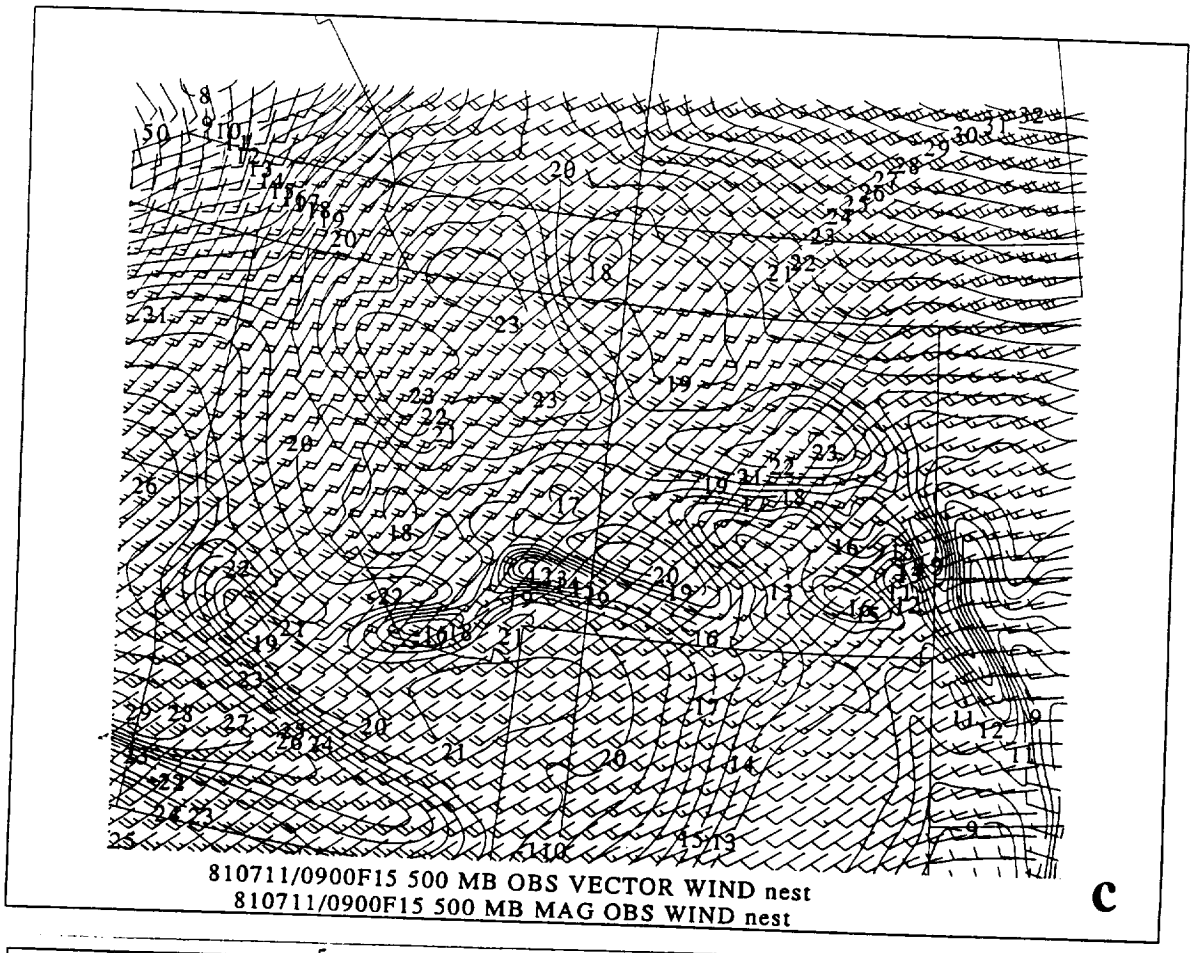

810711/0900F15 500 MB OBS VECTOR WIND nest
810711/0900F15 500 MB MAG OBS WIND nest

c

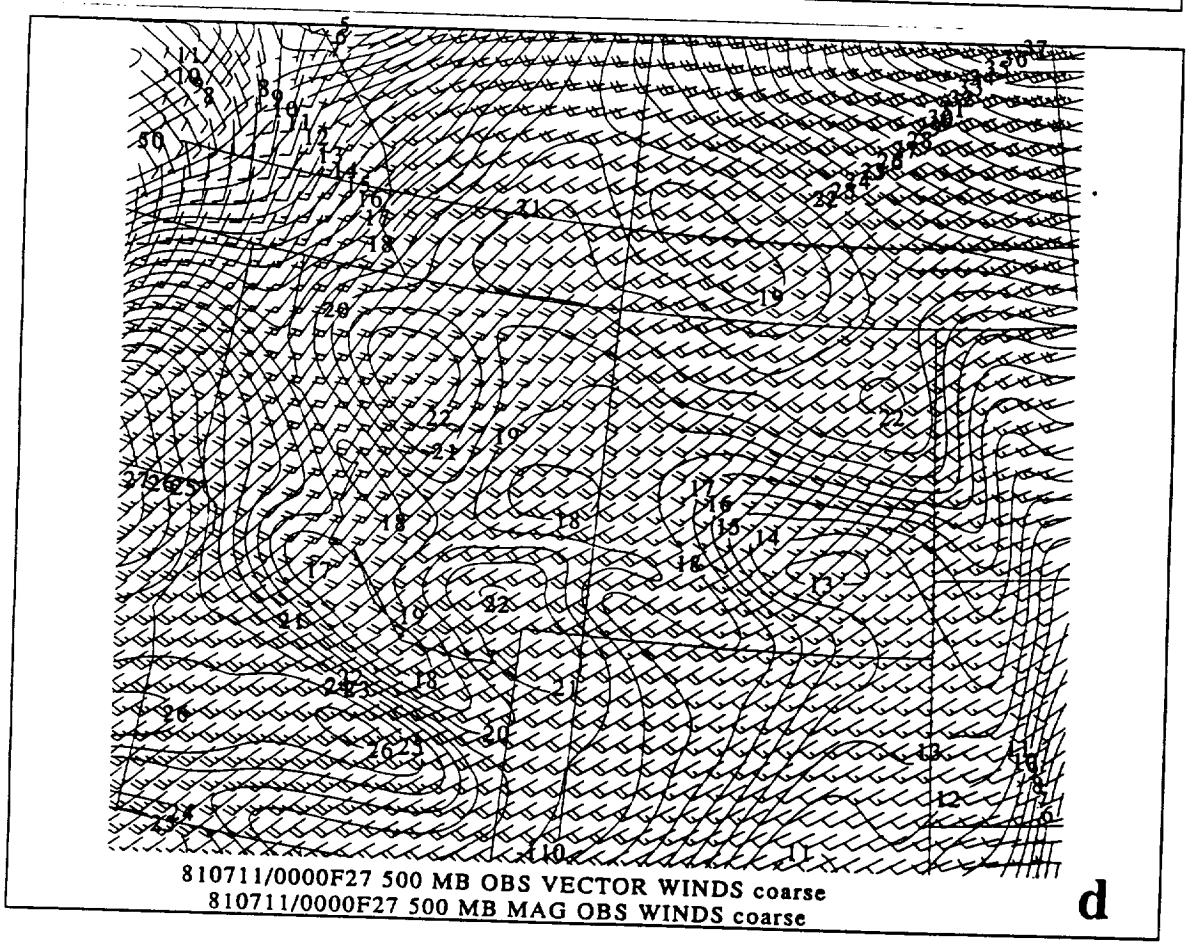

810711/0000F27 500 MB OBS VECTOR WINDS coarse
810711/0000F27 500 MB MAG OBS WINDS coarse

d

810711/0900F09 700 MB OMEGA nest

A

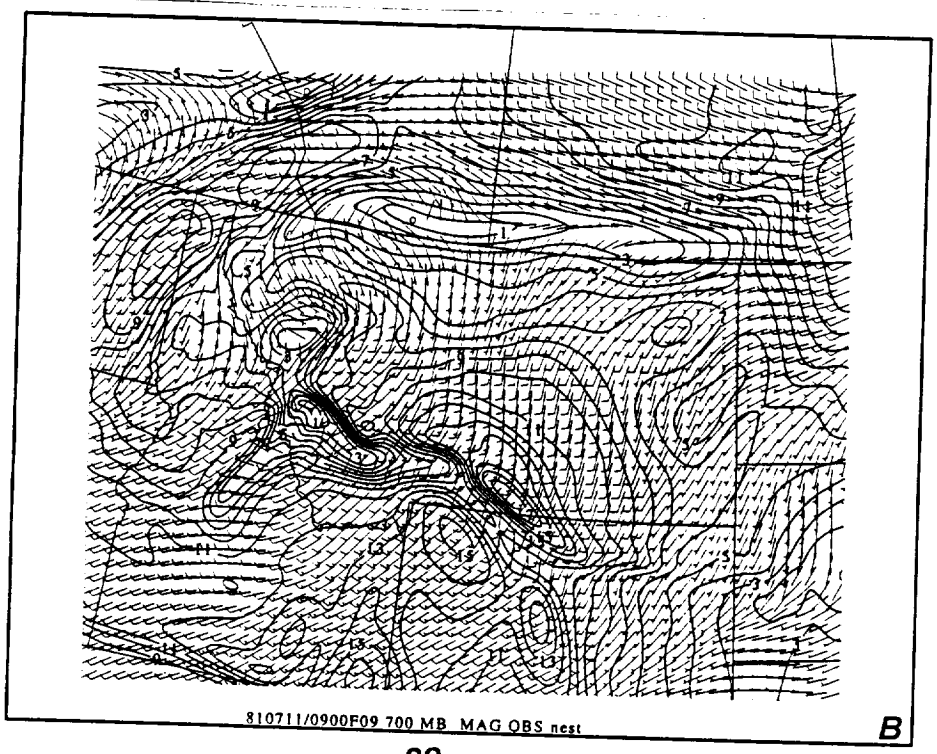

810711/0900F09 700 MB MAG OBS nest

B

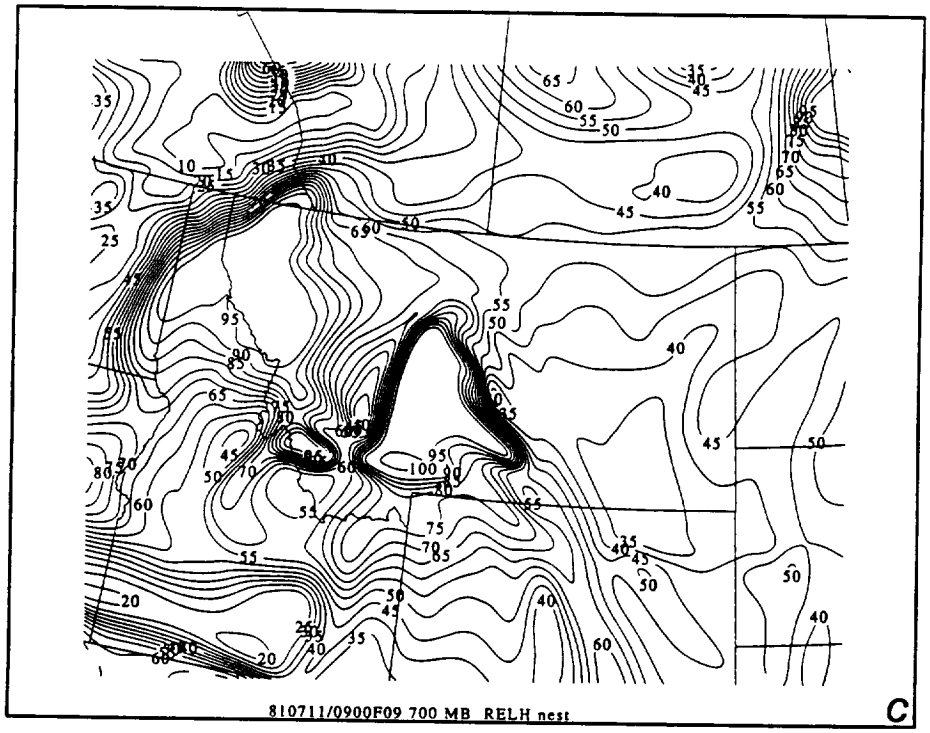

810711/0900F09 700 MB RELH nest

C

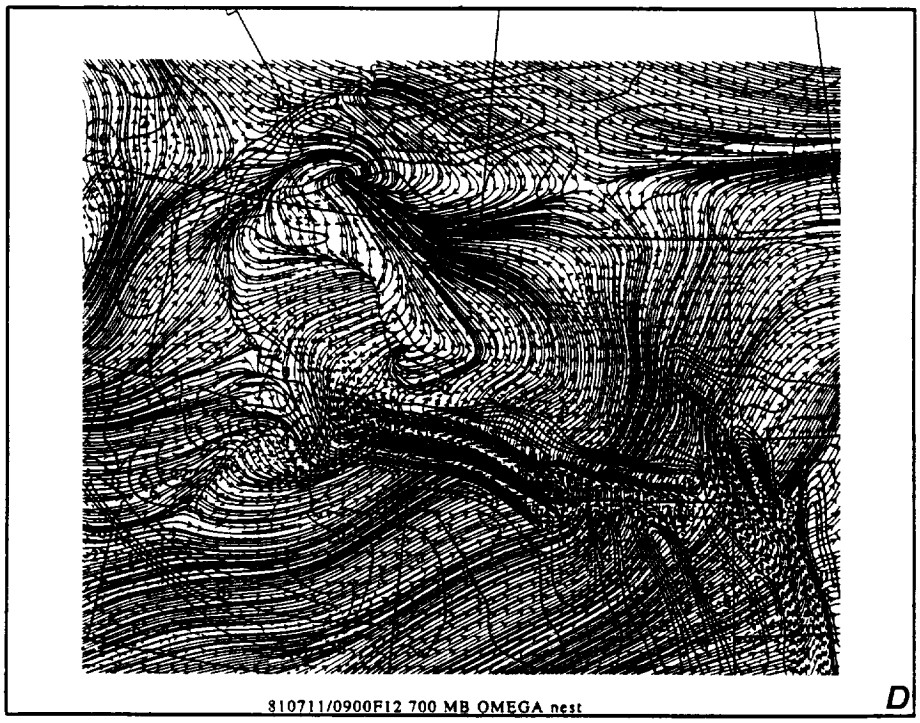

810711/0900F12 700 MB OMEGA nest

D

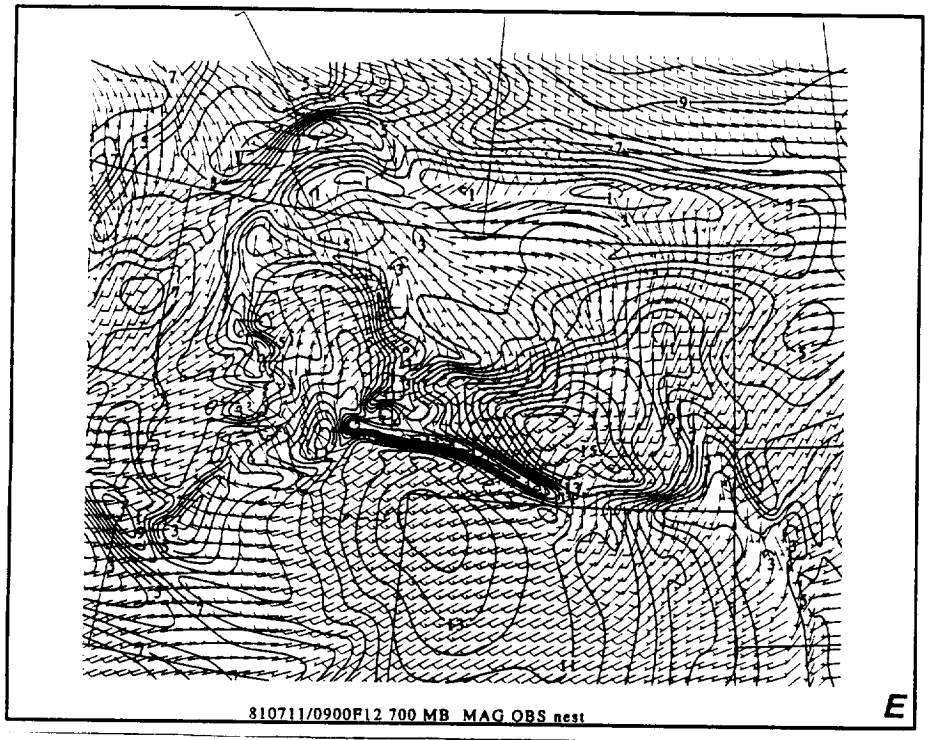

810711/0900F12 700 MB MAG OBS nest

E

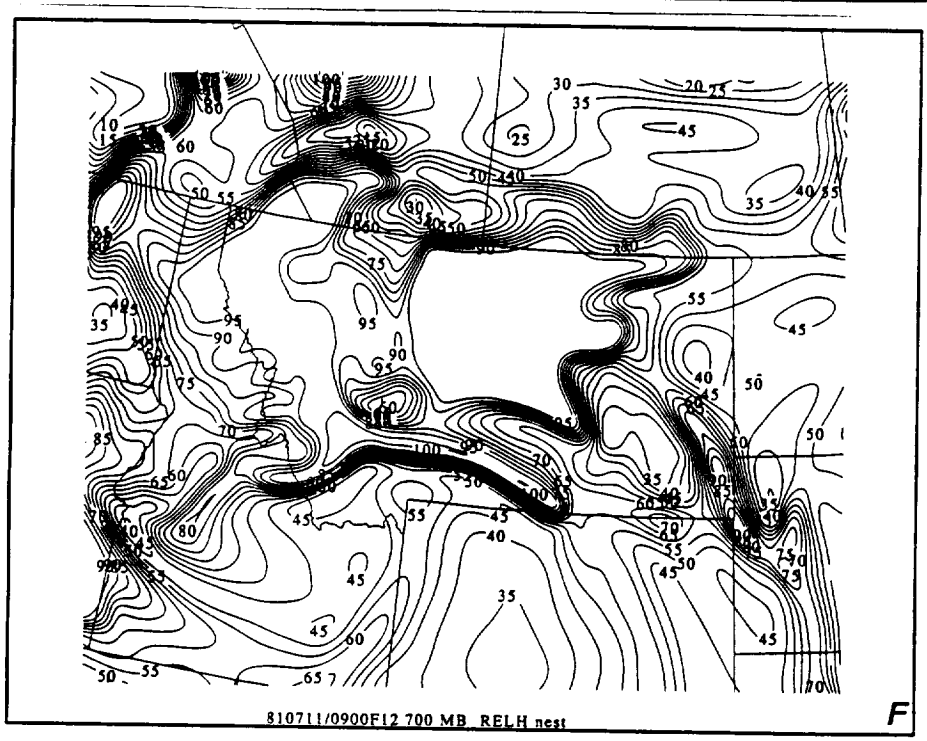

810711/0900F12 700 MB RELH nest

F

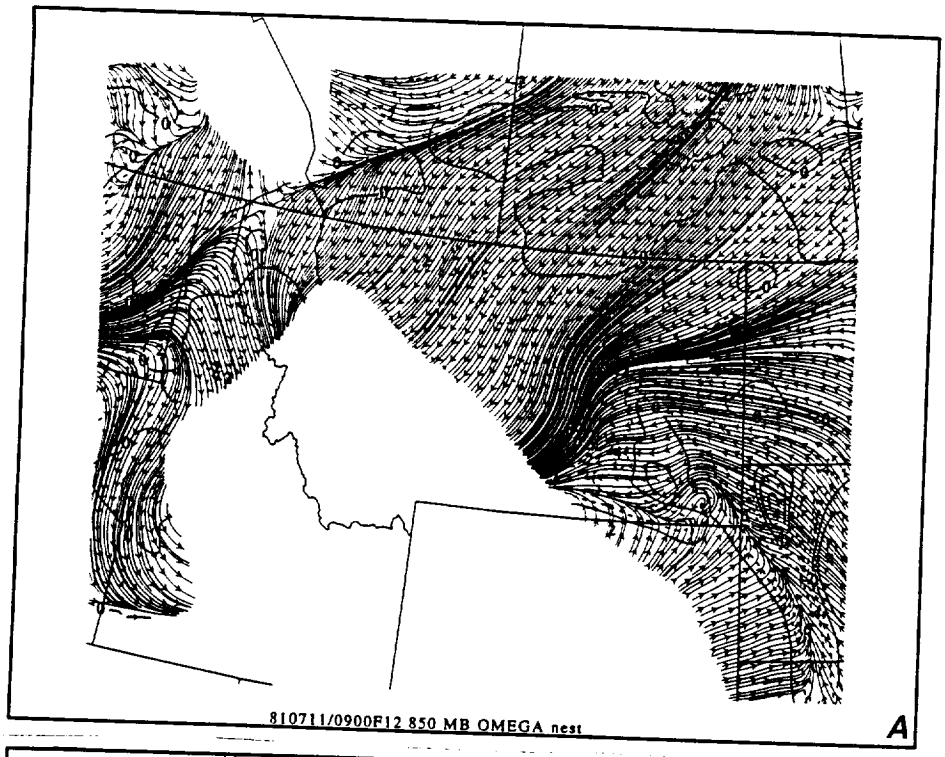
810711/0900F12 850 MB OMEGA nest
A

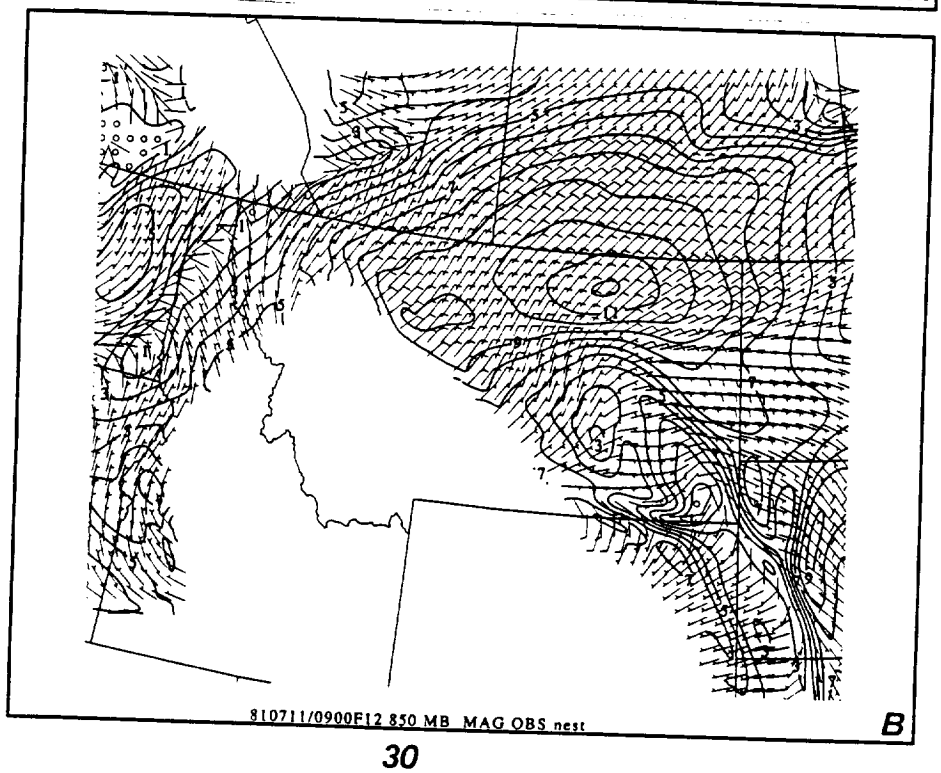
810711/0900F12 850 MB MAG OBS nest
B

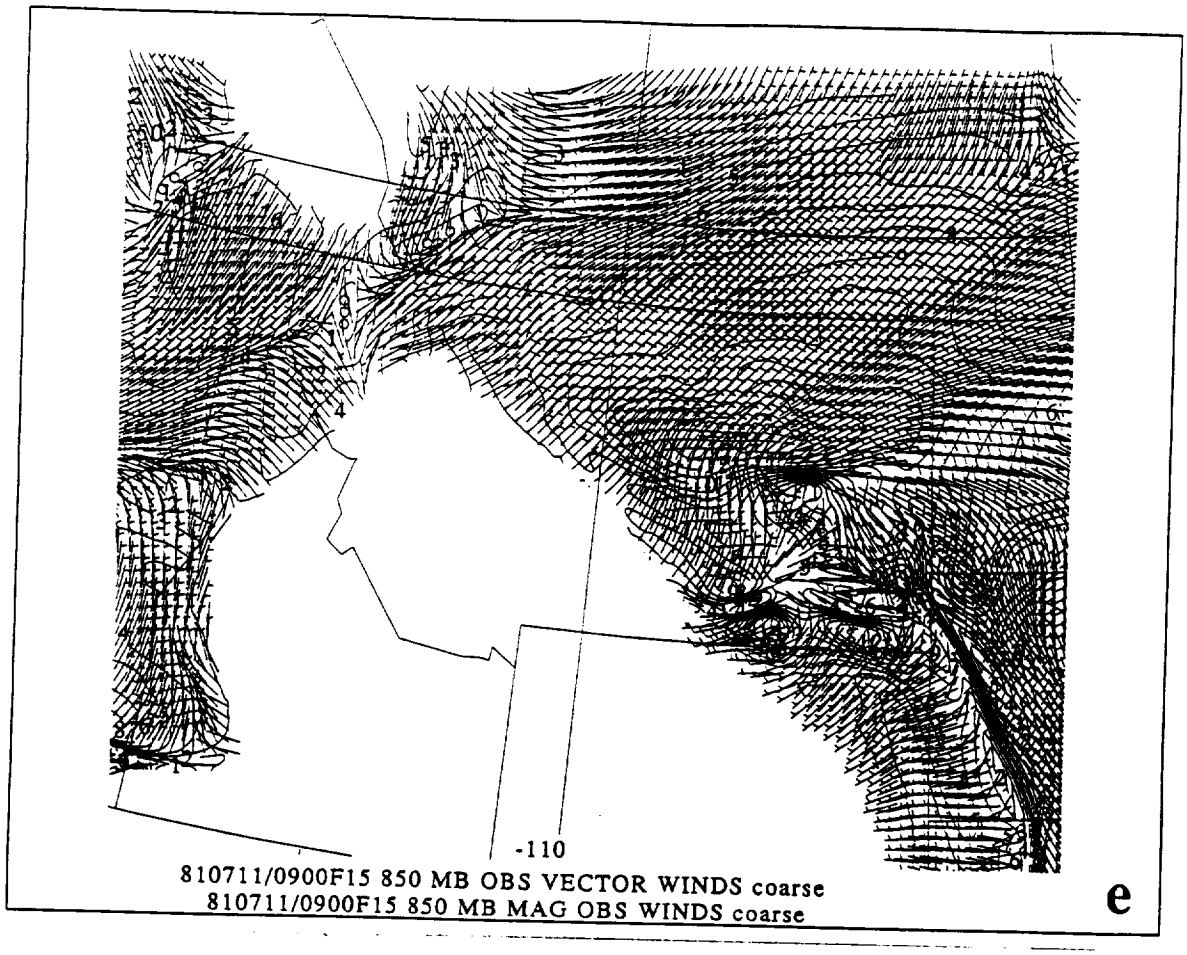

810711/0900F15 850 MB OBS VECTOR WINDS coarse
810711/0900F15 850 MB MAG OBS WINDS coarse

e

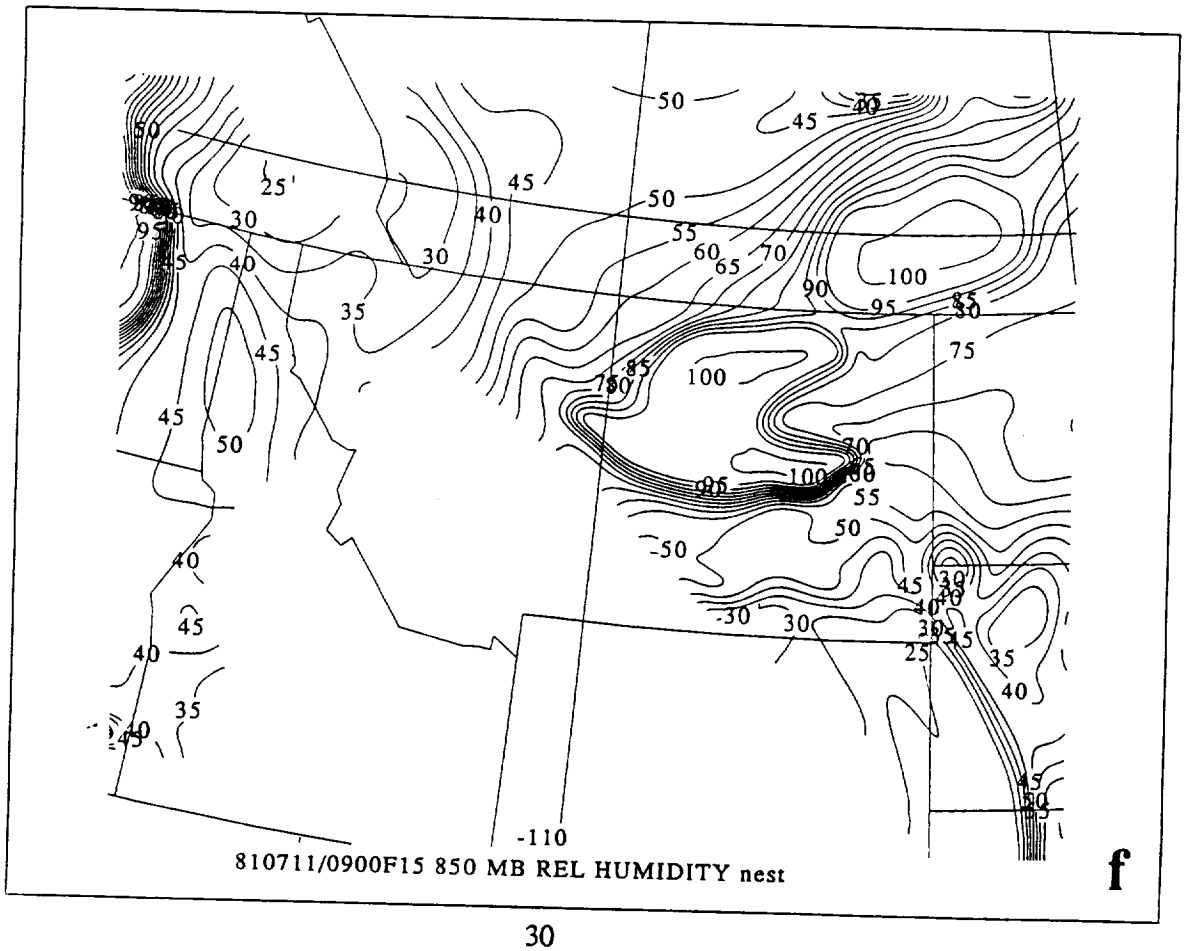

810711/0900F15 850 MB REL HUMIDITY nest

f

810711/0900F15 700 MB OMEGA nest

a

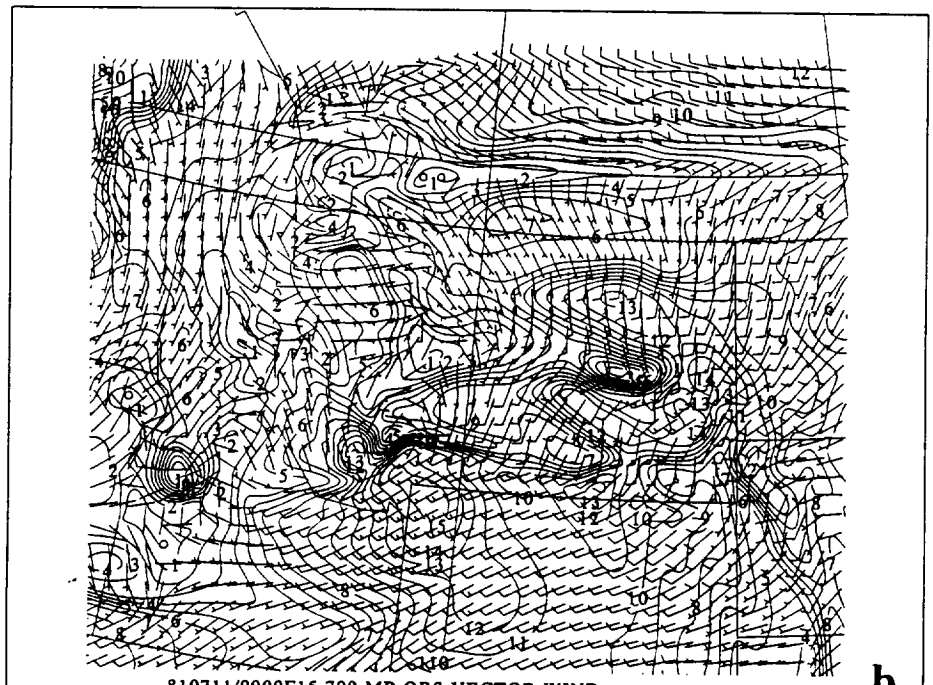

810711/0900F15 700 MB OBS VECTOR WIND nest
810711/0900F15 700 MB MAG OBS WIND nest

b

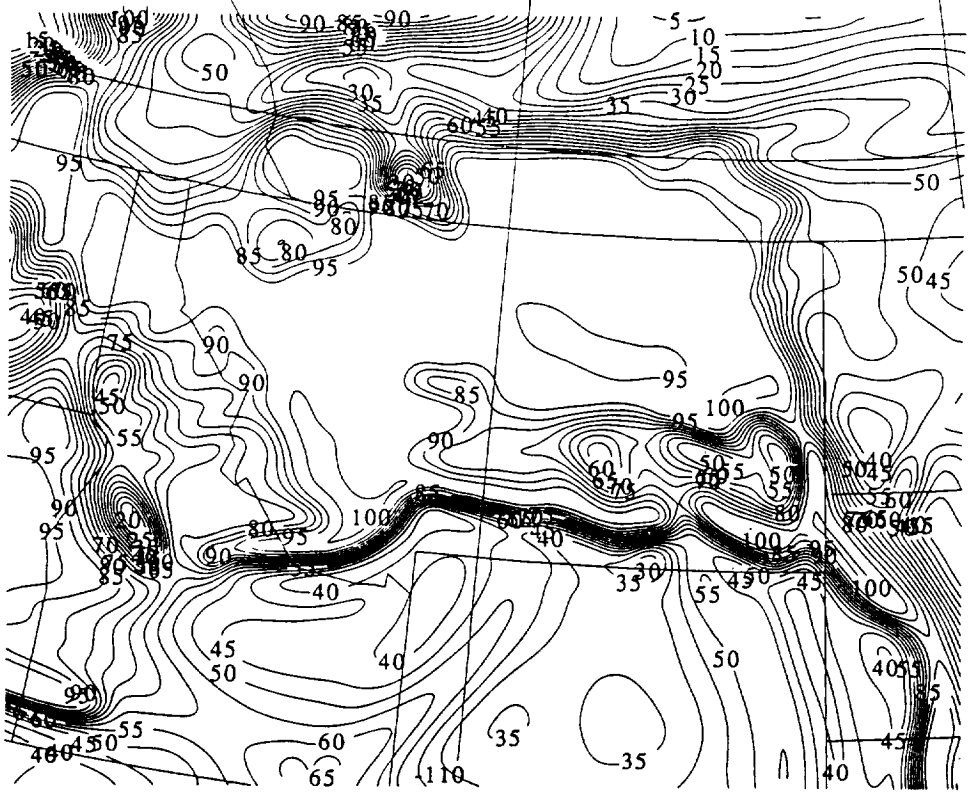

810711/0900F15 700 MB REL HUMIDITY nest

c

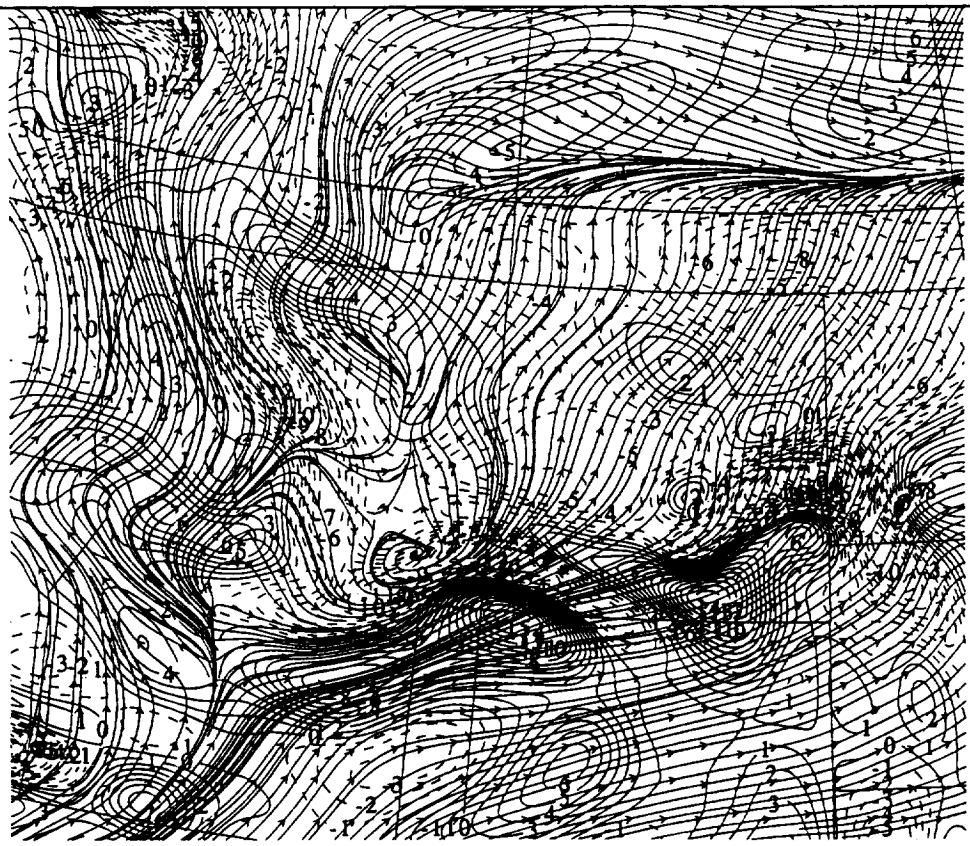

810711/0000F27 700 MB OMEGA coarse

d

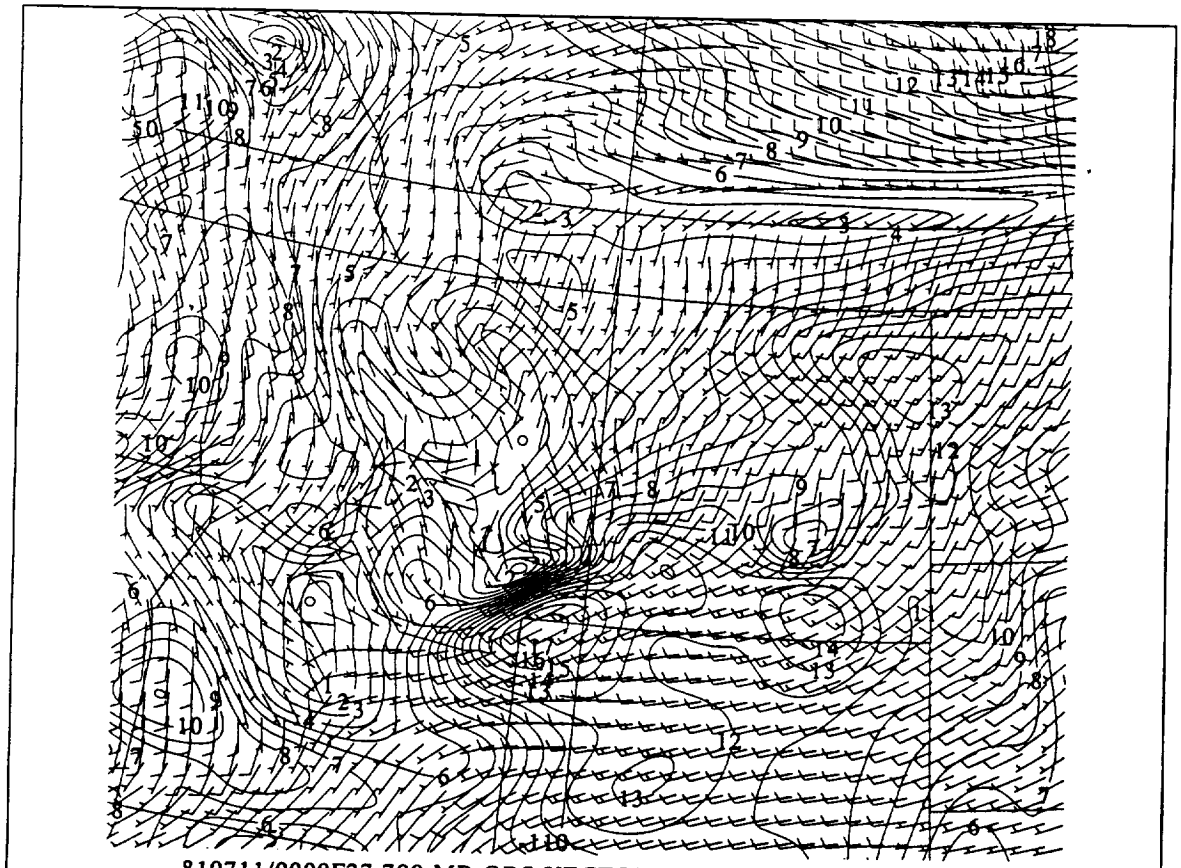

810711/0000F27 700 MB OBS VECTOR WINDS coarse
810711/0000F27 700 MB MAG OBS WINDS coarse

e

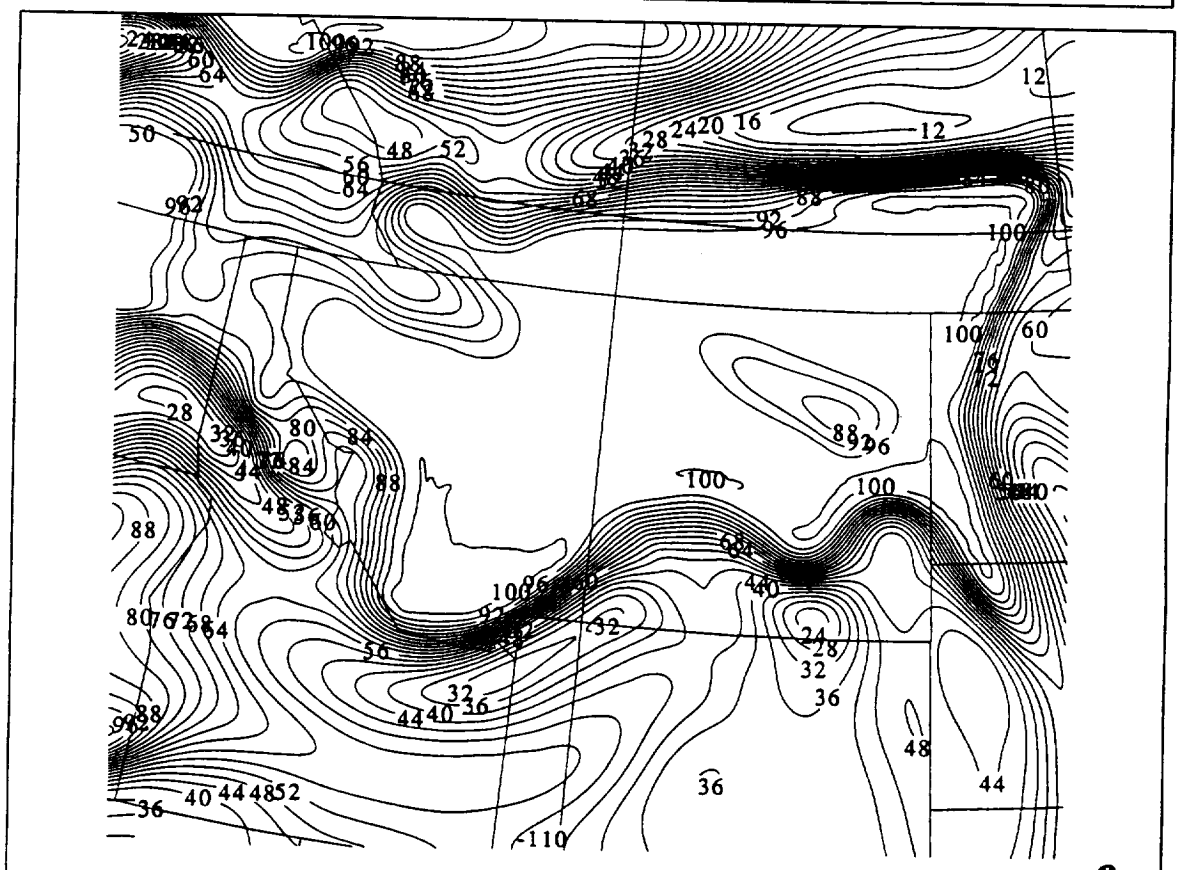

810711/0000F27 700 MB RELH coarse

f

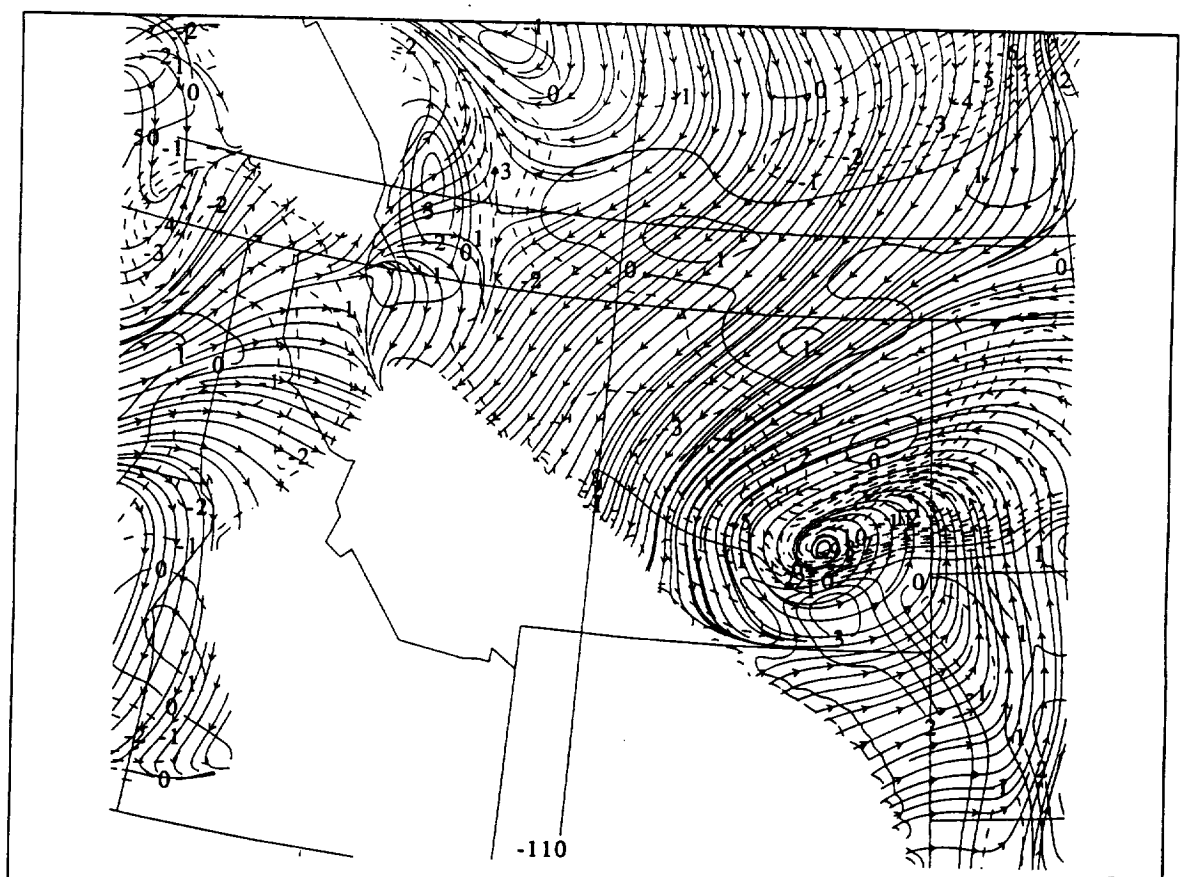

810711/0000F27 850 MB OMEGA coarse

a

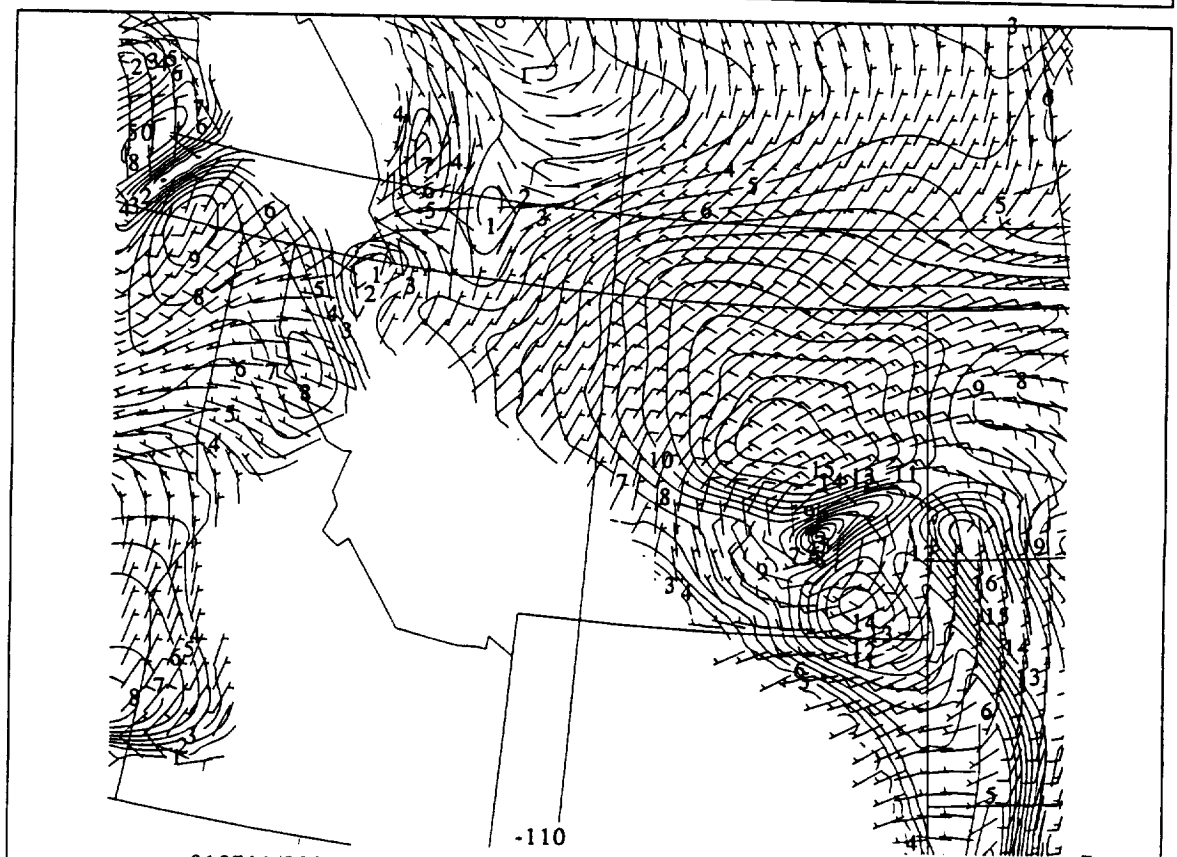

810711/0000F27 850 MB OBS VECTOR WIND coarse
810711/0000F27 850 MB MAG OBS WINDS coarse

b

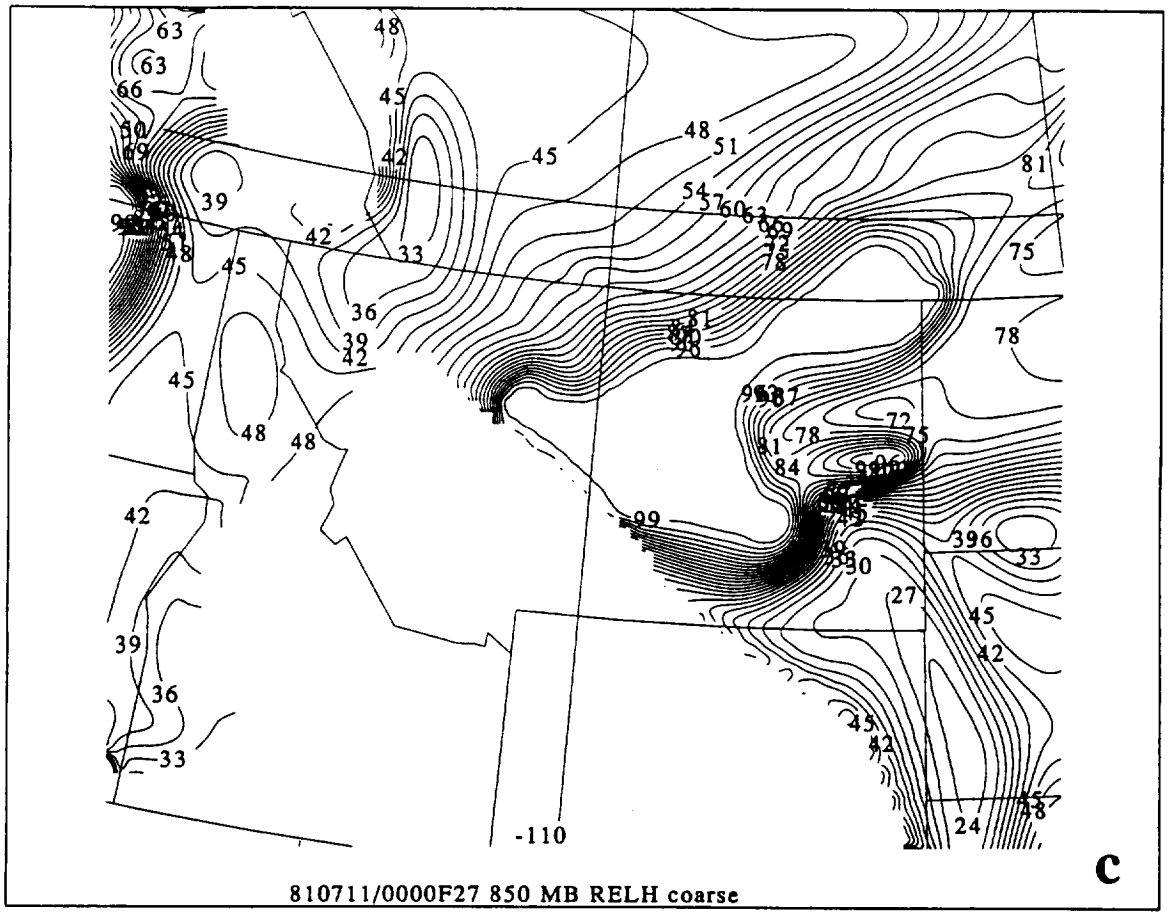

810711/0000F27 850 MB RELH coarse

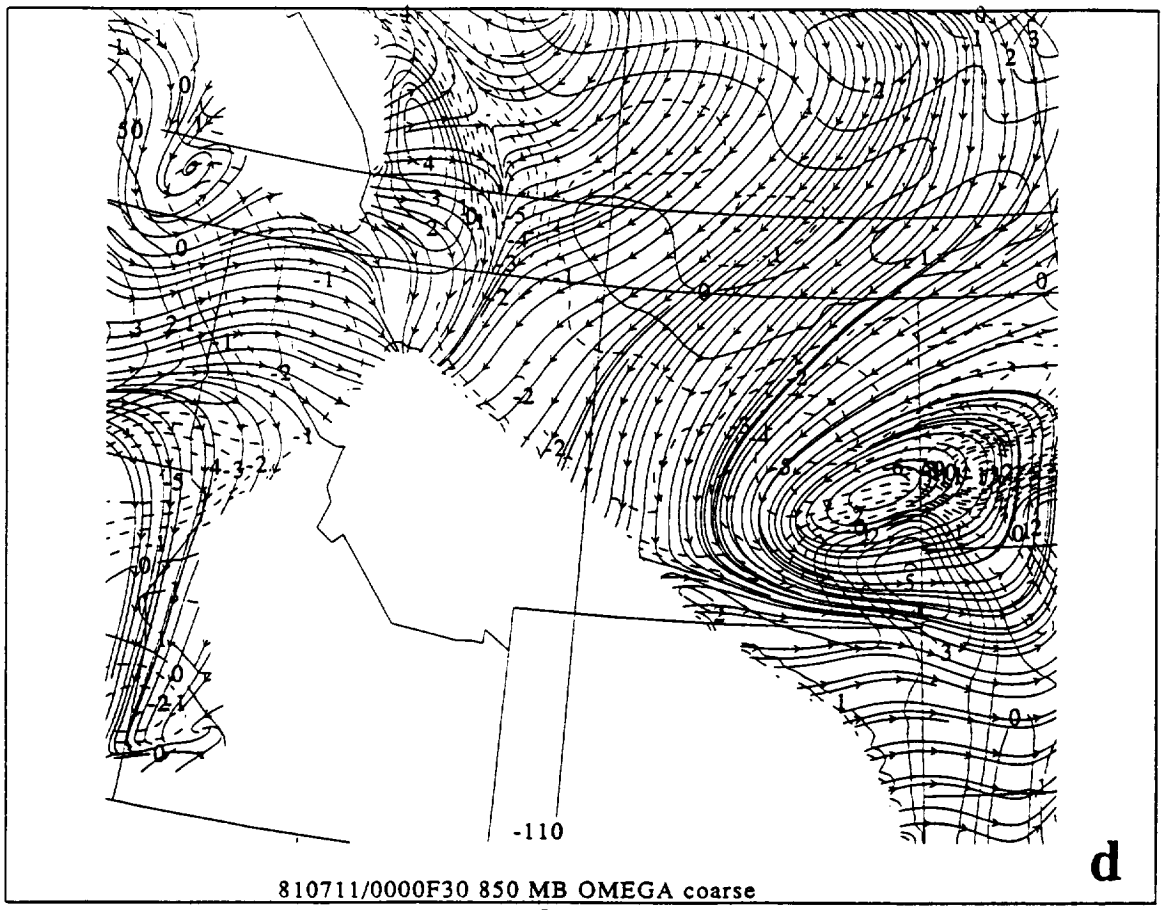

810711/0000F30 850 MB OMEGA coarse

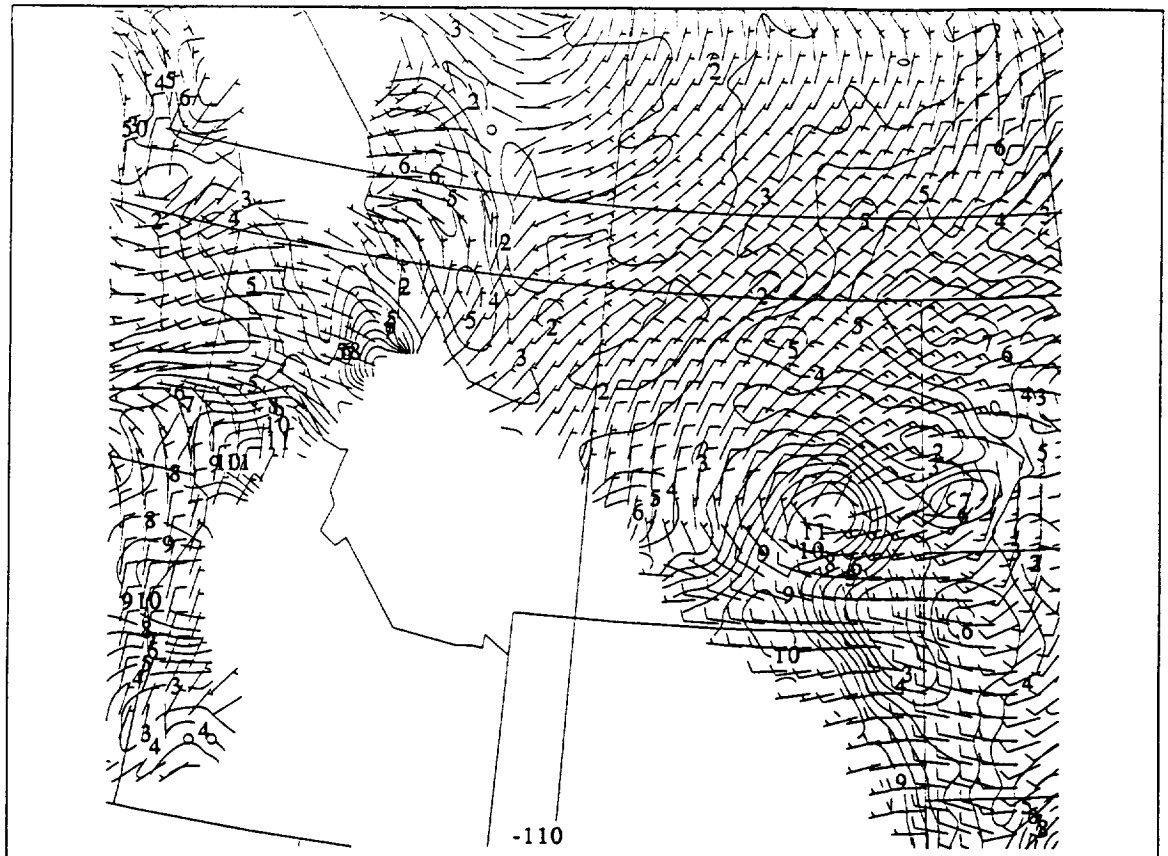

810711/0000F30 850 MB OBS VECTOR WINDS coarse
810711/0000F30 850 MB MAG OBS WINDS coarse

e

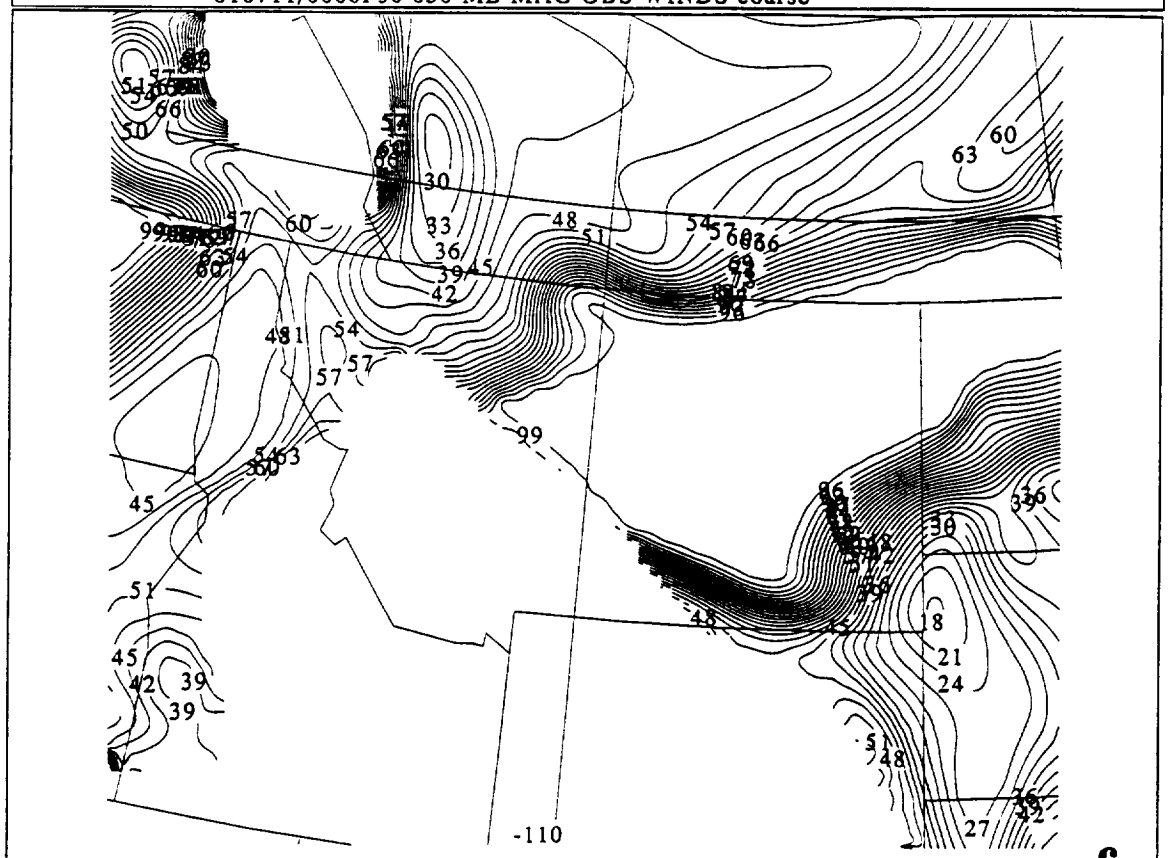

810711/0000F30 850 MB RELH coarse

f

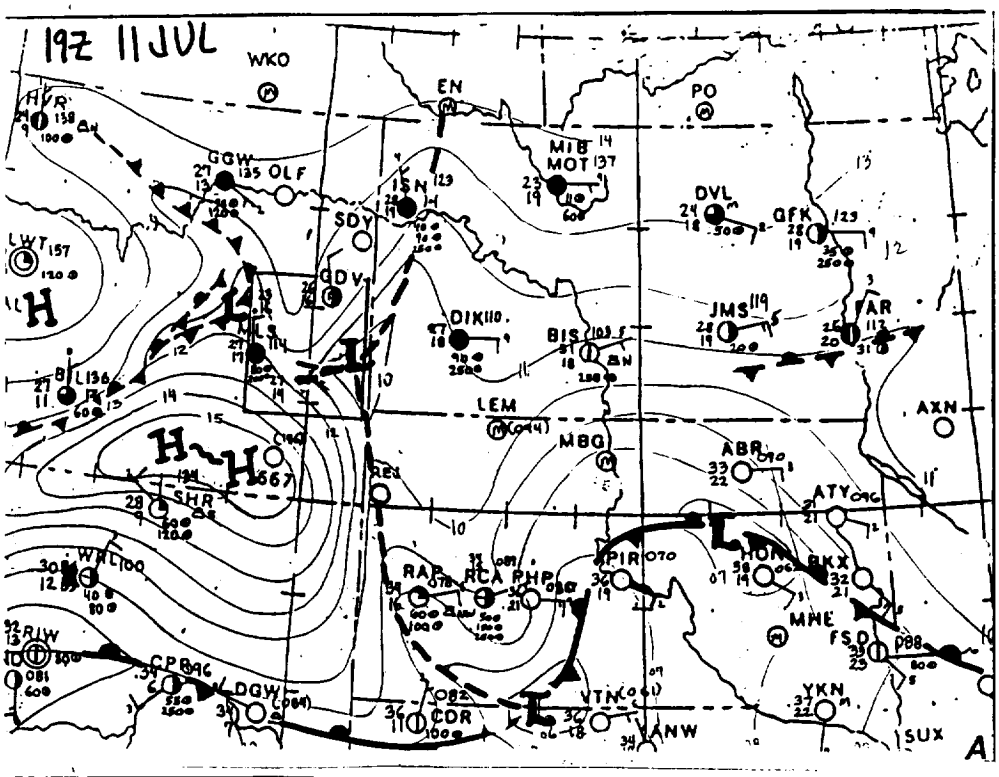
19Z 11 JUL
WKO
EN
PO
HVR
GGW
OLF
ISN
MIB
MOT
DVL
GFK
SDY
GDV
LWT
DIK
BIS
JMS
FAR
LEM
MBG
AXN
ABR
ATY
SHR
RAP
RCA
PHP
PIR
HON
BKX
MHE
FSD
WRL
RIW
CPR
DGW
CDR
VTN
ANW
YKN
SUX
A

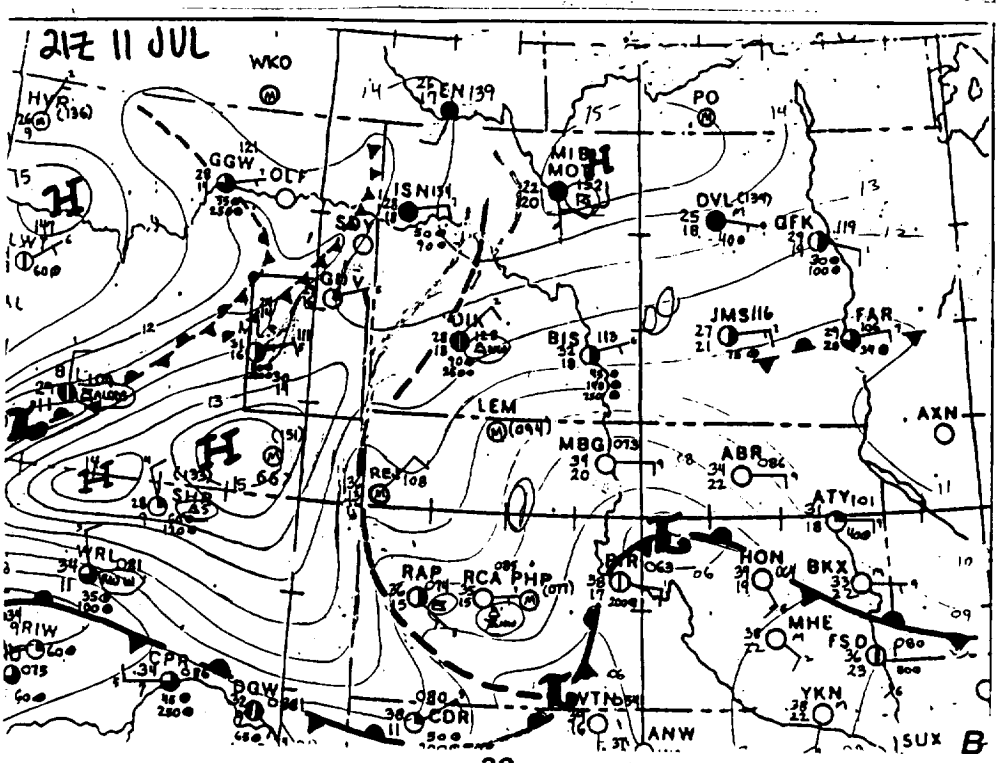
21Z 11 JUL
WKO
EN
PO
HVR
GGW
OLF
ISN
MIB
MOT
DVL
GFK
SDY
GDV
LWT
DIK
BIS
JMS
FAR
LEM
MBG
AXN
ABR
ATY
SHR
RAP
RCA
PHP
PIR
HON
BKX
MHE
FSD
WRL
RIW
CPR
DGW
CDR
VTN
ANW
YKN
SUX
B

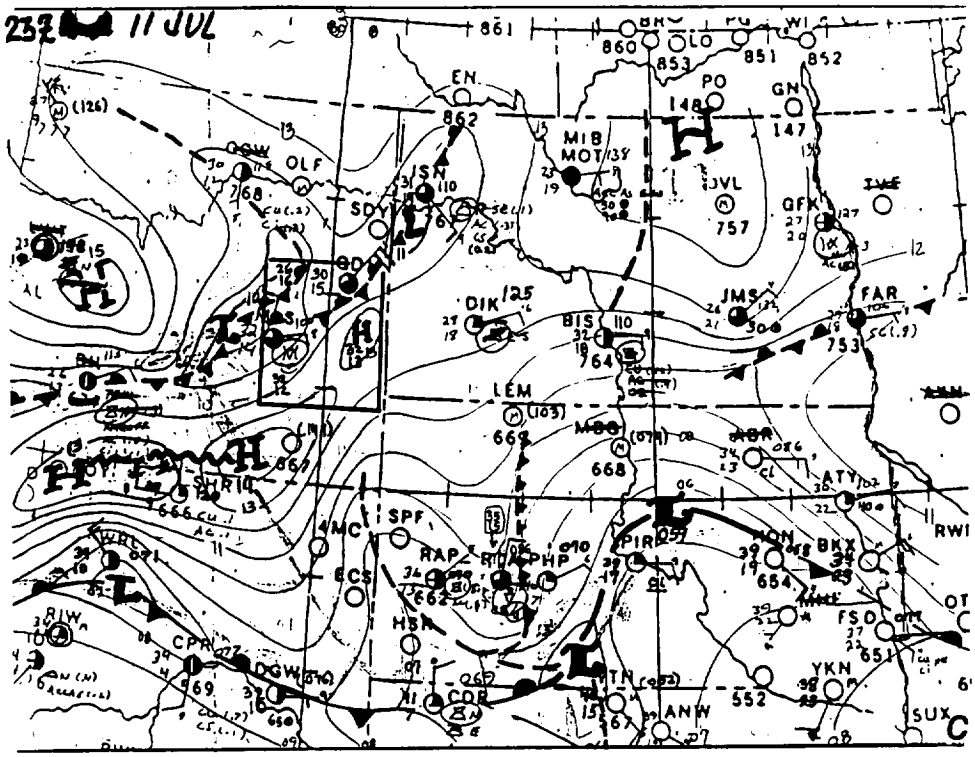
23Z 11 JUL
C

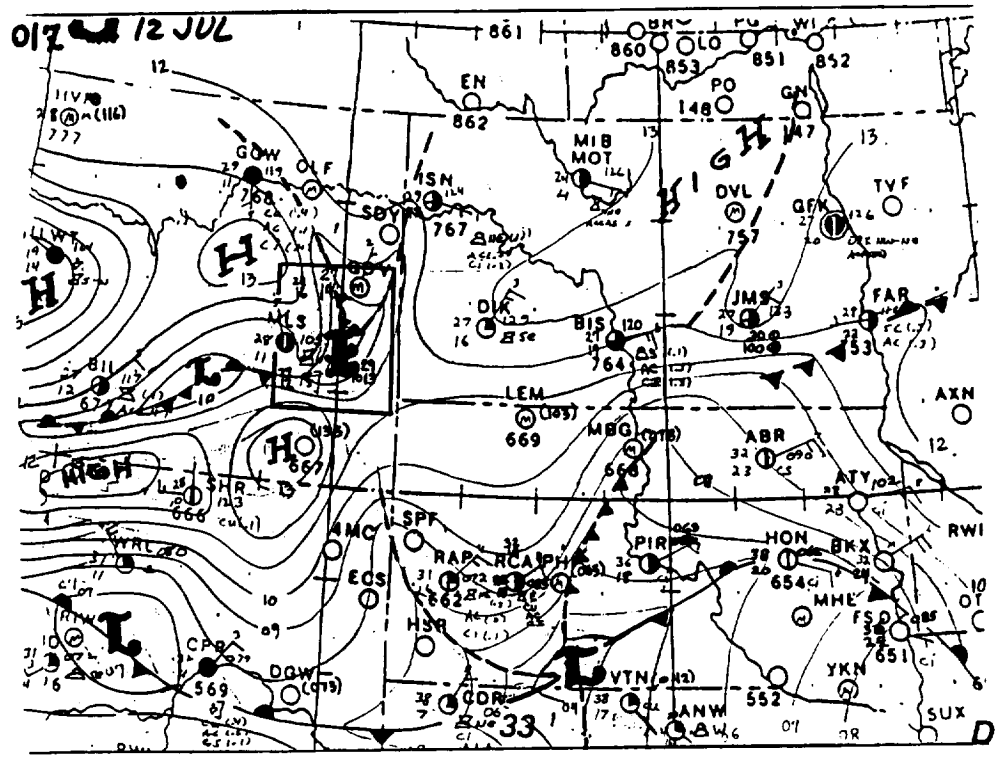
01Z 12 JUL
D

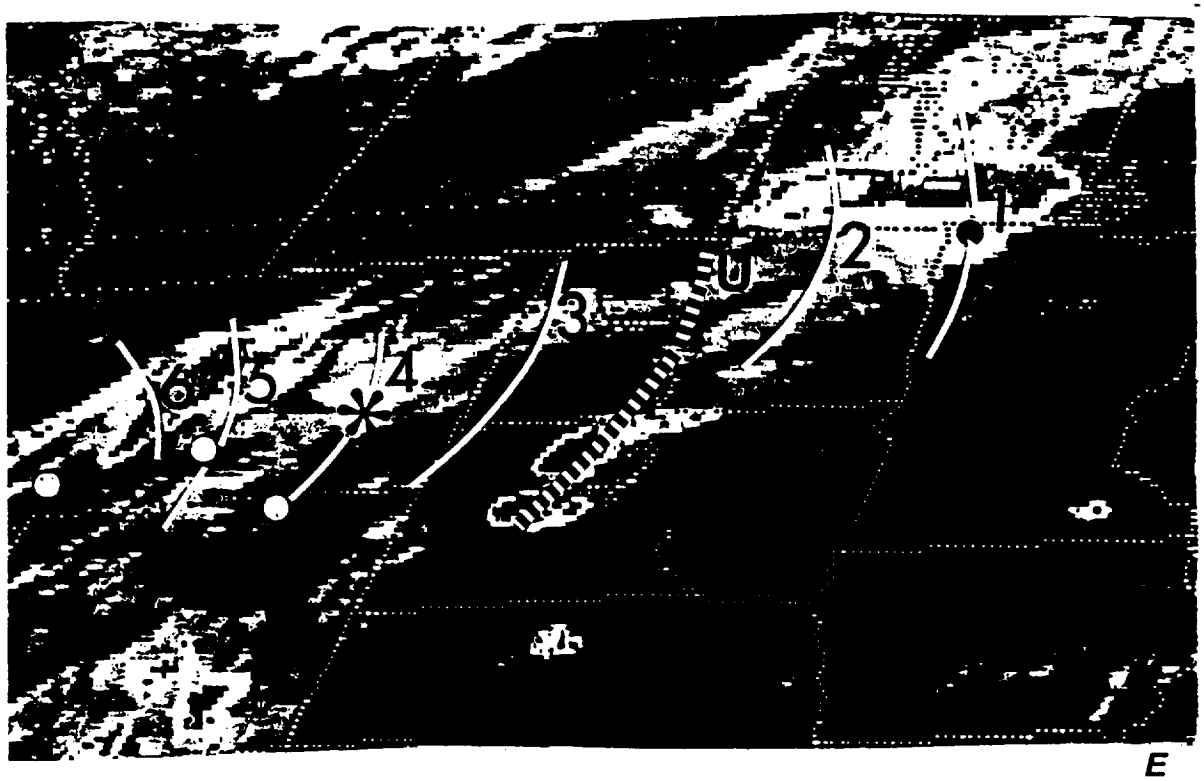

E

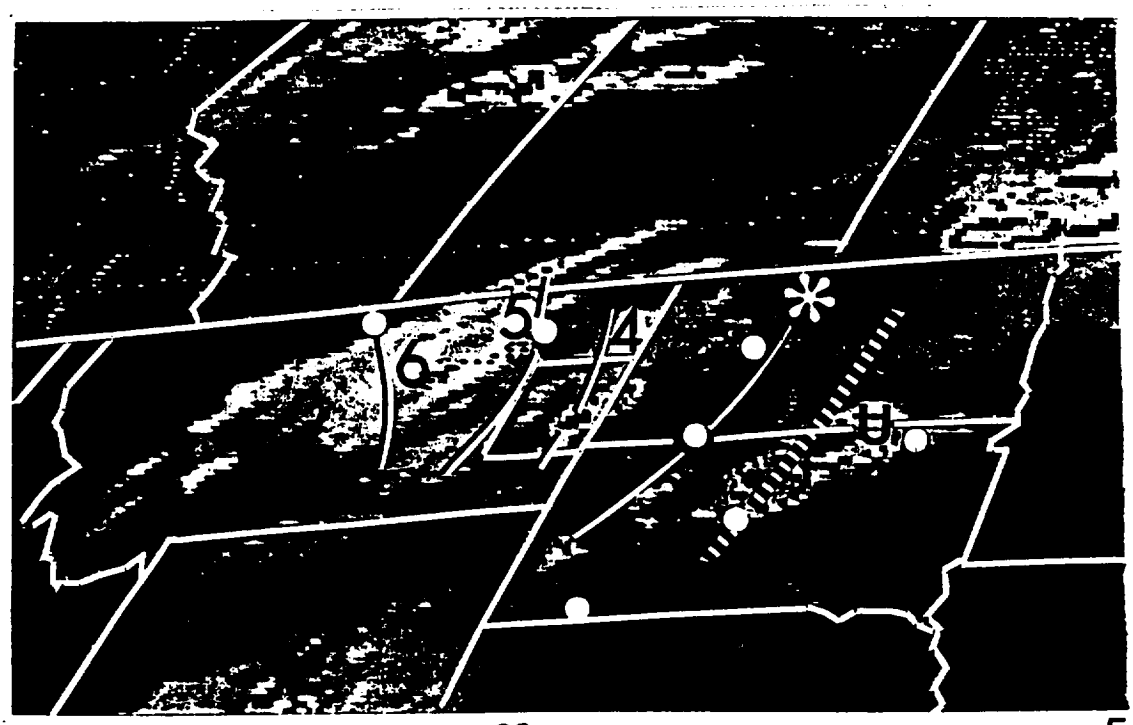

F

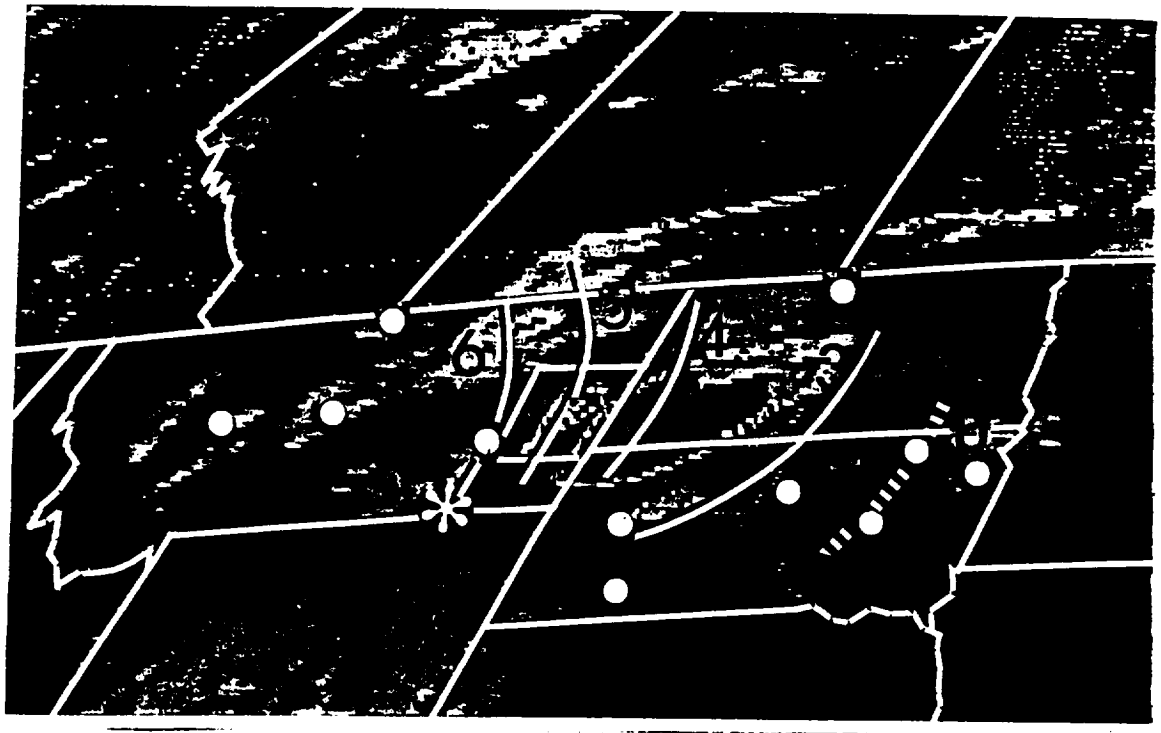

G

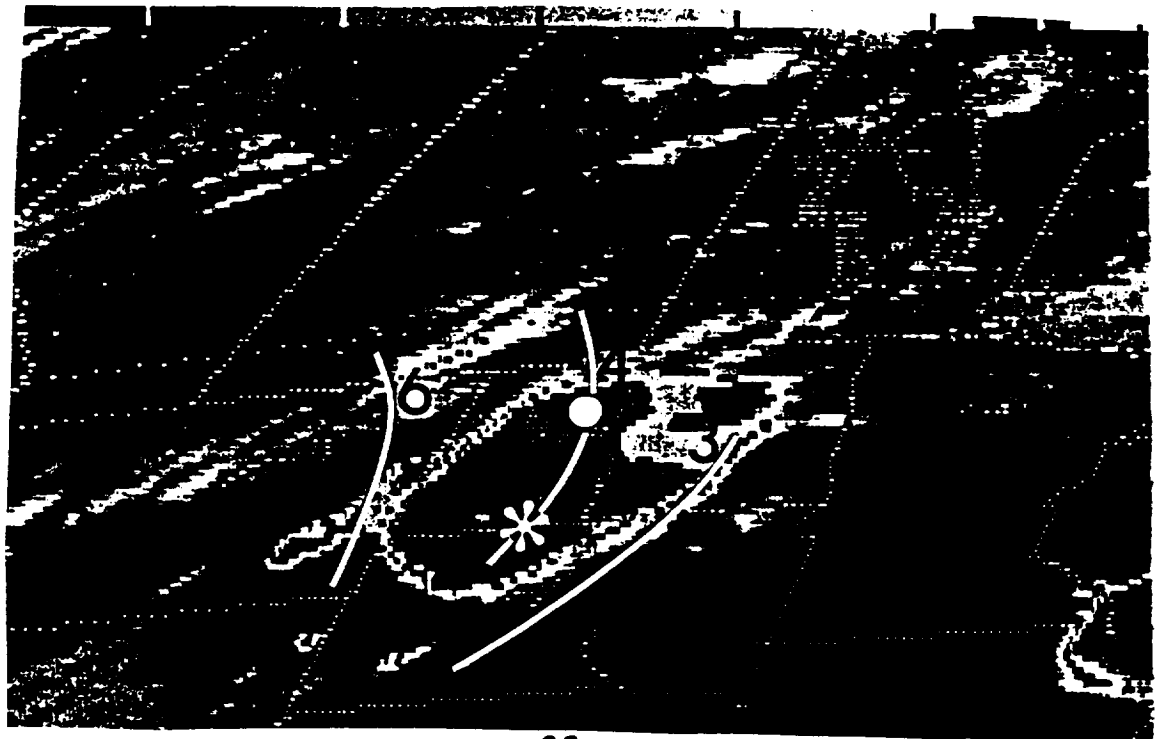

H

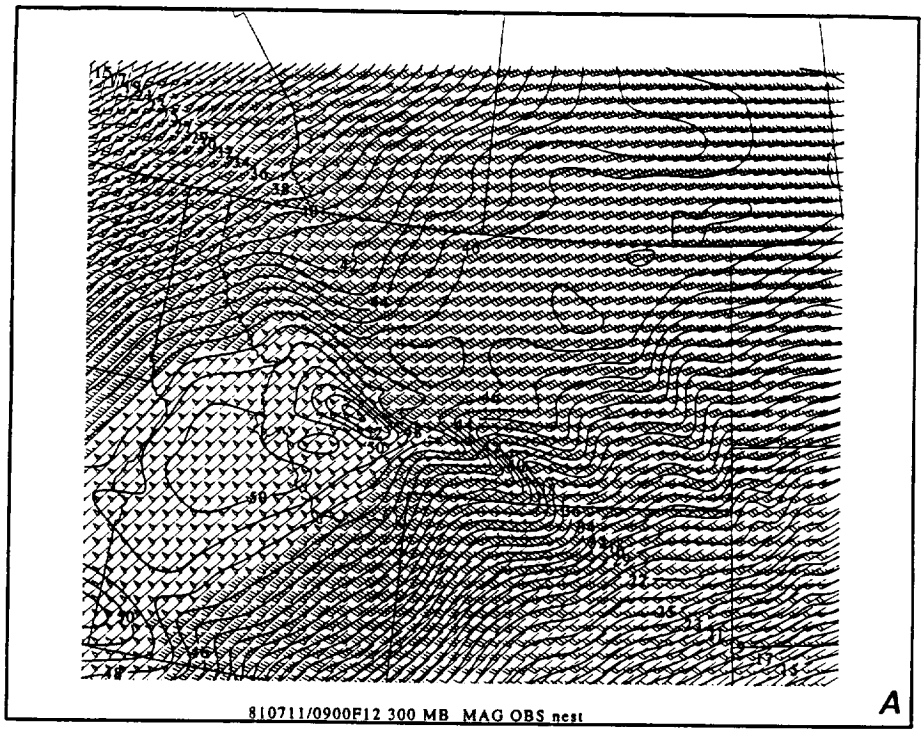
810711/0900F12 300 MB MAG OBS nest
A

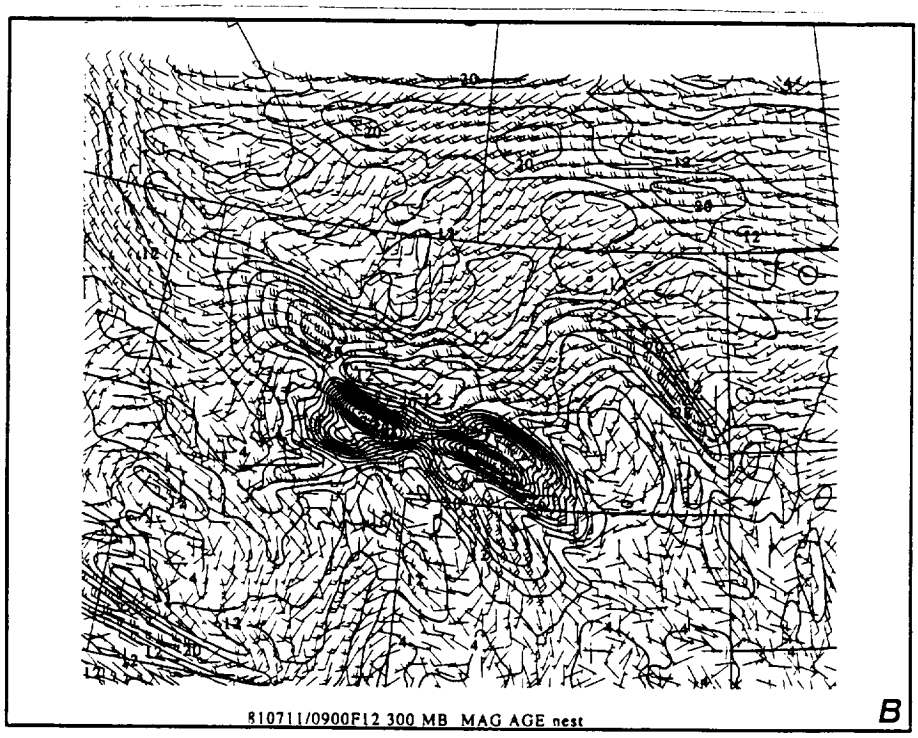
810711/0900F12 300 MB MAG AGE nest
B

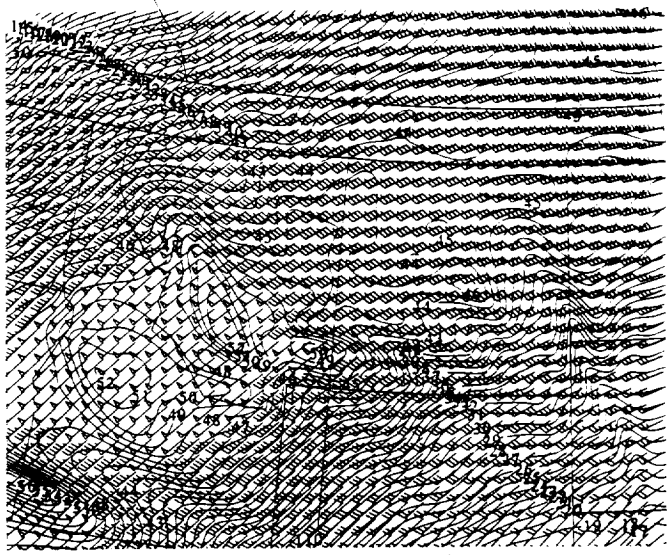

810711/0900F15 300 MB OBS VECTOR WIND nest
810711/0900F15 300 MB MAG OBS nest

c

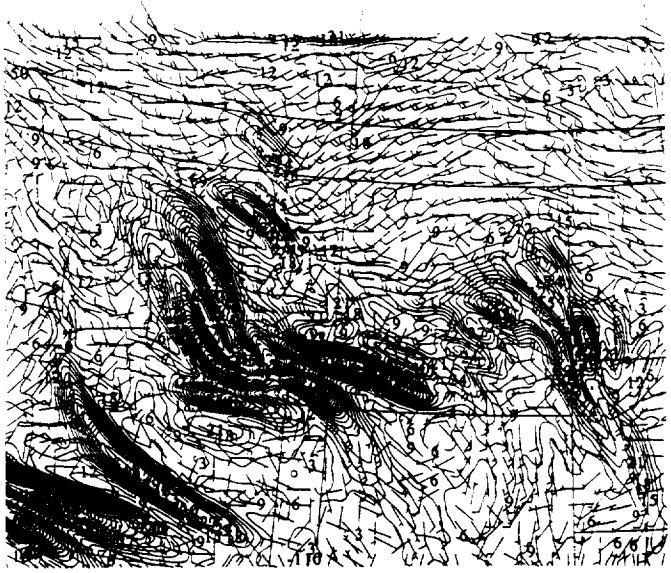

810711/0900F15 300 MB AGEO VECTOR WINDS nest
810711/0900F15 300 MB MAG AGEO WINDS nest

d

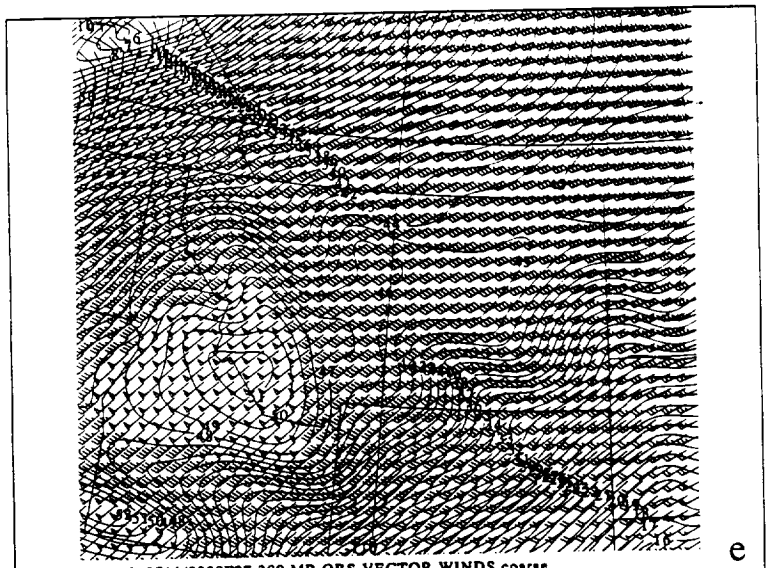

810711/0000F27 300 MB OBS VECTOR WINDS coarse
810711/0000F27 300 MB MAG OBS WINDS coarse

e

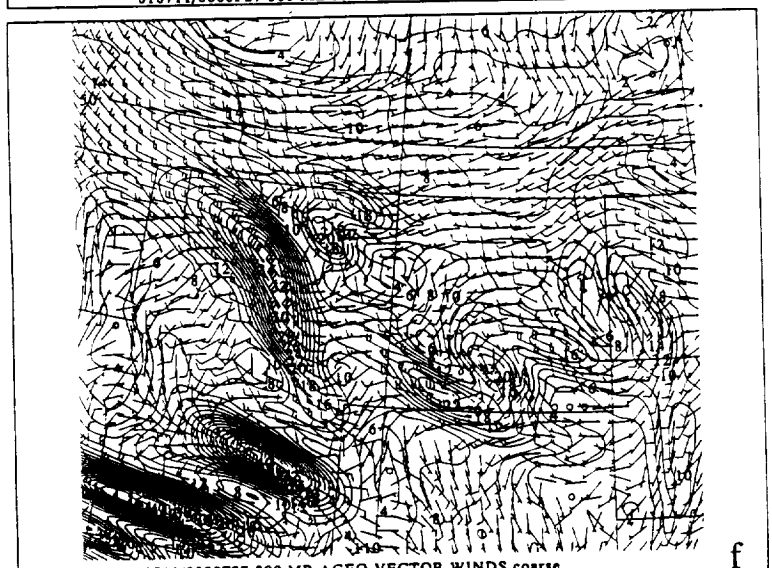

810711/0000F27 300 MB AGEO VECTOR WINDS coarse
810711/0000F27 300 MB MAG AGEO WINDS coarse

f

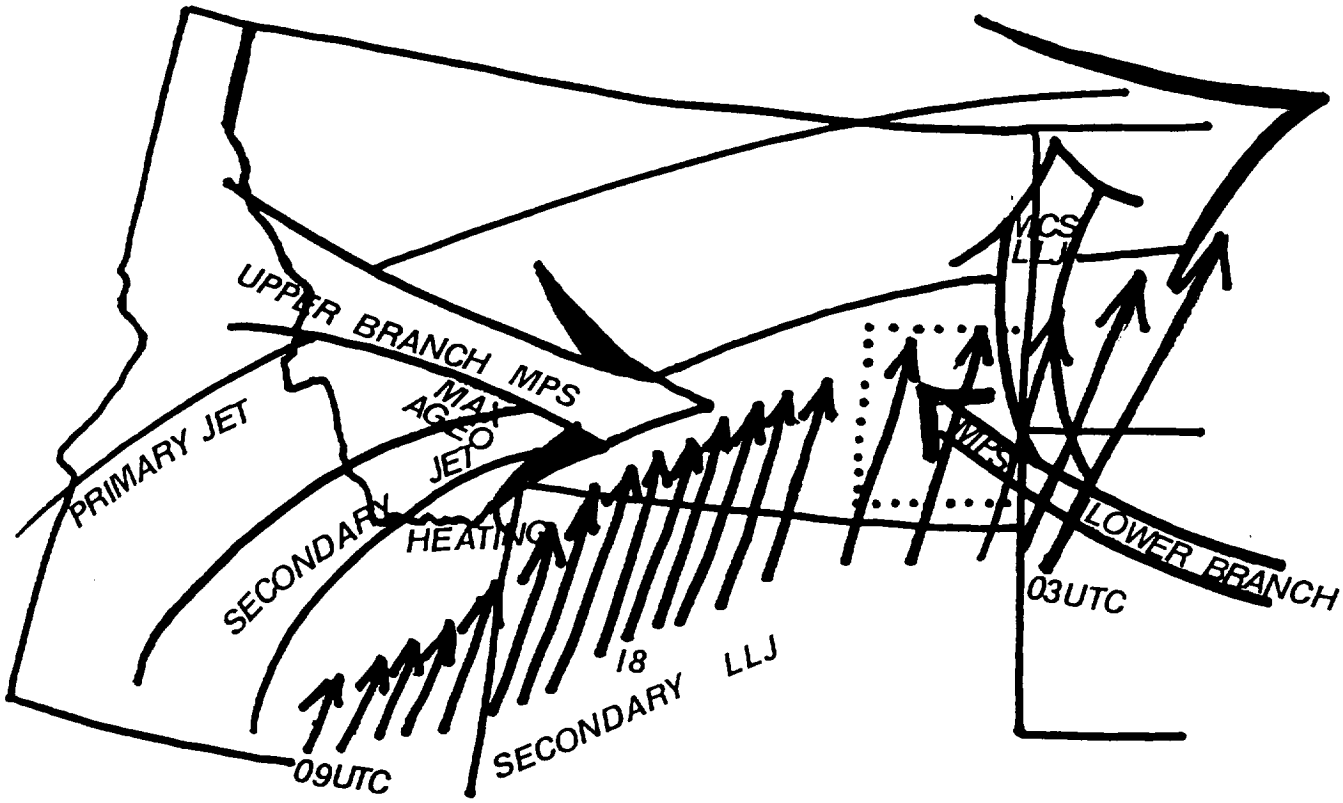
UPPER BRANCH MPS
PRIMARY JET
MAX
AGEO
JET
SECONDARY
HEATING
MCS
LLJ
MPS
LOWER BRANCH
03UTC
18
SECONDARY LLJ
09UTC